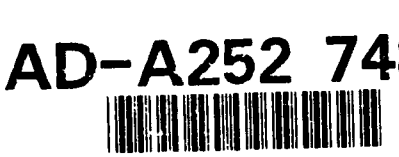

(2)

NAVAL POSTGRADUATE SCHOOL
Monterey, California

THESIS

PREDICTING THE UNDERWATER SOUND OF MODERATE AND HEAVY RAINFALL FROM LABORATORY MEASUREMENTS OF RADIATION FROM SINGLE LARGE RAINDROPS

by

Leo H. Ostwald, Jr.

March, 1992

Thesis Advisor: Jeffrey A. Nystuen

Unclassified

SECURITY CLASSIFICATION OF THIS PAGE

REPORT DOCUMENTATION PAGE

Form Approved OMB No 0704-0188

1a REPORT SECURITY CLASSIFICATION UNCLASSIFIED	1b RESTRICTIVE MARKINGS
2a SECURITY CLASSIFICATION AUTHORITY	3 DISTRIBUTION / AVAILABILITY OF REPORT Approved for public release; distribution is unlimited.
2b DECLASSIFICATION / DOWNGRADING SCHEDULE	
4 PERFORMING ORGANIZATION REPORT NUMBER(S)	5 MONITORING ORGANIZATION REPORT NUMBER(S)
6a NAME OF PERFORMING ORGANIZATION Naval Postgraduate School	6b OFFICE SYMBOL (If applicable) 55
7a NAME OF MONITORING ORGANIZATION Naval Postgraduate School	
6c ADDRESS (City, State, and ZIP Code)	7b ADDRESS (City, State and ZIP Code) Monterey, CA 93943-5000
8a NAME OF FUNDING / SPONSORING ORGANIZATION	8b OFFICE SYMBOL (If applicable)
9 PROCUREMENT INSTRUMENT IDENTIFICATION NUMBER	
8c ADDRESS (City, State, and ZIP Code)	10 SOURCE OF FUNDING NUMBERS

PROGRAM ELEMENT NO	PROJECT NO	TASK NO	WORK UNIT ACCESSION NO

11 TITLE (Include Security Classification)
Predicting the Underwater Sound of Moderate and Heavy Rainfall from Laboratory Measurements of Radiation from Single Large Raindrops

12 PERSONAL AUTHOR(S) Ostwald, Leo H. Jr.

13a TYPE OF REPORT	13b TIME COVERED	14 DATE OF REPORT (Year, Month Day)	15 PAGE COUNT
Master's Thesis	FROM _____ TO _____	March, 1992	168

16 SUPPLEMENTARY NOTATION
The views expressed in this thesis are those of the author and do not reflect the official policy or position of the Department of Defense or the U.S. Government.

17 COSATI CODES			18 SUBJECT TERMS (Continue on reverse if necessary and identify by block number)
FIELD	GROUP	SUB-GROUP	Rainfall Rate, Underwater Sound Spectrum, Ambient Noise, Inverse Technique, Precipitation

19 ABSTRACT (Continue on reverse if necessary and identify by block number)

Large raindrops (greater than 2.2 mm diameter) that strike a water surface at terminal velocity are capable of creating bubbles that radiate significant underwater acoustical energy. Previous studies have revealed a positive correlation between underwater sound spectral levels during rainfall and the number of large raindrops present. Therefore, laboratory measurements have been made of the underwater sound generated by large rain-drops. Using the laboratory measurements, smoothed energy density spectra for various sizes of large raindrops are determined. These spectra are then used to compute a predicted underwater sound spectrum due to rainfall for rainfall rates of 15 mm/hr and 100 mm/hr, assuming an exponential (Marshall-Palmer) raindrop size distribution. The resulting spectra are compared to underwater sound spectra measured at sea during periods with similar rainfall rates. The predicted rainfall spectra are comparable to the measured rainfall spectra. Possible reasons for differences are discussed. An inversion technique for obtaining the raindrop size distribution from the rainfall acoustical spectrum is presented. An alternate approach for obtaining the required inversion matrix is suggested for future work.

20 DISTRIBUTION / AVAILABILITY OF ABSTRACT	21 ABSTRACT SECURITY CLASSIFICATION
☒ UNCLASSIFIED/UNLIMITED ☐ SAME AS RPT ☐ DTIC USERS	UNCLASSIFIED

22a NAME OF RESPONSIBLE INDIVIDUAL	22b TELEPHONE (Include Area Code)	22c OFFICE SYMBOL
Jeffrey A. Nystuen	(408) 646-2917	OC/Ny

DD Form 1473, JUN 86 *Previous editions are obsolete* SECURITY CLASSIFICATION OF THIS PAGE

S/N 0102-LF-014-6603

Unclassified

Approved for public release; distribution is unlimited.

Predicting the Underwater Sound of Moderate and Heavy Rainfall from
Laboratory Measurements of Radiation from Single Large Raindrops

by

Leo H. Ostwald Jr.
Lieutenant, United States Navy
B.S., Montana State University, 1985

Submitted in partial fulfillment of
the requirements for the dual degrees of

MASTER OF SCIENCE IN PHYSICAL OCEANOGRAPHY
MASTER OF SCIENCE IN ENGINEERING ACOUSTICS

from the

NAVAL POSTGRADUATE SCHOOL
March 1992

Author: Leo H. Ostwald Jr.
Leo H. Ostwald Jr.

Approved by:
J. A. Nystuen, Thesis Advisor

H. Medwin, Co-Advisor

Curtis A. Collins, Chairman,
Department of Oceanography

Anthony A. Atchley, Chairman,
Engineering Acoustics Academic Committee

ABSTRACT

Large raindrops (greater than 2.2 mm diameter) that strike a water surface at terminal velocity are capable of creating bubbles that radiate significant underwater acoustical energy. Previous studies have revealed a positive correlation between underwater sound spectral levels during rainfall and the number of large raindrops present. Therefore, laboratory measurements have been made of the underwater sound generated by large raindrops. Using the laboratory measurements, smoothed energy density spectra for various sizes of large raindrops are determined. These spectra are then used to compute a predicted underwater sound spectrum due to rainfall for rainfall rates of 15 mm/hr and 100 mm/hr, assuming an exponential (Marshall-Palmer) raindrop size distribution. The resulting spectra are compared to underwater sound spectra measured at sea during periods with similar rainfall rates. The predicted rainfall spectra are comparable to the measured rainfall spectra. Possible reasons for differences are discussed. An inversion technique for obtaining the raindrop size distribution from the rainfall acoustical spectrum is presented. An alternate approach for obtaining the required inversion matrix is suggested for future work.

TABLE OF CONTENTS

LIST OF TABLES

LIST OF FIGURES

ACKNOWLEDGEMENTS

I would like to express my gratitude to my wife, Jennifer, who provided encouragement and support throughout this effort.

A number of individuals have helped make this work possible, especially my advisor Dr. Jeffrey Nystuen and co-advisor Dr. Herman Medwin. Their suggestions and advice during all phases of the research were invaluable. I would like to thank LT Peter Jacobus, who shared with me his knowledge of the laboratory procedures and signal analysis techniques. Also, collection of the raindrop data would have been much more difficult without the assistance of LT Chris Scofield and LT Glenn Miller.

Special thanks goes to Mr. David Powell and Mr. John O'Sullivan of the Monterey Bay Aquarium for providing filtered seawater for the laboratory tank. I am indebted to Dr. Ching-Sang Chiu of the Oceanography Department who provided much needed insights into inversion theory, and to Dr. James Miller of the Electrical Engineering Department for helping resolve some spectral analysis issues.

I am also grateful to Mr. James Stockel and Mr. Tarry Rago for taking the time to analyze the salinity samples, and to Mr. Mike Cook for making available the rainfall spectrum data. Partial financial support was provided by the Tactical Oceanographic Warfare Support Program Office, Naval Research Laboratory Detachment, Stennis Space Center, Mississippi.

I. INTRODUCTION

Precipitation is an important factor in air/ocean climate modeling and weather forecasting. However, measurement of precipitation in the open ocean is a difficult venture. Because of platform motion and disturbance of the airflow pattern in the vicinity of the platform, rain gauge measurements at sea are unreliable. Moreover, rain gauges measure rainfall only at the host platform, and so spatial variability in the precipitation cannot be determined. Indirect methods for rainfall measurement include radar backscatter/attenuation measurements and analysis of satellite imagery, These methods tend to be rather inaccurate. An independent means of verifying the rainfall measurements obtained by remote sensing is therefore desirable.

The underwater sound produced by rainfall striking the ocean surface may provide another means of measuring rainfall rates and raindrop size distributions at sea. The shape of the underwater sound spectra in the presence of rain is much different from the spectral shape when rainfall is absent (Lemon and Farmer, 1984). Also, the spectral levels when rain is present can be many decibels higher than the spectral levels due to wind generated noise, as shown in Figure 1. Thus, the underwater noise generated by rainfall is identifiable, which suggests that a correlation may exist between the precipitation rate and underwater spectral levels.

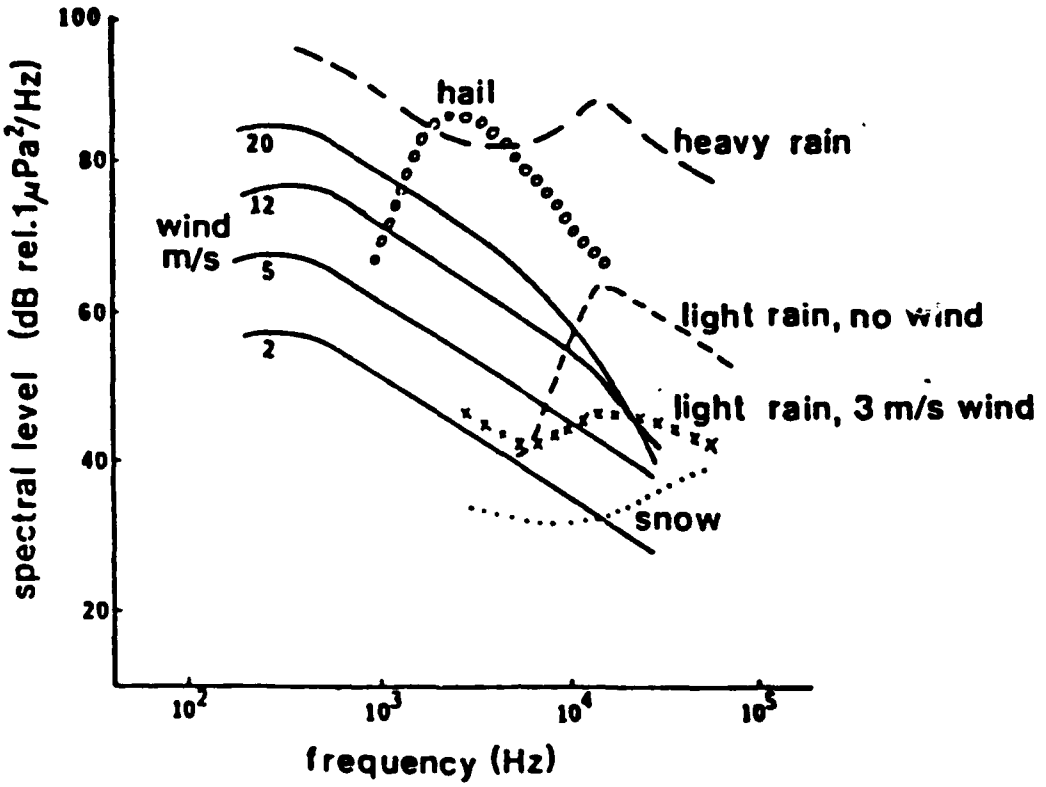

Figure 1. Spectral characteristics of ocean noise (Nystuen and Farmer, 1989).

However, attempts to develop direct empirical relationships between rainfall rate and underwater sound intensities have only been moderately successful. First, significant surface wind effects on the rainfall underwater acoustical signature have been observed during conditions of light rainfall (Nystuen and Farmer, 1987). The surface wind effect will be described later. Second, the character of the underwater sound generated by rainfall appears to be influenced not only by the amount of rainfall, but by the sizes of the raindrops that strike the surface. This possibility was suggested by

McGlothin as one explanation for the inadequate empirical fit between rainfall rate and underwater spectral levels which he obtained for conditions of moderate to heavy rainfall.

The purpose of this thesis is to predict the underwater sound spectrum observed at sea during conditions of moderate to heavy rainfall using laboratory measurements of the underwater sound generated by large raindrops. Chapter II will explain the motivation for this work. In the first part of Chapter II, the mechanisms for underwater sound generation by raindrops will be discussed. Characteristics of raindrop size distributions will then be described, along with implications of drop size distribution variations on rainfall rate predictions using underwater sound measurements. The remainder of Chapter II will describe field observations of underwater rain noise and relate these observations to the raindrop sound generation mechanisms.

In Chapter III, results of laboratory measurements of the impact noise of raindrops will be presented. The primary purpose of these measurements was to determine how to treat the laboratory raindrop impact sound in terms of its farfield contribution to the underwater rainfall acoustical noise. In Chapter IV, the acoustical energy density spectrum associated with various sizes of large raindrops will be obtained from laboratory measurements of large raindrop impact and bubble sound. In Chapter V, the relationship between the laboratory measured spectra and the

rainfall spectra observed at sea will be established, and then used to predict the underwater sound spectrum due to rainfall. An inversion technique for determining raindrop size distributions from the measured rainfall sound spectrum is also described in Chapter V. The inversion technique is presented mainly to establish a formalism for future work. As will be seen, because of the lack of adequate information about the sea surface conditions, the rainfall drop size distributions, and the bubble densities during rainfall, an inversion was not attempted in this work.

II. BACKGROUND

A. SOURCES OF UNDERWATER SOUND DUE TO RAINDROPS

In order to determine the relationship between underwater acoustic levels and rainfall rate, the characteristics of the underwater sound produced by individual raindrops must first be understood. The two components of the underwater sound produced by drop splashes were first described by Franz (1959). The first source of raindrop sound is the impact itself; the second source is an oscillating bubble which sometimes forms. The underwater acoustical signal generated by a large (4.2 mm diameter) and particularly energetic drop is shown in Figure 2. The oscillating bubble is a highly efficient radiator of acoustical energy, generating a damped sinusoidal signal much longer in duration than the impact signal. For the case in Figure 2, the bubble formation is delayed by about 50 msec from the time of impact.

Two distinct mechanisms have been identified for the formation of bubbles by naturally occurring raindrops (Snyder, 1990). These are known as the Type I mechanism (or regular entrainment) for small raindrops (0.8 to 1.1 mm diameter) and the Type II mechanism for large raindrops (greater than 2.2 mm diameter). The regions of bubble formation (in terms of drop size and impact velocity) for each of these two

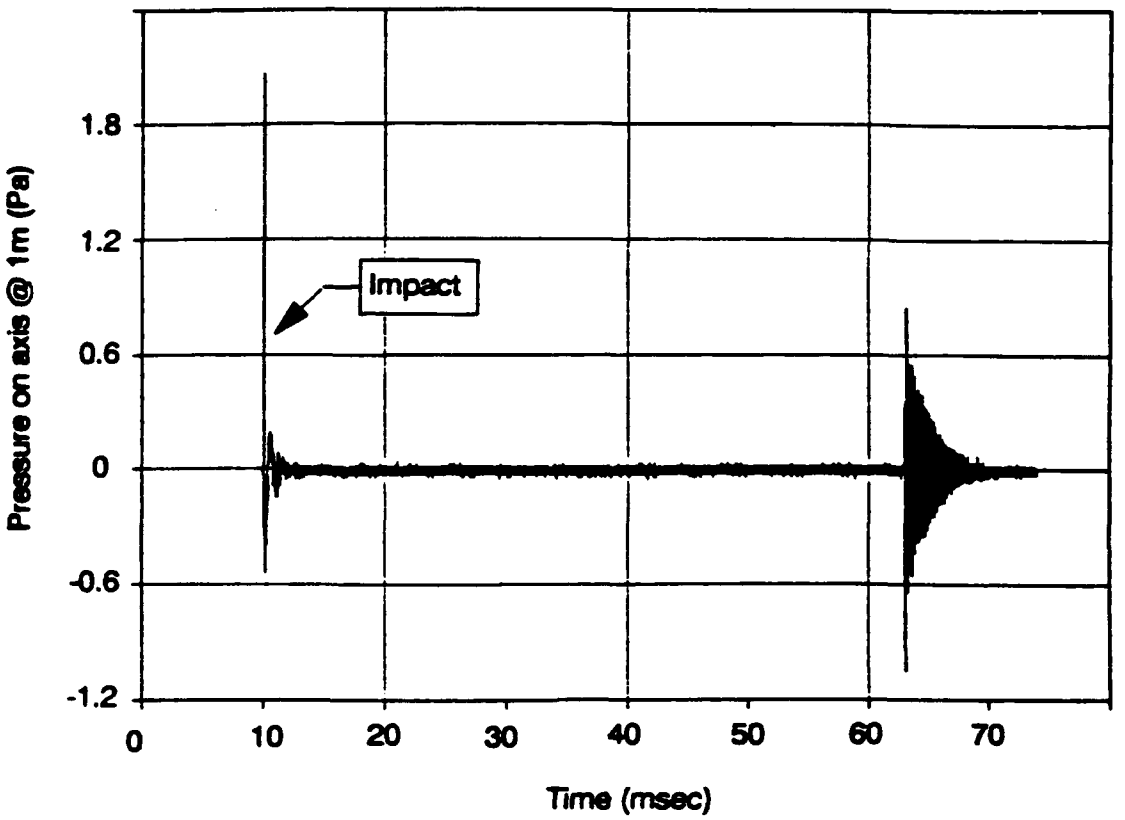

Figure 2. Impact and bubble signal of a 4.2 mm diameter raindrop in artificial seawater. The time delay between impact and onset of the bubble is about 50 msec.

mechanisms are shown in Figure 3. Note that for natural rainfall the drops strike the surface at terminal velocity, so only regions on the terminal velocity curve are applicable.

The Type I mechanism occurs for drops 0.8 to 1.1 mm in diameter falling at terminal velocity, and has been studied at the Naval Postgraduate School (Kurgan, 1989; Medwin *et al.*, 1990) and elsewhere (Pumphrey *et al.*, 1989; Oguz and Prosperetti, 1990). The Type I bubble results when the base of a conical splash crater is

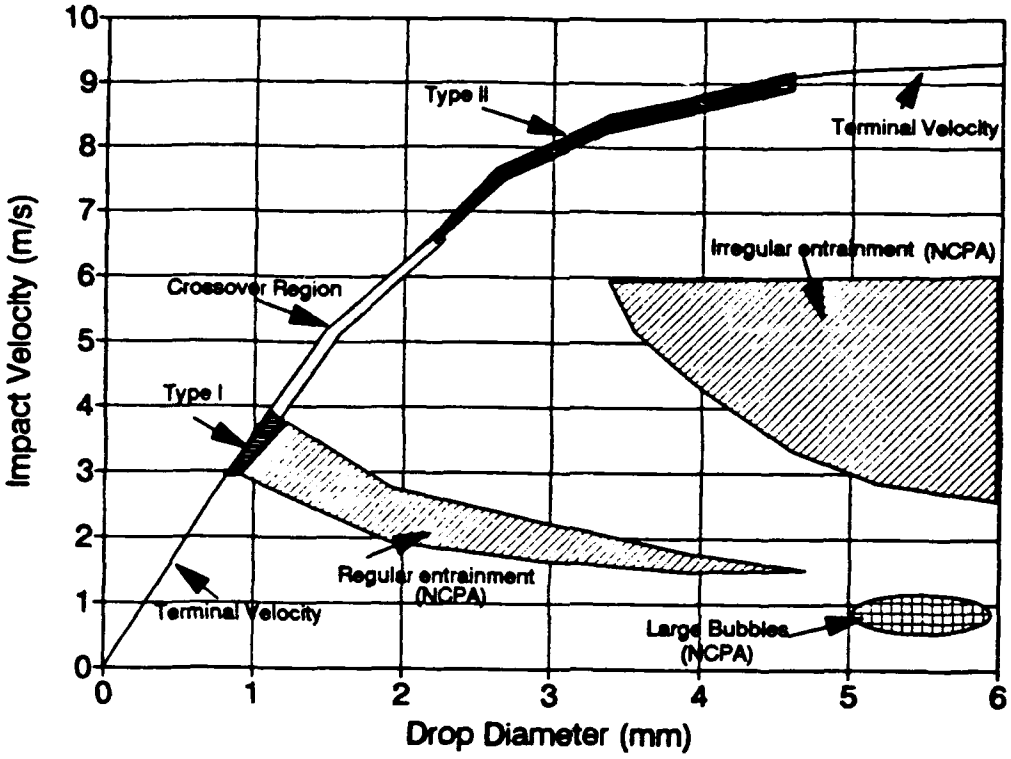

Figure 3. Bubble formation regions as a function of drop diameter (horizontal axis) and drop velocity (vertical axis) (Jacobus, 1991). NCPA is the National Center for Physical Acoustics.

pinched off (Longuet-Higgins, 1990); the resulting bubble has a resonance frequency of about 15 kHz. The Type I raindrops have been observed to produce bubbles 100% of the time when striking a smooth water surface at normal incidence, but the percentage of bubble formation decreases to 0% as the incidence angle increases to 25° (Kurgan, 1989).

The Type II mechanism occurs for drops larger than 2.2 mm in diameter. So far this mechanism has been studied only at the Naval Postgraduate School (Snyder,

1990; Jacobus, 1991) because of the availability of a 26 meter high drop tower (the larger Type II drops must be released from sufficient height to achieve terminal velocity). The sequence of events leading to Type II bubble formation are shown in Figure 4 (Snyder, 1989). First, a closed canopy of water forms above the splash cavity. Water continues to flow up the sides of the canopy. This convergence of water generates upward and downward moving turbulent jets. The downward jet plunges through the bottom of the splash crater, entraining air that pinches off to form a resonating bubble.

Unlike the Type I raindrops at normal incidence, not all drops larger than 2.2 mm diameter produce bubbles when striking the surface at normal incidence and at terminal velocity. Also, the dependence of Type II bubble formation on incidence angle is unknown. However, Snyder (1990) observed that, in order for a bubble to form, the downward moving jet must be canted (as illustrated in Figure 4). Drops for which there was no cant in the downward moving jet were not observed to produce bubbles. This suggests that increasing the incidence angle may actually increase the probability of bubble formation, since oblique incidence may contribute to asymmetry in the resulting splash.

The frequency spectrum of underwater sound generated by Type II raindrop bubbles was studied by Jacobus (1991). The spectral density curve of an individual

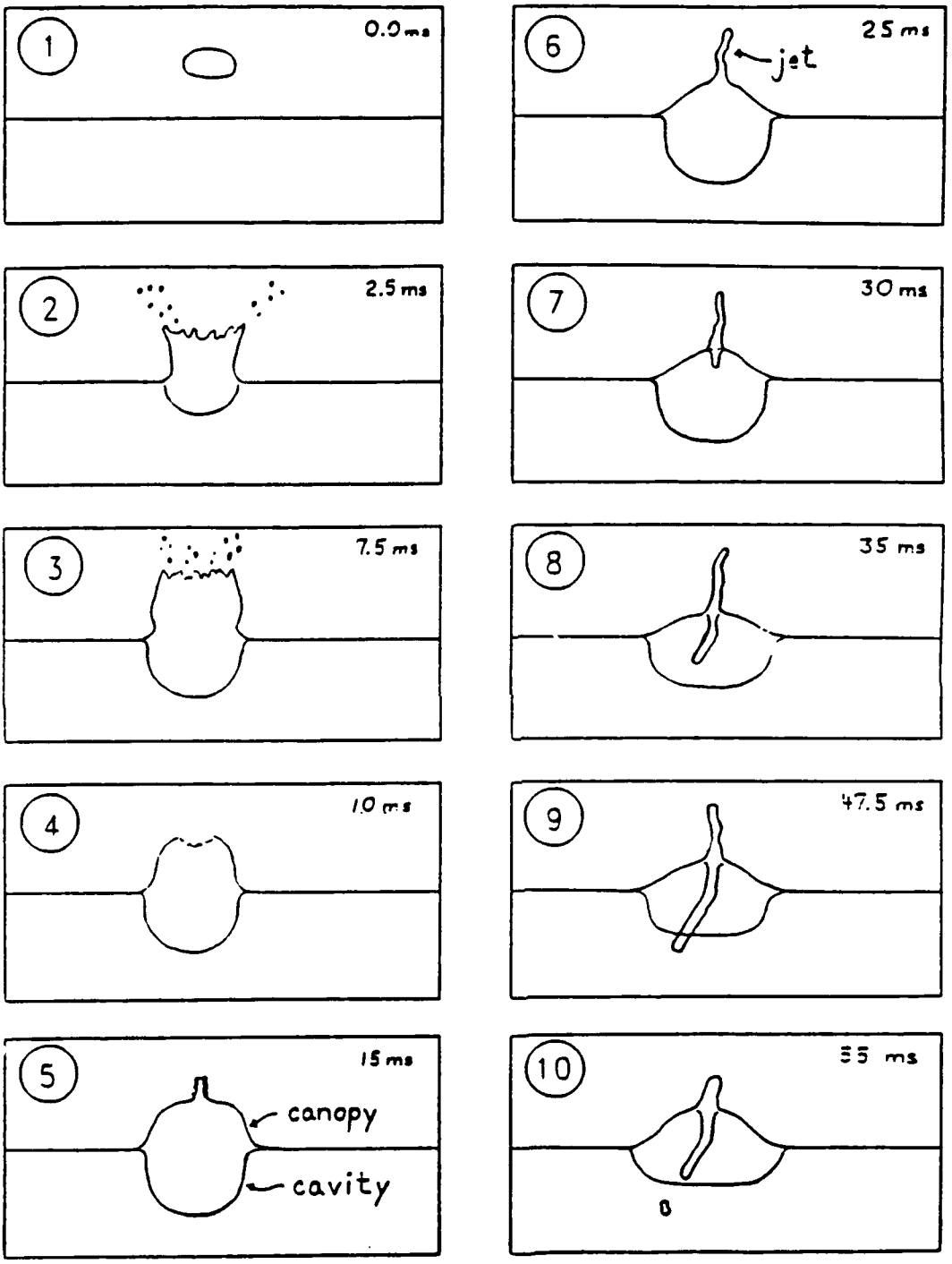

Figure 4. Drop sequence sketch (Snyder, 1990).

Type II raindrop bubble signal is shown in Figure 5. The figure shows the contribution to the spectrum from the dominant bubble and from a secondary bubble which sometimes forms (more than one secondary bubble may be present). According to both Jacobus and Snyder, Type II dominant bubbles typically resonate at frequencies between 2 and 10 kHz. The frequency of a freely oscillating bubble in water is inversely proportional to the bubble radius (Clay and Medwin, 1977). The dominant Type II bubble frequency tends to decrease with increasing drop size (Figure 6),

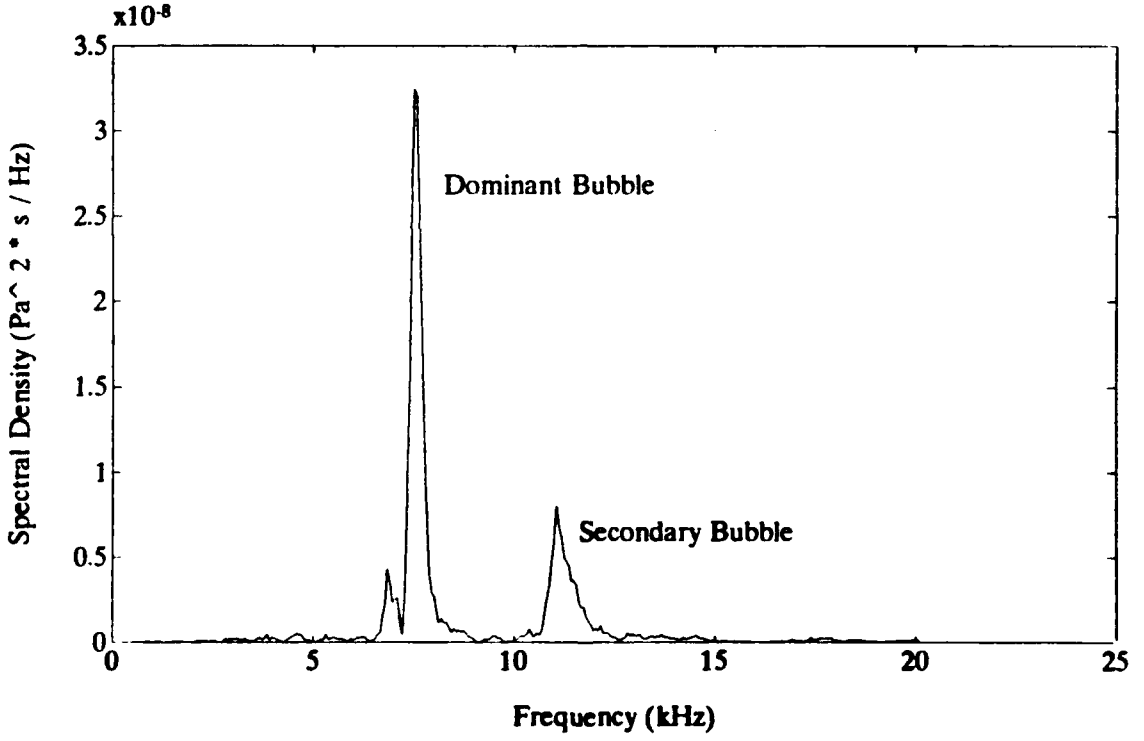

Figure 5. Spectrum of the 1 m on-axis bubble signals for a 3.4 mm raindrop in artificial seawater combined with filtered seawater. The peaks in the spectrum are due to primary and secondary bubbles.

suggesting that larger raindrops tend to produce larger bubbles as expected. Jacobus also studied the variation of Type II raindrop bubble energy with drop temperature, surface temperature and salinity. He determined that Type II bubbles radiate more energy as the temperature difference between the drop and the surface increases. In fact, the average bubble energy for a 10° C temperature difference is almost twice that for a 0° C temperature difference. Also, the bubbles radiate much more energy in fresh water than in saline water (he reports a 45% lower bubble energy in water of 35 ppt salinity as compared to fresh water). Both of these effects have significant implications for the prediction of rainfall rates at sea from acoustical measurements. The cause of the bubble energy variations with salinity and surface-drop temperature difference has not yet been determined.

B. CHARACTERISTICS OF RAINFALL DROP SIZE DISTRIBUTIONS

Because the character of the underwater noise generated by individual raindrops is a function of the drop size, it may also be true that the character of underwater rainfall sound is dependent on the number of drops of a given drop size that strike the surface. If underwater acoustical signals are to be used for rainfall measurements, the raindrop size distribution must be known or inferred, as well as the relationship between the raindrop size distribution and rainfall rate. A summary of raindrop sizes and the corresponding mechanisms that generate underwater noise is presented in

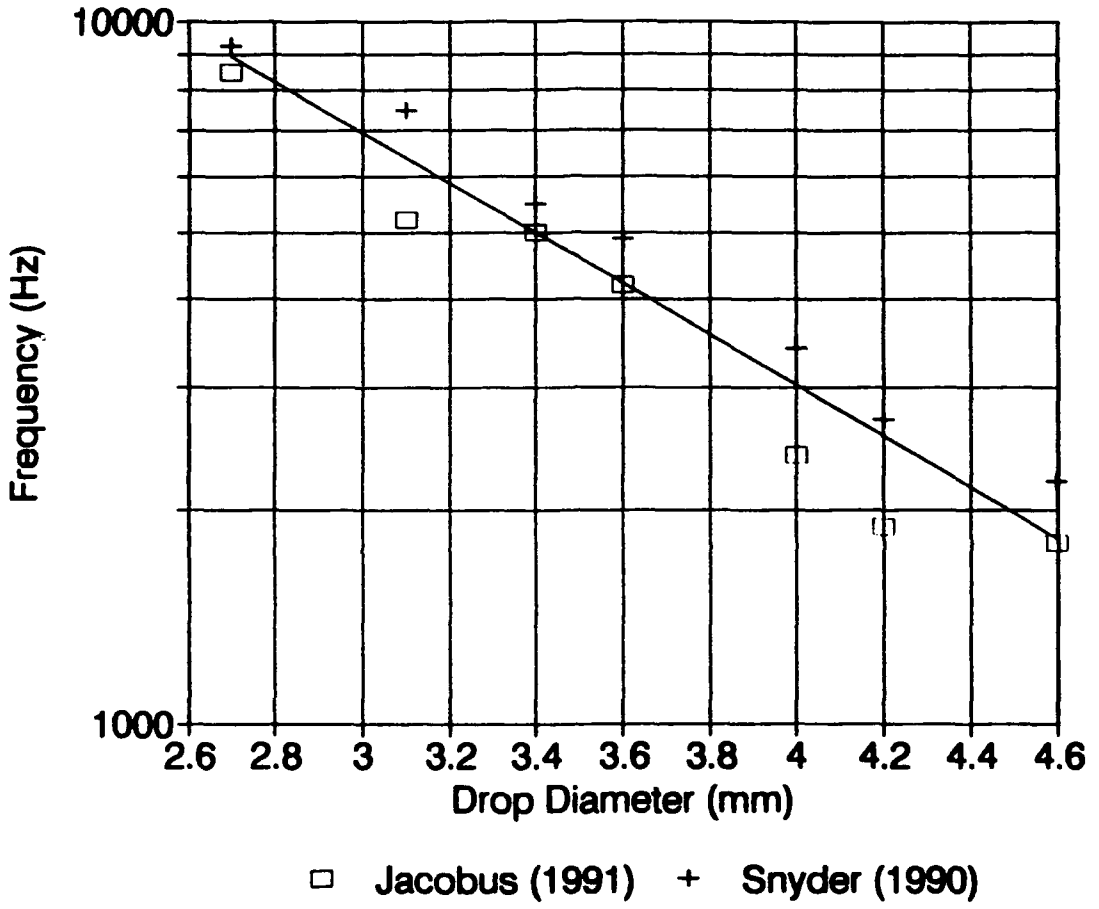

Figure 6. Type II dominant bubble frequency vs. drop diameter.

Table 1. The nomenclature shown in Table 1 for the various drop size ranges was suggested by Medwin *et al.* (1992).

TABLE 1. RAINDROP SIZES VS. SOURCES OF ACOUSTIC NOISE

Nomenclature	Equivalent Raindrop Diameter (mm)	Source of Underwater Acoustic Noise
Minuscule	0 - 0.8	Impact Only
Small (Type I)	0.8 - 1.1	Bubble and Impact
Mid-Size	1.1 - 2.2	Impact Only
Large (Type II)	2.2 and larger	Bubble and Impact

The classic raindrop size distribution model is the Marshall and Palmer model (1948) given by:

$$N(D) = N_o \cdot e^{-\Lambda D} \qquad (1)$$

where N is the number of drops per unit volume (m^3) per unit drop diameter increment (0.1 mm), D is the equivalent spherical drop diameter (mm), and N_o (drops per m^3 per 0.1 mm) and Λ (mm^{-1}) are statistical parameters that determine the character of the drop size distribution. The term "equivalent spherical diameter" is used here since, except for minuscule drops, raindrops are not in fact spherical; they are ellipsoidal, with the larger ones flattened at the base. Marshall and Palmer determined that the parameter Λ (the exponential slope) is given by $\Lambda = 4.1 \cdot R^{-0.20}$,

where R is the rainfall rate in mm/hr. Marshall and Palmer also suggested that N_o (the $D = 0$ intercept) is a constant equal to 800 drops per m^3 per 0.1 mm. Thus, the Marshall-Palmer distribution predicts that the number of very small drops present in rainfall is independent of the rainfall rate (N approaches N_o as the drop size, D, goes to zero), and that fewer large drops are present for low rainfall rates than for high rainfall rates. The characteristics of the Marshall-Palmer distribution are illustrated in Figure 7, which shows the Marshall-Palmer distributions for rainfall rates of 15 and 100 mm/hr.

If the Marshall-Palmer drop size distribution were suitable for all rainfall conditions, then the rainfall rate could be determined by measuring the exponential slope of the drop size distribution alone, and then using the Marshall-Palmer Equation for Λ to solve for R. However, actual raindrop size distributions can differ markedly from the Marshall-Palmer distribution. Cataneo and Stout (1968) observed drop size distributions on the Atlantic Coast which varied with synoptic conditions (cold frontal rains consisted of a larger number of small drops than warm frontal rains for similar rainfall rates). Waldvogel (1974) observed large jumps in the value of N_o associated with mesoscale variations within a given precipitation field. For instance, N_o values for showers and thunderstorms (in areas of weak convection) tended to be large (on the order of 35,000) while N_o values for steady, widespread rain (in areas

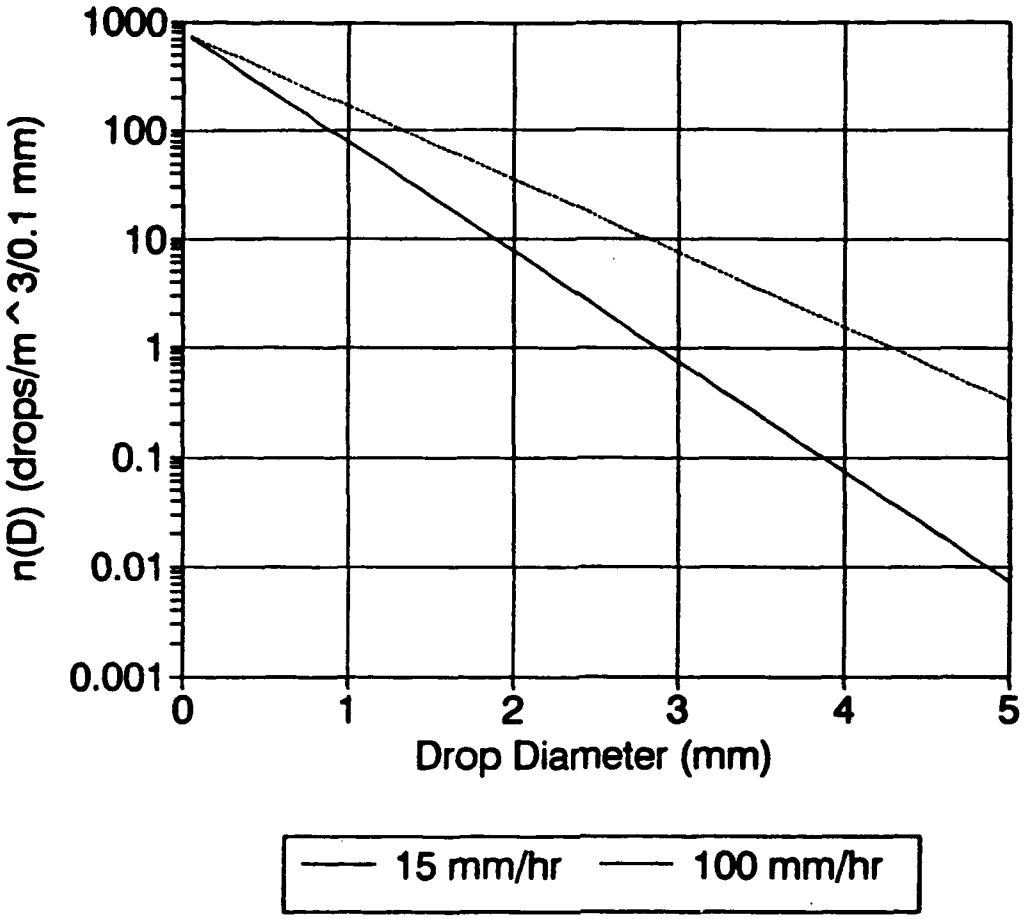

Figure 7. Marshall-Palmer drop size distributions ,$N(D)$, for 15 mm/hr and 100 mm/hr rainfall rates.

with little or no convection) tended to be small (on the order of 4000). The value for Λ, the drop size distribution slope, has also been observed to depart from the expression given by Marshall and Palmer. Hodson (1986) observed that Λ approaches a constant value between 2.1 and 2.3 mm^{-1} for rainfall rates in excess of 25 mm/hr; above 25 mm/hr, an increase in rainfall rate is reflected by an increase in the value of N_o.

While the exponential distribution is accepted by most researchers to be an adequate approximation to actual raindrop size distributions, Ulbrich (1983) contends that drop size distributions can be better modeled as gamma distributions of the form:

$$N(D) = N_o \cdot D^{\mu} \cdot e^{-\Lambda \cdot D} \qquad (2)$$

where the variable μ is a positive or negative value. Figure 8, obtained from Ulbrich (1983), compares the exponential distribution with the gamma distribution for both positive and negative values of μ. When μ is greater than zero, the distribution is concave downward, and the smallest and largest drops are fewer in number than for the exponential distribution (in fact, the number of drops goes to zero as D goes to zero for drops less than 1 mm diameter). When μ is less than zero, the distribution is concave upward, and the number of small and large drops is greater than for the comparable exponential distribution. Ulbrich also calculated the values of μ and N_o for different environmental conditions by empirical analysis of rainfall data gathered from many different sources. He determined that the drop size distribution parameters can be roughly categorized according to the type of precipitation. For instance, thunderstorms tend to have relatively large values of N_o and positive μ, while N_o is smaller and μ more variable for stratiform precipitation.

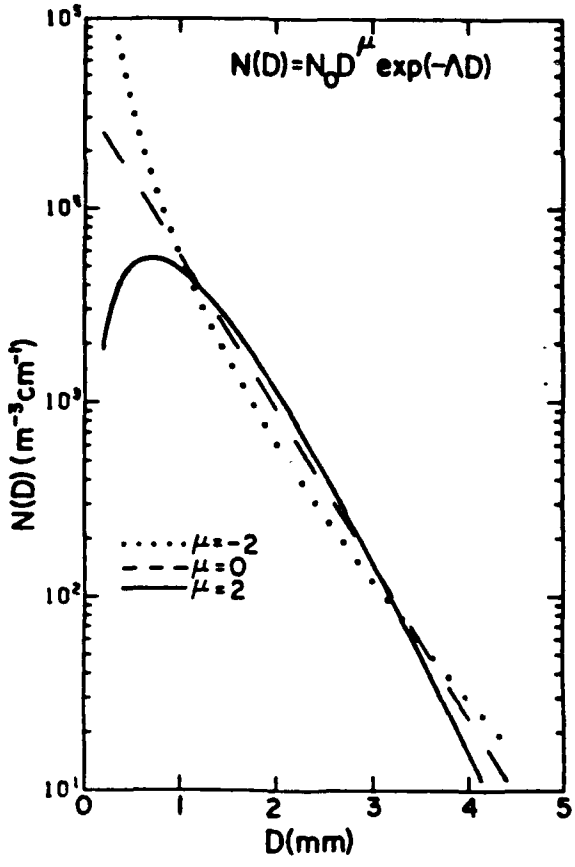

Figure 8. Gamma raindrop size distributions, $N(D)$, for positive and negative values of μ, where D is the drop diameter (Ulbrich, 1983).

While many measurements of raindrop size distributions have been conducted in connection with the study of radar reflectivity from rainfall, very few concurrent measurements of rainfall drop size distributions and rainfall underwater acoustical signatures have been made. Because of this, it will later be necessary to assume a form

for the drop size distribution in order to calculate the predicted underwater acoustic signal from the laboratory measured acoustic signal of individual raindrops. The form of drop size distribution for any required computations will be the exponential Marshall-Palmer distribution. However, it must be kept in mind that the actual drop size distribution may differ significantly from the Marshall-Palmer distribution, which in turn may cause significant differences between the actual and predicted acoustical rainfall signature. Simultaneous field measurements of rainfall rate, rainfall drop size distribution, and rainfall acoustic signals are needed to remedy this limitation.

The raindrop size distribution can be integrated to yield the rainfall rate according to the following equation:

$$R = 3600 \cdot (\frac{\pi}{6}) \cdot 10^{-6} \cdot \int_0^{\infty} N(D) D^3 v_t(D) dD \qquad (3)$$

where R is the rainfall rate in mm/hr, $N(D)$ is the raindrop size distribution (drops per m^3 per 0.1 mm) v_t is the terminal drop velocity (m/s), and D is the drop diameter in mm (Hodson, 1986). The terminal raindrop velocity is a function of raindrop diameter, and varies from approximately 4 m/s for raindrops of 1.0 mm equivalent spherical diameter to 9.1 m/s for raindrops of 5.0 mm equivalent spherical diameter (Pruppacher and Klett, 1978). Snyder (1990) demonstrated that, for raindrops of size 2.2 to 5 mm diameter, the terminal velocity can be approximated by the equation $v_t = 4.6 \cdot D^{1/2}$ (m/s). Thus, for raindrops in excess of 2.2 mm diameter, the rainfall rate

integrand varies approximately as the 7/2 power of D. Since the contribution to the total rainfall rate increases rapidly with increasing drop size, the contribution of large raindrops to the total rainfall rate can be significant, even though the raindrop size distribution tends to decrease exponentially. Since large raindrops also generate a characteristic underwater acoustical signature (via the Type II bubble generating mechanism), they will be emphasized in this work.

C. FIELD OBSERVATIONS OF RAINFALL ACOUSTIC SIGNATURES

1. Observations for Light Rainfall

Much of the research on the ambient underwater noise generated by rainfall has focused on light rainfall conditions because of a consistently observed peak in the underwater sound spectrum at about 15 kHz when light rain is present. An example of the underwater sound spectrum for light rain is shown in Figure 9 (Nystuen and Farmer, 1987). The 15 kHz frequency in the spectrum for light rainfall has been well correlated with the number of small (< 1.5 mm diameter) raindrops present (Nystuen, 1986). The source of the spectral peak at 15 kHz has been mainly attributed to the generation of Type I bubbles by raindrops of 0.8 to 1.1 mm diameter, since the Type I bubbles have a characteristic resonance frequency of about 15 kHz (Pumphrey *et al.*, 1989; Medwin *et al.*, 1990).

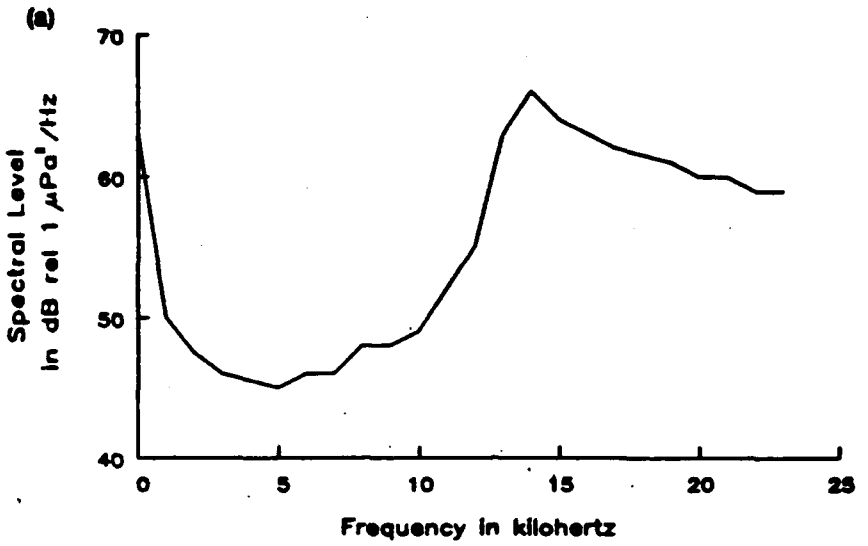

Figure 9. Underwater sound spectrum during light rainfall showing characteristic 15 kHz peak (Nystuen and Farmer, 1987)

The underwater spectral levels in the vicinity of 15 kHz are not useful for predicting the total rainfall rate, since the magnitude and shape of the ambient rainfall noise peak at 15 kHz depends not only on the number of 0.8 to 1.1 mm drops present in the rainfall, but also on the wind speed and the surface roughness. This is illustrated in Figure 10 (Nystuen, 1992), which shows the ambient noise generated by 0.6 mm/hr rainfall for various wind speeds. As the wind speed increases from 0.6 m/s to 3.3 m/s, the spectral peak near 15 kHz becomes less pronounced. The reason for the observed change is that, as wind speed increases, a greater percentage of the small

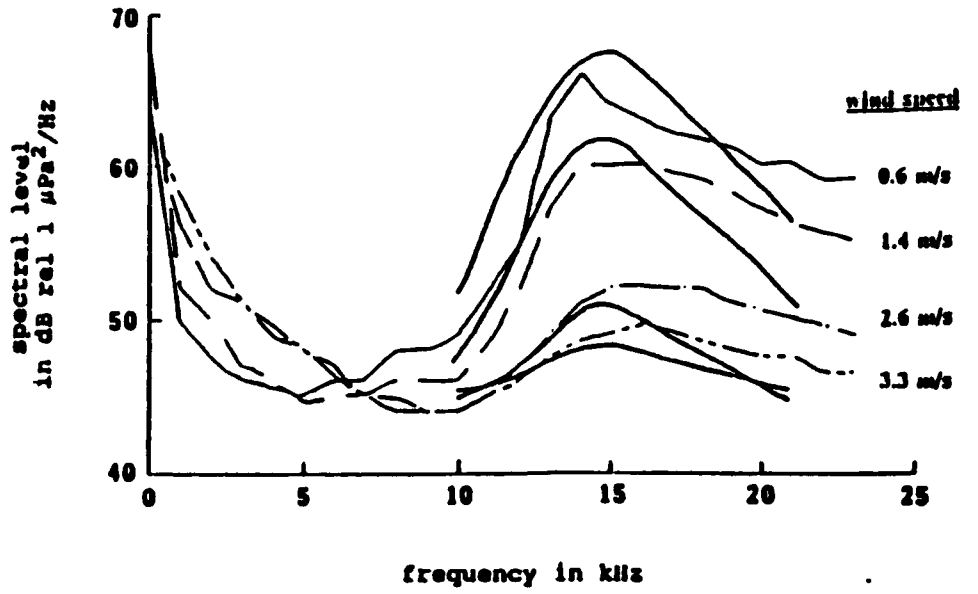

Figure 10. Effect of wind on the 15 kHz spectral peak during light rain. As wind speed increases, the 15 kHz peak becomes weaker. Predicted spectra (based on the bubble formation percentages in Table 2) are superimposed (Nystuen, 1992).

raindrops strike the surface at oblique incidence, and, as discussed earlier, the likelihood of Type I bubble formation for oblique incidence is very small. In fact, the percentage of bubbles formed at the various wind speeds shown in Figure 10 was calculated by Nystuen (1992). The calculation assumed a form for the surface roughness based on the ambient wind speed; the results are presented in Table 2. Clearly, the presence of even light to moderate winds can have an overwhelming effect on the underwater sound generated by the Type I raindrop bubbles.

TABLE 2. THE PERCENTAGE OF DROPS CREATING BUBBLES FOR DIFFERENT WIND SPEEDS (NYSTUEN, 1992)

		Wind Speed (m/s)				
		0	0.6	1.4	2.6	3.3
Drop Size (mm)	0.8	100	53	12	0.3	0.02
	0.9	100	58	15	0.8	0.1
	1.0	100	61	18	1.4	0.3

2. Observations for Moderate to Heavy Rainfall

The characteristics of the underwater acoustic signature for moderate to heavy rainfall rates is much different from that for light rainfall. Based on measurements of rainfall underwater acoustical spectra at the Ocean Test Platform (OTP) in the Gulf of Mississippi, Tan (1990) discovered that the 15 kHz peak observed in the spectrum for light rainfall is no longer present during conditions of moderate to heavy rainfall. This is illustrated by the spectrum in Figure 11, obtained during conditions of heavy convective precipitation at the OTP (McGlothin, 1991).

A positive correlation between the number of large raindrops (greater than 2.2 mm diameter) and underwater spectral levels at lower frequencies (less than about 10 kHz) has been recognized for some time. Nystuen (1986) observed at Clinton Lake, Illinois that the underwater rain noise levels at frequencies less than 10 kHz (and at higher frequencies as well) increased as the number of large raindrops increased.

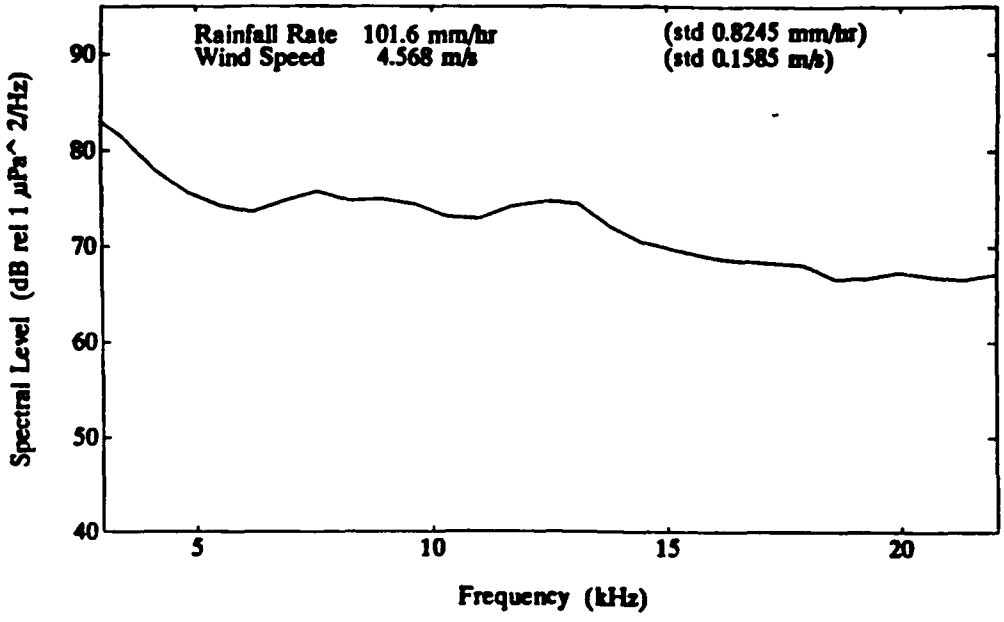

Figure 11. Underwater sound spectrum during heavy precipitation (McGlothin, 1991).

Scrimger *et al.* (1987) also observed an increase the underwater spectral levels at low frequencies with an increase in the number of large raindrops present. At the time of those studies, the mechanism for the increase in spectral levels at low frequencies with an increase in the number of large drops was unknown. It is now known that the Type II bubble generation mechanism is the most likely source of the low frequency noise generated by large raindrops.

Recent measurements of the correlation between rainfall rate and underwater spectral levels were performed by McGlothin (1991). The results are shown in

Figure 12. The correlation coefficients obtained by McGlothin are uniformly high over most of the frequency spectrum, except during events when the wind speeds are high (greater than 10 m/s). At the higher frequencies, the correlation coefficients between rainfall rate and sound level decrease for high wind speed. This is thought to be due to bubble clouds generated by breaking waves, a phenomenon which has been observed in the field (Farmer and Lemon, 1984), and studied in the laboratory (Medwin and Daniel, 1990).

McGlothin's results for events with rainfall rates greater than 150 mm/hr are shown in Figure 13. For frequencies between about 2 kHz and 10 kHz, the correlation coefficient is uniformly high (greater than 0.8) for all the events shown, even during high wind conditions. Note that for higher frequencies, the correlation coefficient decreases for all events (although the decrease is most marked with high wind present). McGlothin suggests that this may be due to subsurface bubble clouds generated by the heavy rainfall itself, which would also attenuate the high frequency rainfall noise as it propagated through the cloud.

Given the strong correlation between rainfall rates and underwater sound levels, especially below 10 kHz, and a knowledge of the sound production mechanisms of individual raindrops, it should be possible to use measurements of the underwater sound generated by rain to infer the numbers of raindrops of various sizes striking the

surface. Assuming that all or most of the rain noise that is < 10 kHz is generated by large (Type II) raindrops, a drop size distribution for the large drops can be estimated, and then extrapolated to smaller raindrop sizes. The drop size distribution obtained in this way can then be integrated to yield the total rainfall rate. This is the nature of the inverse problem of obtaining rainfall rate from the acoustical signature of the rainfall.

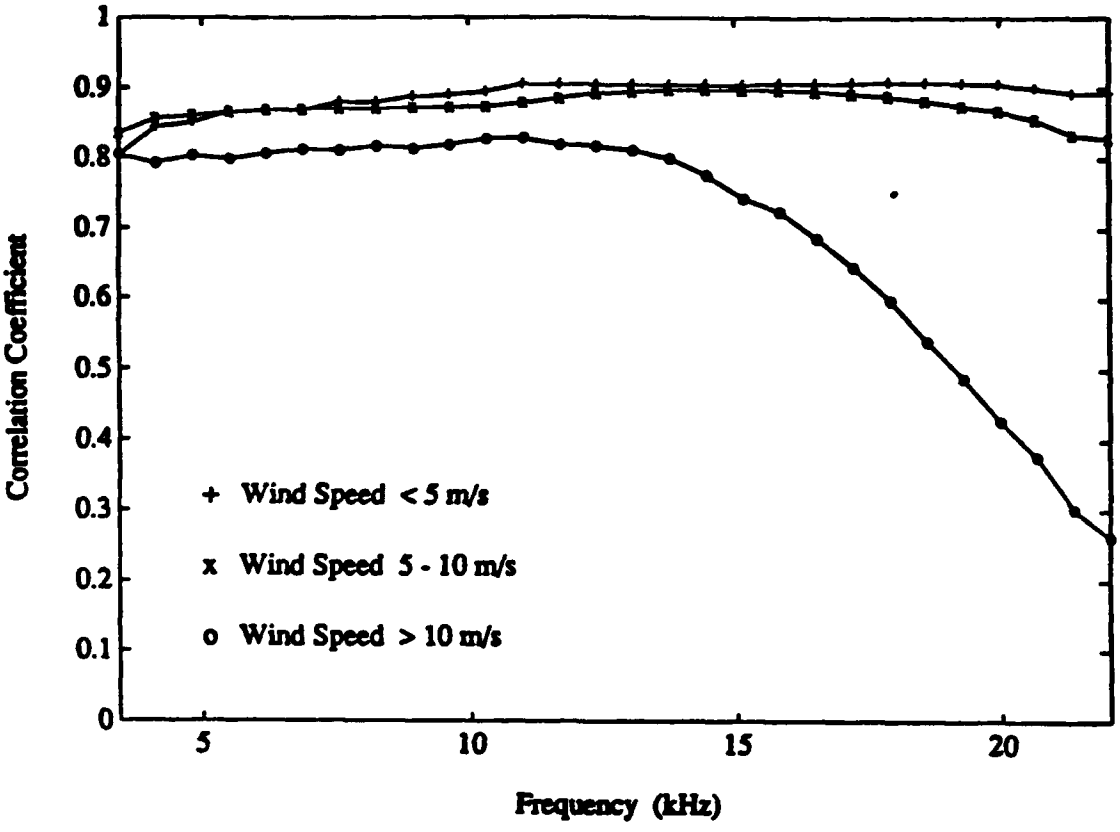

Figure 12. Correlation coefficients between underwater spectral levels and rainfall rate for the rainfall events studied by McGlothin (1991).

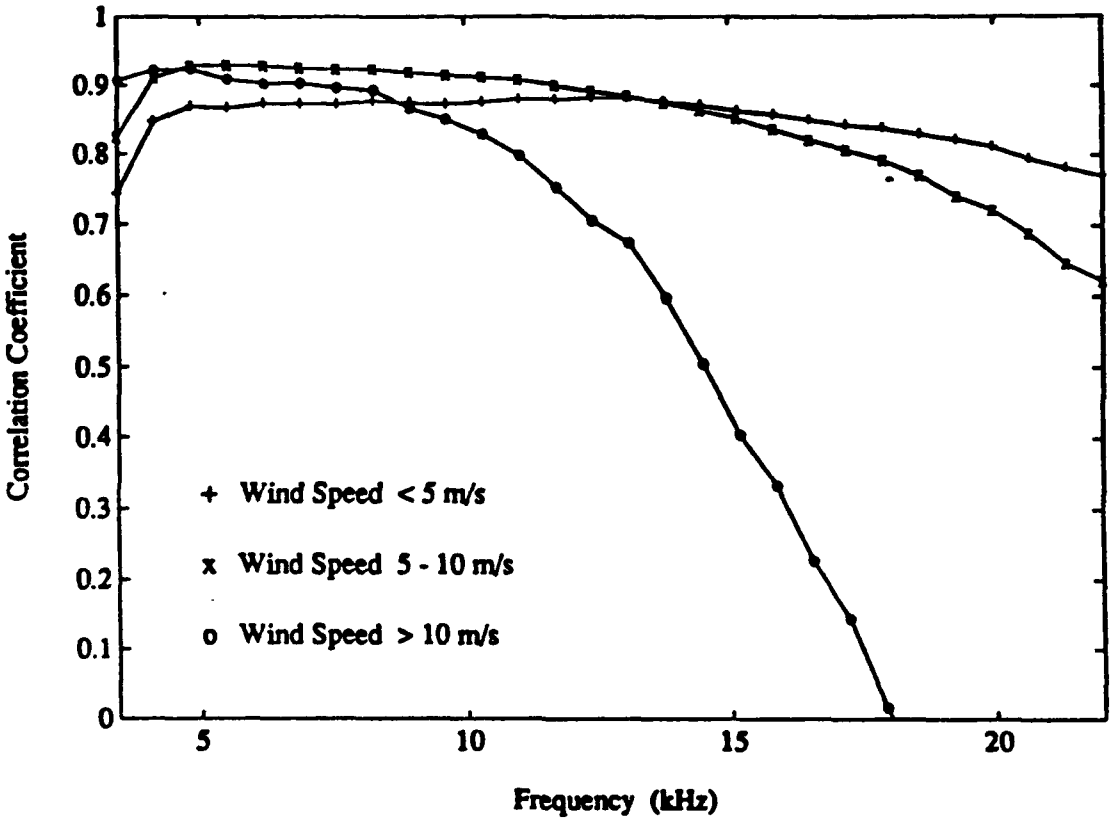

Figure 13. Correlation coefficients between underwater spectral level and rainfall rate where the rainfall rate exceeded 150 mm/hr (McGlothin, 1991).

III. CHARACTERISTICS OF THE IMPACT SOUND

A. BACKGROUND

The impact sound of individual raindrops contributes to the total underwater noise generated by rainfall at sea. Figure 14 shows a typical impact acoustic signal obtained using a hydrophone 6 cm below the surface with no electronic filtering. The two components to the impact sound are a short duration impulse and a relatively long duration plateau. The corresponding frequency spectrum is shown in Figure 15. In the frequency domain, the impulse component shows up as broadband noise and the plateau shows up as a low frequency spike. Pumphrey (1991) points out that, due to the broadband nature of the impact spectrum, any measurements of impact sound will be affected by the impulse response of the measuring equipment. To demonstrate this, the impact signal shown in Figure 14 was filtered with a 1 to 30 kHz bandpass filter (as will be explained later, these are the equipment filter settings used when measuring the bubble signals). The results are shown in Figures 16 and 17. Figure 16 shows the filtered impact signal, while Figure 17 shows the corresponding frequency spectrum. Note that the peak impulse pressure of the filtered signal is significantly less than that of the unfiltered signal, and that the plateau component of the filtered signal

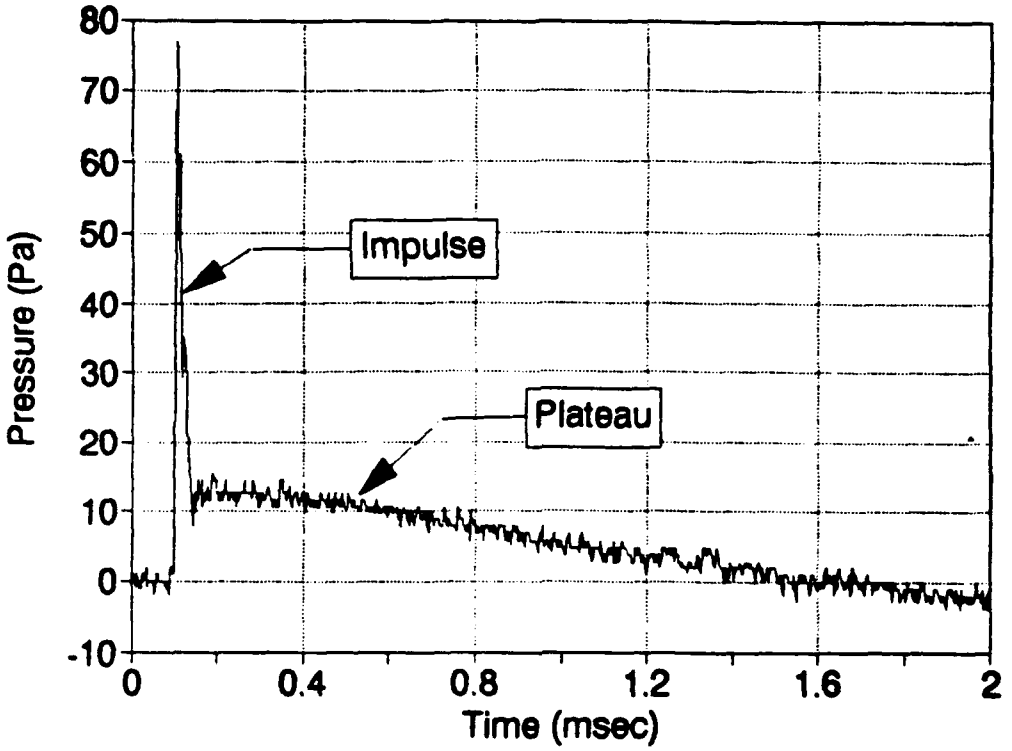

Figure 14. Laboratory measured underwater acoustical signal for a 4.6 mm diameter raindrop impact with no filtering. The hydrophone was at a depth of 5.5 cm.

is diminished. A detailed empirical study of the impact sound of raindrops was performed by Pumphrey and Crum (1989). They determined that the impulse component of the impact tended to vary with range as $1/r$, while the plateau component tended to fall off more rapidly with range (approximately as $1/r^2$). Pumphrey (1991) treats the plateau component as a near field acoustical effect, and uses this assumption to derive the corresponding far field pressure associated with the plateau. This approach contradicts the results of Nystuen (1986) who, based on numerical

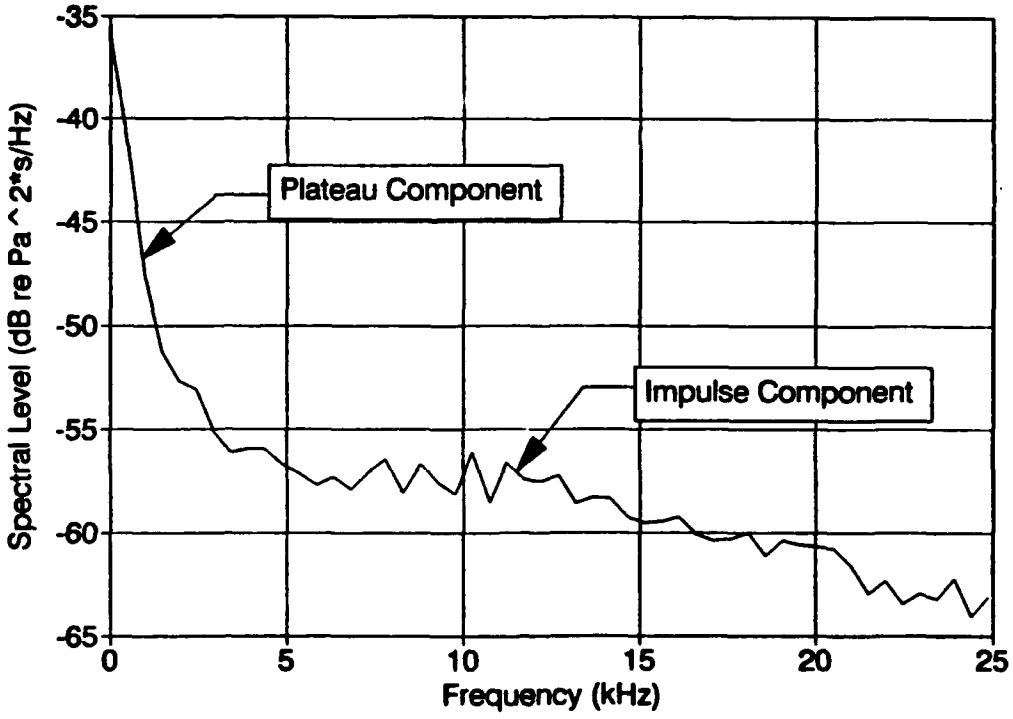

Figure 15. Frequency spectrum of the unfiltered impact signal shown in Figure 14.

simulations of a raindrop impact, asserted that the plateau is a hydrodynamic effect associated with fluid flow in the vicinity of the impact.

Laboratory measurements of the raindrop impact sound have been conducted with three objectives in mind. The first objective was to investigate some of the results obtained by other researchers pertaining to characteristics of the impact sound. The second objective was to resolve how to best treat the plateau component of the impact noise in terms of its contribution to the far field acoustic pressure (if any). The third objective was to determine the average impact frequency spectra for the various sizes

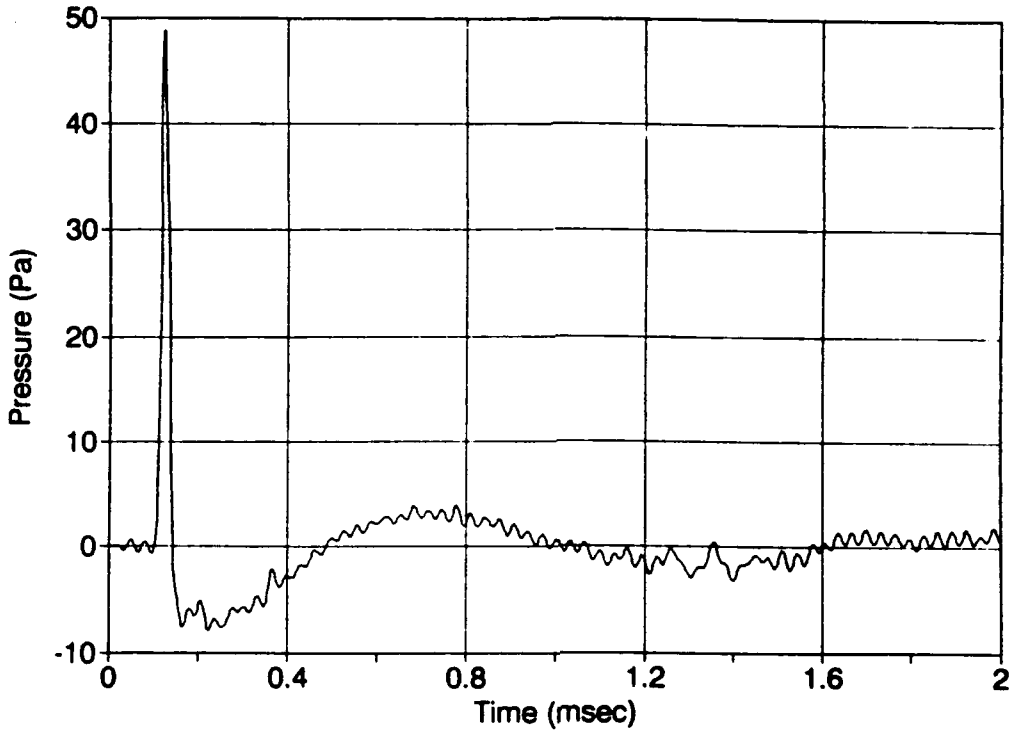

Figure 16. Effect of applying a 1 to 30 kHz bandpass filter to the impact signal. The filter causes the signal to go negative for a short time after the initial impulse.

of large raindrops as a basis for solution of the inverse problem (measuring rainfall rate from the underwater acoustical signature of large raindrops). The data collection and analysis techniques for obtaining the impact spectra were similar to those used to obtain the bubble spectra, and will be described later.

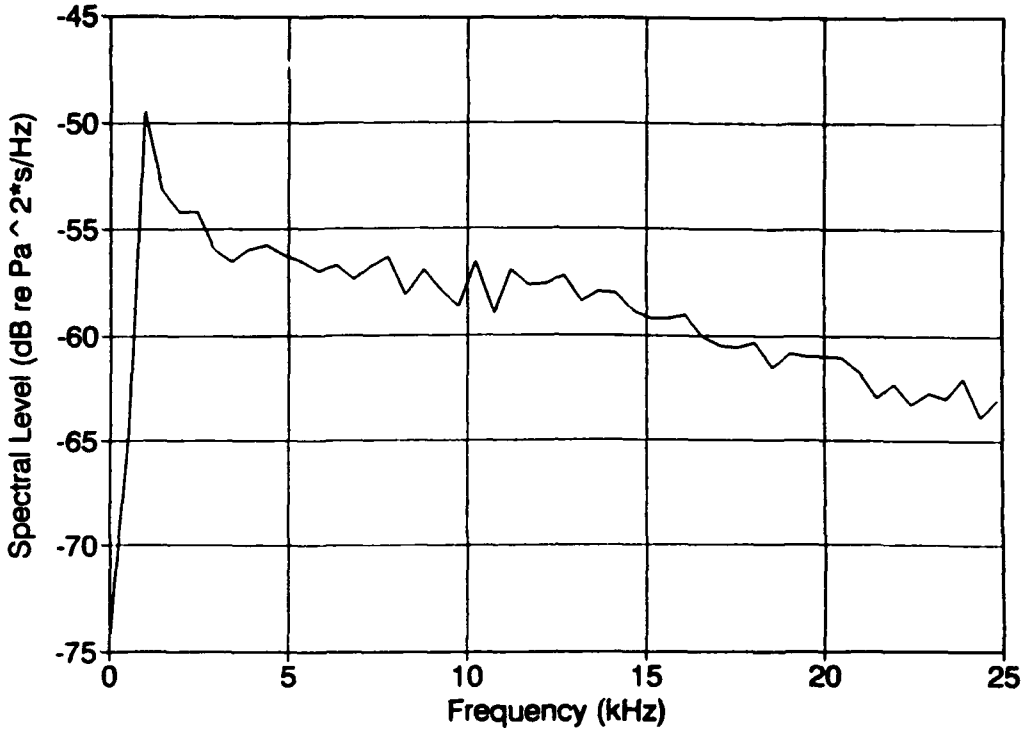

Figure 17. Frequency spectrum of the filtered impact signal.

B. EXPERIMENTAL PROCEDURES

1. Pressure vs. Range Dependence

To determine the pressure versus range dependence of the impact and plateau components, the experimental setup shown in Figure 18 was employed. A set of 25 raindrops of 4.6 mm diameter were launched from a height of 26 m in a ventilation shaft that serves as a drop tower. The 26 m drop height ensures that the large 4.6 mm drops strike the surface at terminal velocity (as does natural rainfall). At the base of the tower is a redwood tank, which is 1.5 m deep and 1.5 m in diameter.

The tank is lined with redwood wedges to reduce reverberation from the tank walls. For this experiment, the tank was filled with fresh water. The temperature of the tank water was 30° C. The device used to generate the drops consisted of a calibrated pipette tip attached to an intravenous drop bottle, with a drop accuracy of ± 5 percent by volume.

To measure the acoustic signal, two hydrophones were used. The first hydrophone was located at a depth of 5.5 cm, and consisted of a laboratory constructed hydrophone with a lead zirconate acoustic element and a nominal sensitivity of -206 dB re V/μPa. The second hydrophone was an LC-10 located directly below the first hydrophone and at a depth of 22 cm. The nominal sensitivity of the lower hydrophone was -198 dB re V μPa. The hydrophone signals were then amplified by a factor of 100 using HP465A amplifiers, and patched to Computerscope, a digital multichannel analyzer mounted in an IBM PC/XT computer. Computerscope's maximum sampling rate is 1 MHz divided by the number of input channels used (up to 16 channels are available). The maximum rate of 500 kHz was used for sampling the signal from the two hydrophones.

The difference in the arrival time of the impact signal at the two hydrophones was used to calculate the range and angle from the point of impact to the

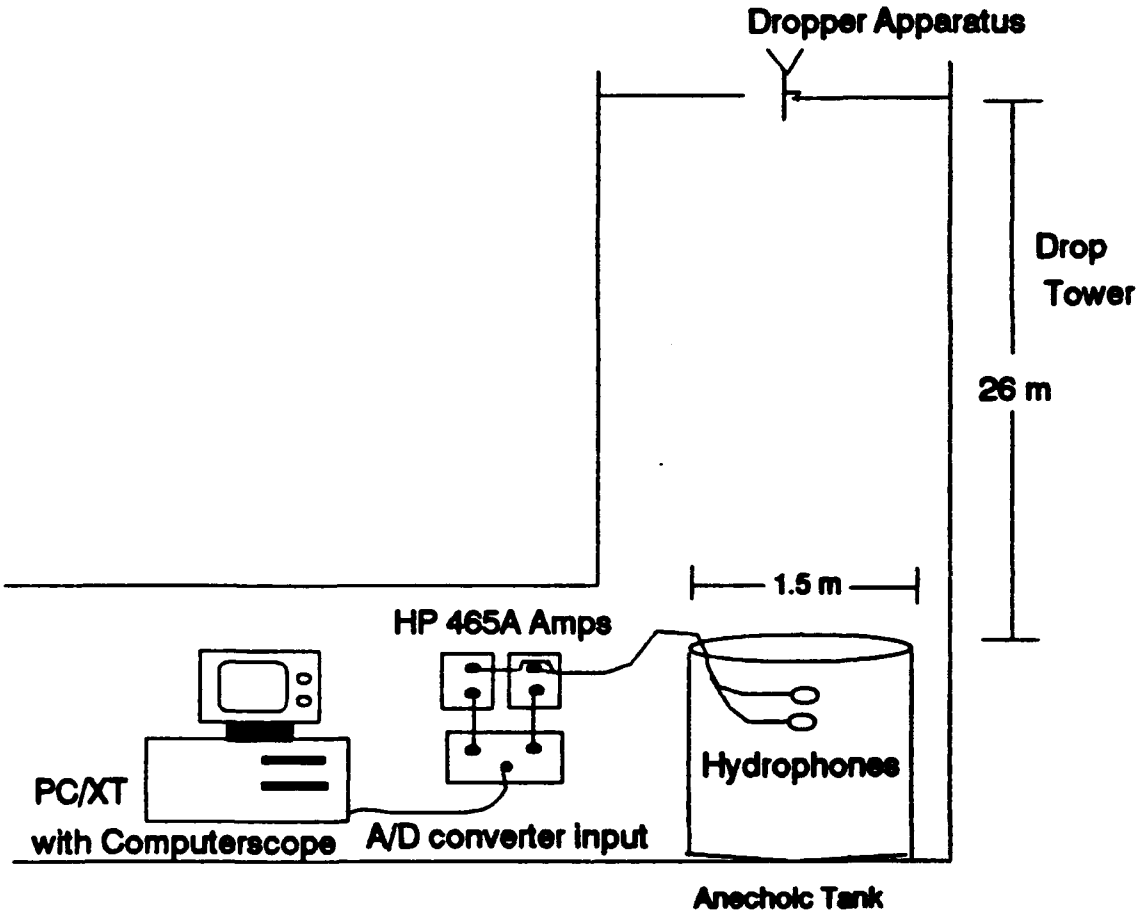

Figure 18. Schematic diagram of the experimental setup for the impact pressure vs. range measurement.

position of the hydrophone. The geometry of the problem is shown in Figure 19. The horizontal distance X in cm is given by:

$$X = \sqrt{\left[\frac{H_2^2 - H_1^2 - c^2 \cdot \Delta t^2}{2 \cdot c \cdot \Delta t}\right]^2 - H_1^2} \qquad (4)$$

where Δt is the arrival time difference (sec), c the speed of sound in water (cm/sec), H_1 and H_2 the hydrophone depths (cm), and $c \cdot \Delta t$ the range difference from the impact to the two hydrophones. After solving for X, the ranges R_1 and R_2, and the angles θ_1 and θ_2 to the respective hydrophones were determined from the equations $R_1 = \sqrt{H_1^2 + X^2}$ and $\theta_2 = \arctan(X / H)$.

2. Radiation Pattern Measurement

The impact radiation pattern was investigated using the setup shown in Figure 20. For this experiment, an array of 4 hydrophones was constructed. The hydrophones were attached to a semicircular ring of 8 cm radius, and positioned at angles of 0°, 20°, 40°, and 60° with the vertical. The hydrophone output signals were again amplified by a factor of 100, and patched to Computerscope, where the signals were sampled at a rate of 250 kHz. Raindrops of 4.6 mm diameter were dropped from a height of 3 m into an anechoically lined fresh water tank containing the hydrophone

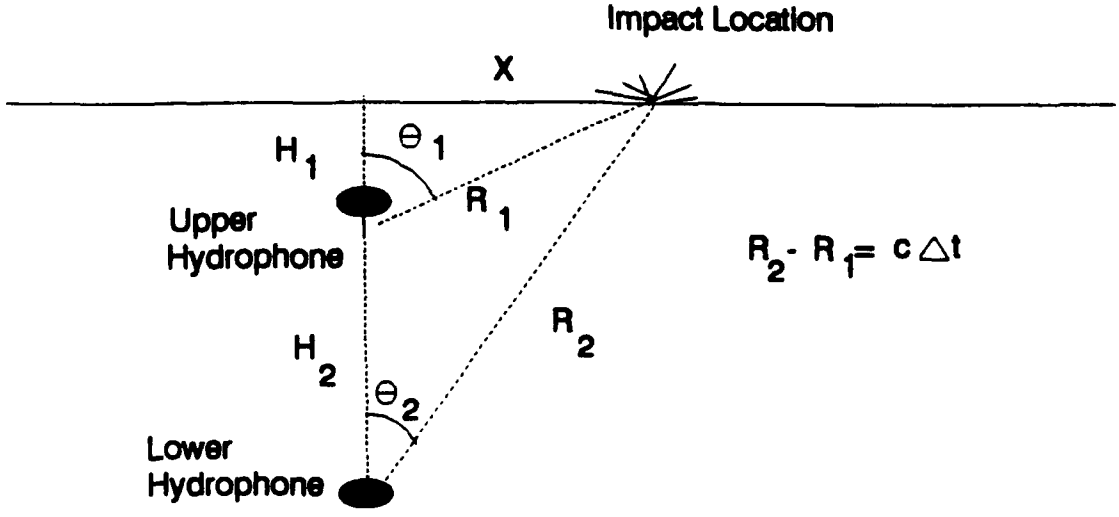

Figure 19. Geometry of the impact pressure vs. range measurement.

array. The reduced drop height was necessary to ensure that a sufficient number of drops landed directly over the center of the array.

3. Peak Impact Pressure vs. Impact Velocity

To investigate the relationship between impact velocity and impact acoustic pressure, another experiment was conducted using a setup similar to that for the radiation pattern measurement, but using only one hydrophone directly below the point of impact. The impact velocity of the drops was varied by adjusting the height of the dropper. The relationship between dropper height and impact velocity is given

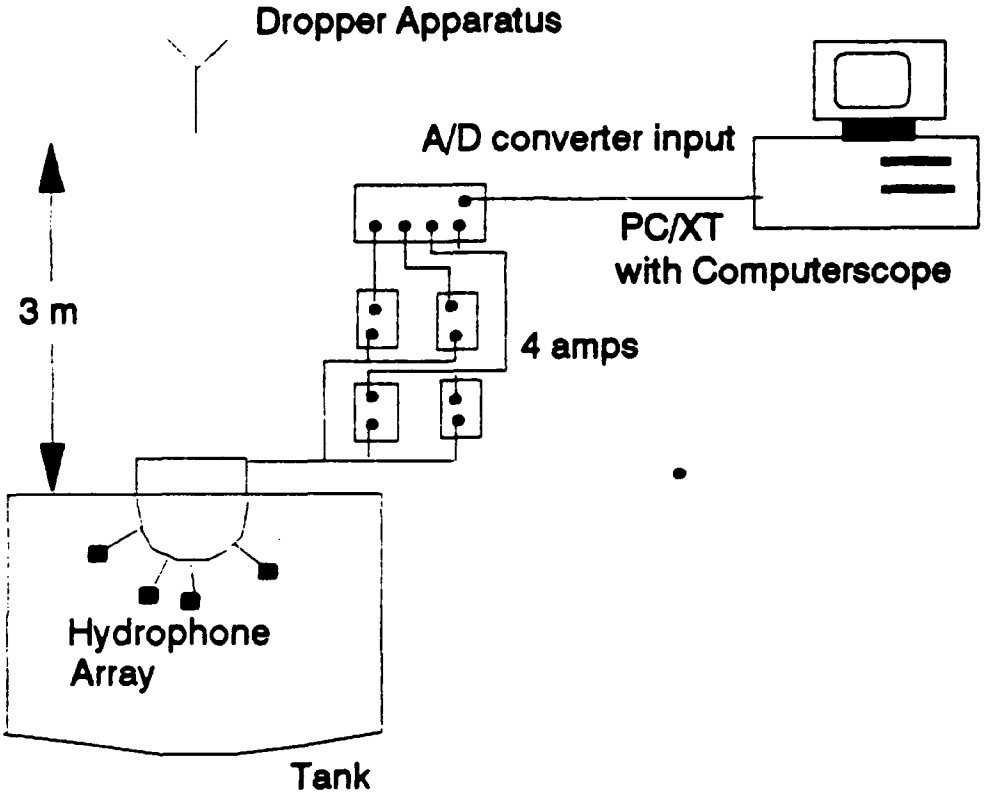

Figure 20. Schematic diagram of the experimental setup for impact radiation pattern measurement.

by the following equation:

$$v_I = v_T \cdot (1 - \exp(\frac{-2gh}{v_T^2}))^{1/2} \quad (5)$$

where v_I is the impact velocity in m/s, v_T is the terminal velocity in m/s (9.1 m/s for 4.6 mm diameter drops), g the gravitational constant in m/s^2, and h the drop height in m (Pumphrey and Crum, 1989).

C. RESULTS

1. Impact Radiation Pattern

The impact radiation pattern was measured for two reasons. First, for the pressure vs. range experiment, the measured impact pressures needed to be corrected to the corresponding on-axis values. Second, the radiation patterns of the impulse and plateau components of the impact sound needed to be compared to determine if there were any differences. For a simple acoustic source in water located near the surface, the radiation pattern may be expected to be that of a dipole, due to the presence of a virtual image of the source above the surface of the water and 180° out of phase with the source. This effect is illustrated in Figure 21. The far field pressure radiated by an acoustic dipole is given by:

$$P(r,\theta,t) = \frac{D}{r} \cdot \cos\theta \cdot e^{i(\omega t - kr)} \quad (6)$$

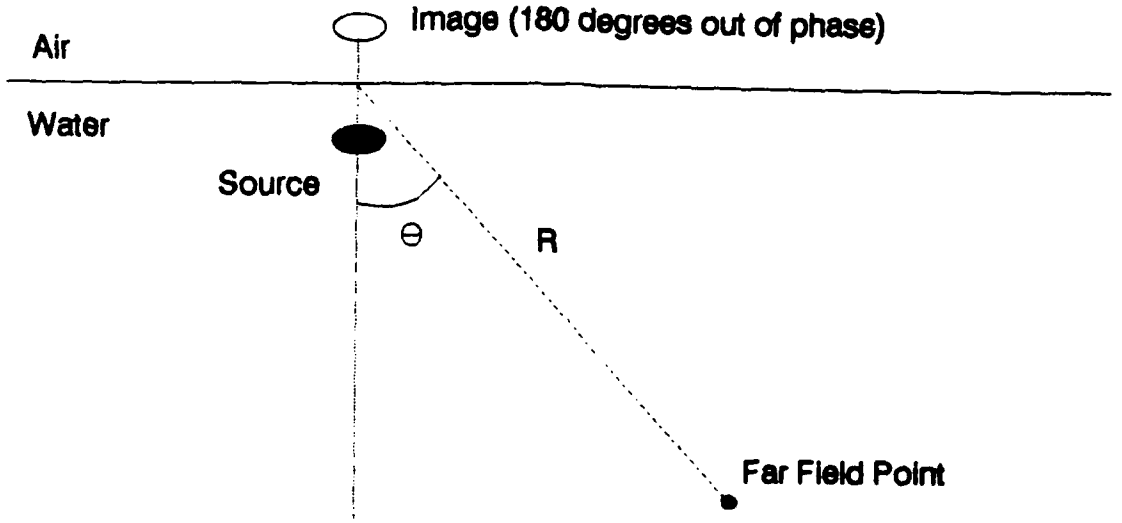

Figure 21. Negative image of a simple acoustic source near a pressure release boundary (the air-water interface). Resulting pressure field is dipolar in nature.

where D is the dipole source strength (Pa · m), r is the range, θ is the angle between the dipole axis and the range vector to the far field point, and the exponential term gives the phase variation with distance and time. Thus, the acoustic pressure radiated by a compact dipole source region of this nature should vary as cos θ, where θ is the angle with the vertical below the source. If the radiation pattern does not exhibit a cos θ dependence, the source region may be of a different nature (such as monopole or quadropole), or the pressure field may be of nonacoustic origin.

Results of the radiation pattern measurements are shown in Figures 22 and 23 for the impulse and plateau components respectively. The figures show the normalized pressure vs. angle for three different impacts, along with the theoretical

dipole radiation pattern. The pressures have been normalized to the on axis (zero degree) value. The radiation patterns of both the impulse and plateau tend to conform to the cos θ dependence of a dipole. This can also be seen in Figure 24, which shows the pressure time series obtained at the 0° and 40° hydrophones for a single impact. The two time series have been superimposed, and the 40° hydrophone signal has been corrected by dividing by the cosine of 40 degrees. The magnitudes of the superimposed signals for both the impulse and the plateau are nearly identical.

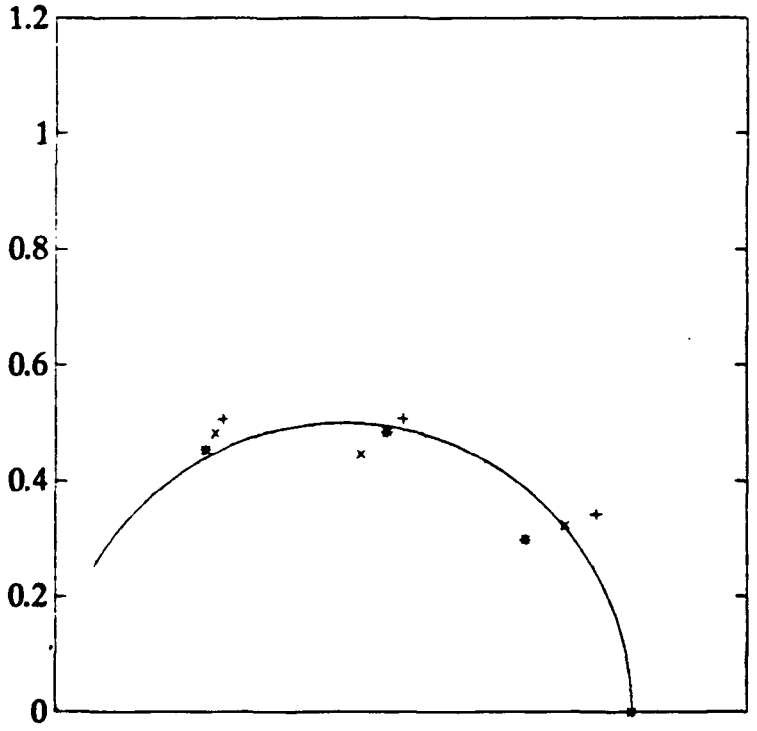

Figure 22. Polar radiation pattern of the normalized impulse pressure for three impacts. The dipole axis is horizontal.

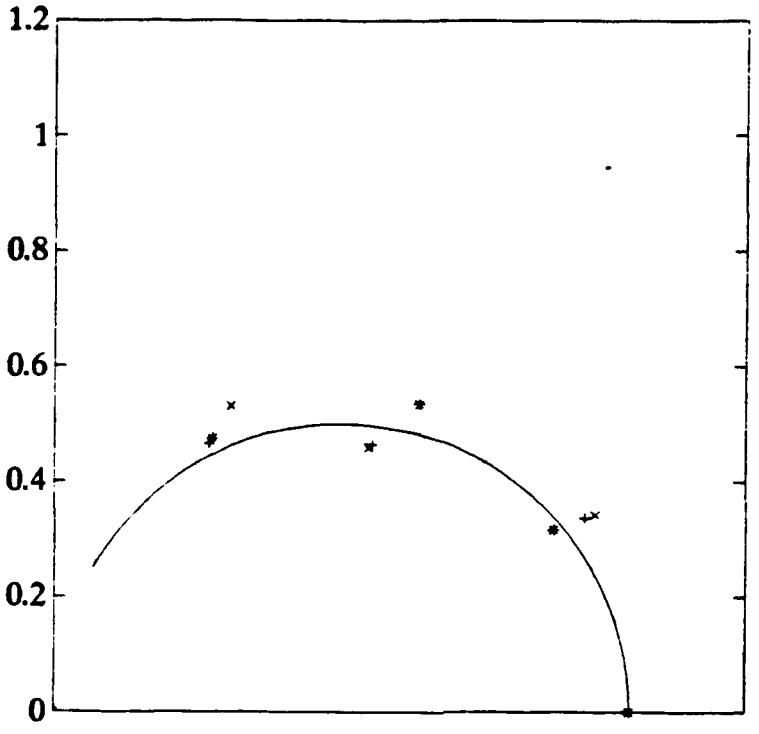

Figure 23. Polar radiation pattern of the normalized plateau pressure for three impacts. The dipole axis is horizontal.

While the impulse and plateau components of the impact sound both appear to have a dipole radiation pattern, it is not necessarily true that the plateau pressure is of acoustical origin. If the plateau pressure is due to incompressible (hydrodynamic) fluid flow associated with the impact, then the cos θ dependence may result from the fluid flow below the impact being predominantly in the vertical direction, since the projection of the fluid velocities into directions away from the vertical will also vary as cos θ. A numerical study of raindrop impacts conducted by

Nystuen (1986) supports the latter contention. Results discussed later refer to the pressure versus velocity finding.

2. Impact Pressure vs. Range Variation

The impact pressure time series obtained at the upper and lower hydrophones for the pressure vs. range experiment are shown in Figure 25. The upper hydrophone was 5 cm below the surface, while the lower hydrophone was 22 cm below the surface. The impact shown landed directly above the hydrophones, so any

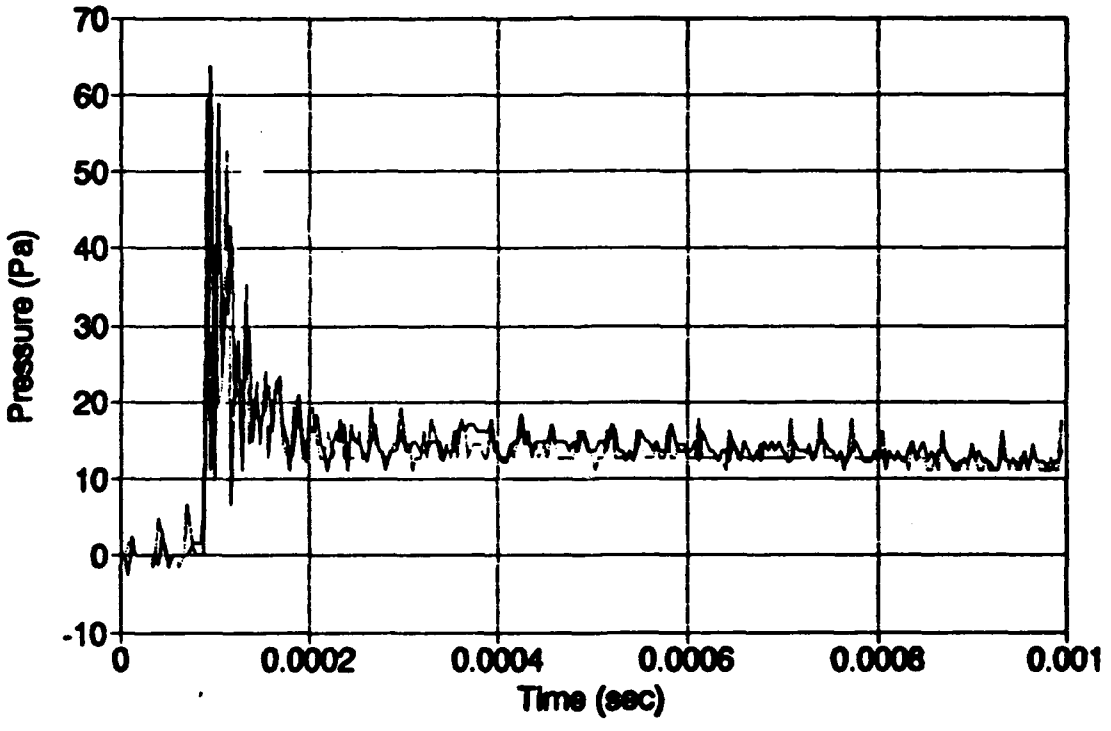

Figure 24. Impact signal in freshwater at the 40° hydrophone (dashed), corrected for cos(40°), superimposed on the impact signal at the 0° hydrophone (solid). Range to the hydrophones was 8 cm.

difference between the two hydrophone signals can only be attributed to the differences in range and in hydrophone sensitivities. Note that the relative magnitude of the impulse and plateau components is very different for the two hydrophones. At the lower hydrophone, the plateau component is barely discernible, while at the upper hydrophone, the plateau component is about 1/3 as large as the impulse component. This suggests that the impulse and plateau components do in fact have different range dependencies.

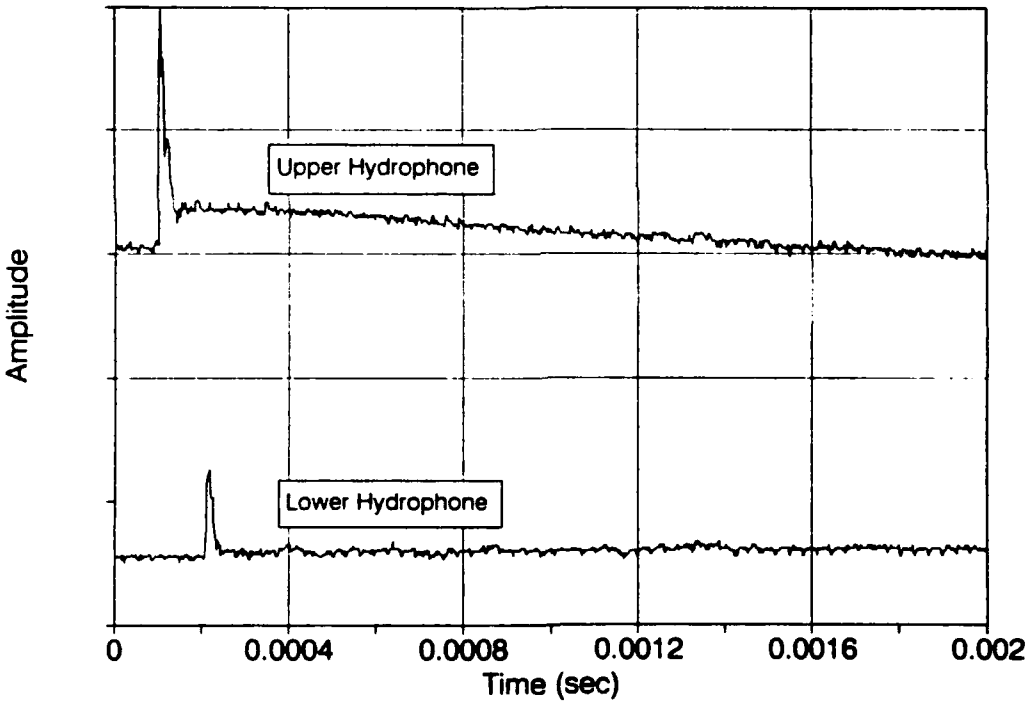

Figure 25. Pressure signals at the upper (top) and lower (bottom) hydrophones for an impact directly overhead.

Plots of axial pressure vs. range for both the plateau and peak impulse pressure are shown in Figure 26 for 4.6 mm diameter raindrops at terminal velocity. The pressure values were calculated using the following equation:

$$P_{axial} = \frac{V_{hyd}}{M \cdot G \cdot \cos\theta} \tag{7}$$

where V_{hyd} is the output voltage, M is the hydrophone sensitivity (V/Pa), and G is the amplifier voltage gain (100). The cos θ term in the denominator is used to correct for the dipole angular variation of the pressure fields. The plateau pressures were recorded 200 μsec after the peak impulse pressure. The line fitted through the impulse data has a slope corresponding to a $1/r$ range dependence, while the line fitted through the plateau data has a slope corresponding to a $1/r^2$ range dependence.

While there is much scatter in the data, the difference in range dependence between the two components of the impact sound can readily be seen from the increasing spread between the impact and plateau pressures with range. The impulse pressure varies approximately as $1/r$, while the plateau pressure varies approximately as $1/r^2$. The data points for the deeper hydrophone, however, tend to fall below the theoretical curves. One reason for this may be differences in response of the two hydrophones to the very rapid pressure change associated with the impulse (on the order of 4 to 8 μsec).

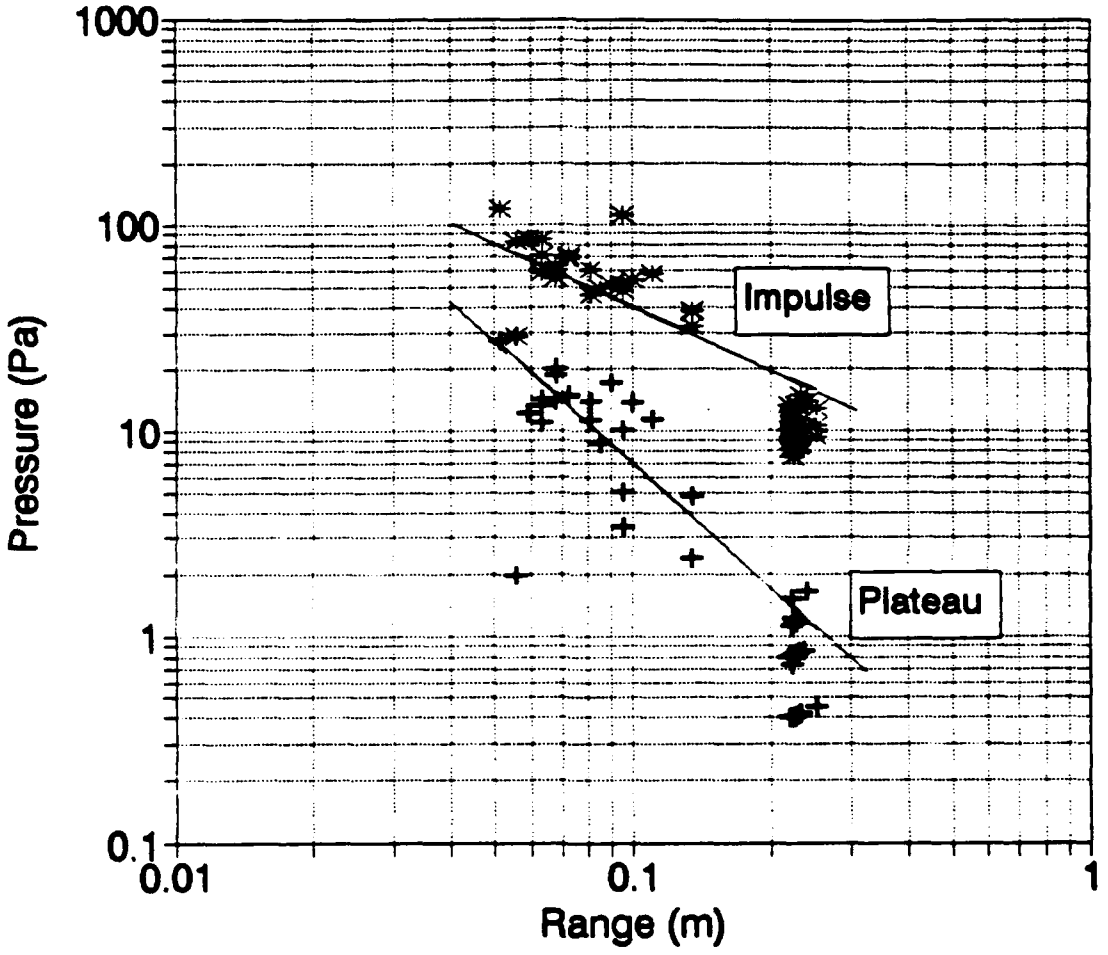

Figure 26. On-axis pressure vs. range for the impulse and plateau components (4.6 mm drops). The hand fitted curves show a $1/r$ dependence (impulse) and $1/r^2$ dependence (plateau).

The rapid decrease of plateau pressure with range indicates that the plateau is a near field effect of either acoustic or hydrodynamic origin. The $1/r$ variation of the much larger impulse pressure, though, agrees with the expected far field pressure variation of an acoustic dipole. Therefore, the contribution of the plateau to the measured signal at a distant hydrophone will be negligible when compared with the far field contribution of the impulse.

3. Dependence of Impact Pressure on Raindrop Velocity

Franz (1954) asserted that the impact pressure of a raindrop would be similar to that of a rigid sphere striking a water surface, for which the initial impact pressure at a range r below the sphere would be given by:

$$p = (\frac{\rho \cos\theta}{rc}) \cdot v^3 \cdot (a - z_d) \qquad (8)$$

where v is the impact velocity, r is the range, a is the radius of the sphere, c is the sound speed, ρ is the fluid density, and z_d is the depth of penetration of the sphere. The peak impact pressure would occur at time zero, and would be proportional to v^3. A numerical analysis of raindrop impacts (Nystuen, 1986), however, revealed that the rigid sphere model is oversimplified. One flaw is the sphericity assumption; actual large raindrops more closely resemble oblate spheroids that are flattened at the base. Nystuen's numerical results indicate that the drop shape can have a significant effect

on the underwater pressure generated by a drop, as shown in Figure 27 (the peak impulse pressure predicted numerically is about three times as large for the flattened drop as it is for the spherical drop). Nystuen also observed that the initial impact pressure in the immediate vicinity of the impact varied as v rather than as v^3 for a given drop shape.

Laboratory measurements of initial impact acoustic pressure (impulse pressure) as a function of terminal velocity tend to agree with Franz's theory. The drop shape, however, cannot be varied independently of the velocity for the laboratory measurements. Pumphrey (1989) empirically determined the peak impulse pressure of the impact to vary as the 2.7 power of velocity. His experiments were performed using drops of 2.52 and 3.8 mm diameter. *Figure 28* shows the results of the peak impulse pressure vs. impact velocity experiment using 4.6 mm diameter drops. The slope of the line fitted to the data corresponds to pressure varying as the 3.5 power of the velocity. The reason the value obtained here is larger than Pumphrey's may be due to increased flattening of the large 4.6 mm diameter drop with increasing velocity, since the flattening is more pronounced for larger drops (Pruppacher and Pitter, 1971). The reason why Nystuen's numerical model of raindrop impacts fails to correctly predict the impact pressure's dependence on impact velocity is uncertain, but it may be due to the fact that Nystuen's numerical simulations of impact pressure were for field points

in the immediate vicinity of the impact (at distances on the order of mm) rather than in the far field of the impact source. The characteristics of the proximal sound field for the impacts are expected to differ significantly from the far field characteristics.

The dependence of the peak impulse pressure on the size and velocity of a raindrop has important implications for the relative contribution of different size raindrops to the total underwater sound generated by rainfall. Assuming a $v^3 \cdot d$ dependence of peak pressure on drop diameter and terminal velocity, a 5.0 mm diameter drop will have an impulse peak pressure 54 times (or 35 dB greater than) that of a 1.0 mm diameter drop. Thus, despite their smaller numbers, the impact sound radiated by the larger raindrops (in excess of 2 mm diameter) can make a significant contribution to the total rainfall impact noise.

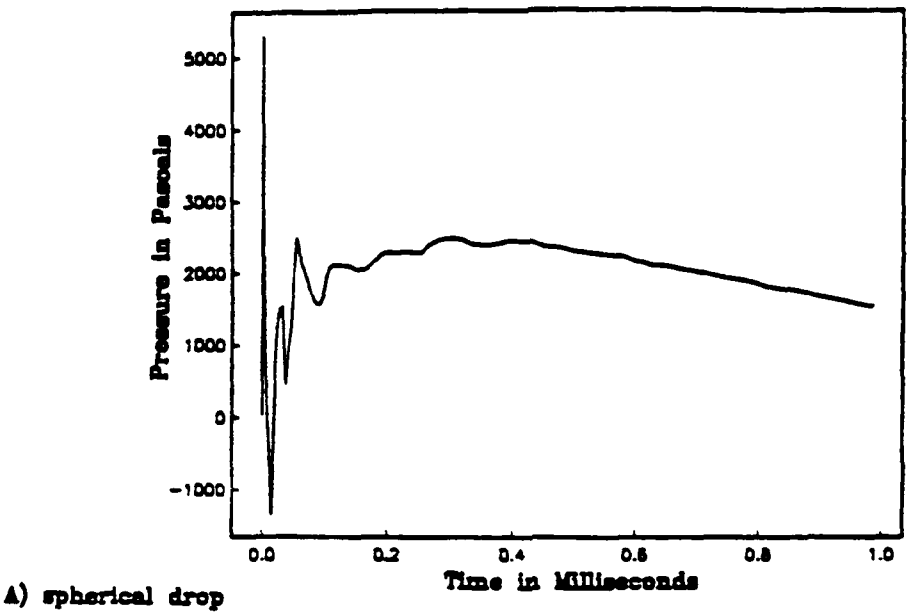

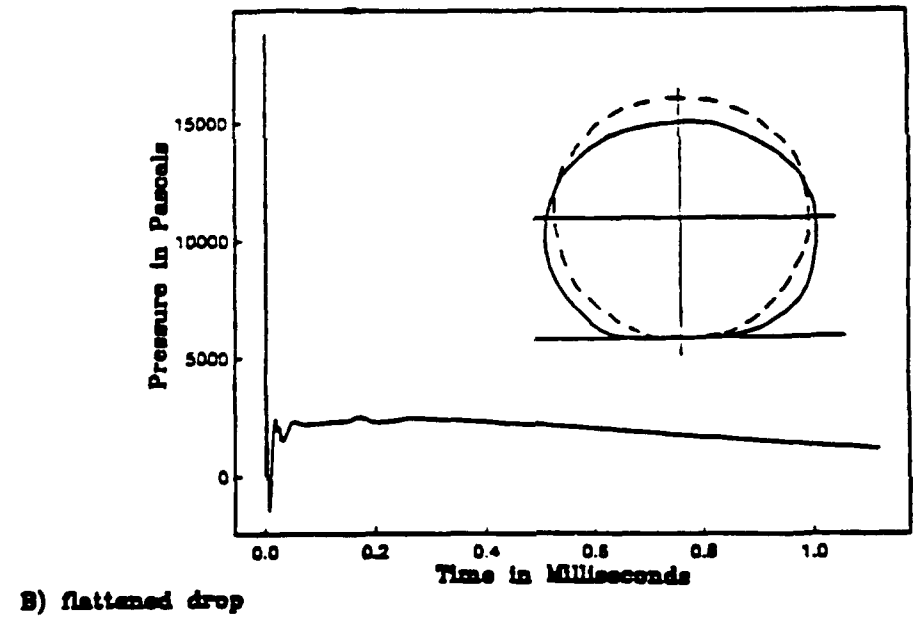

Figure 27. Numerical prediction of the effect of drop shape on the on-axis pressure directly beneath the point of impact for a 3.0 mm diameter raindrop . A realistic flattened drop shape is shown in the lower figure (Nystuen, 1986).

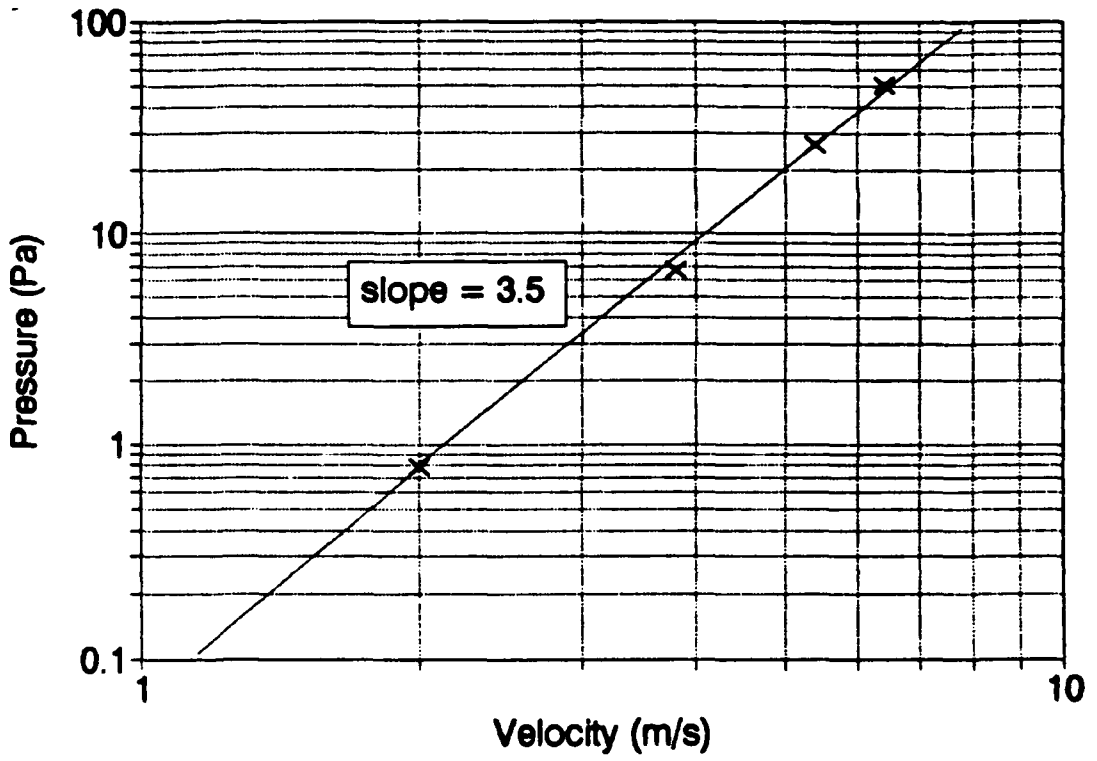

Figure 28. On-axis peak impulse pressure vs. impact velocity for 4.6 mm diameter raindrops in freshwater. The hydrophone depth was 1.5 cm.

IV. ENERGY SPECTRA FOR LARGE RAINDROPS IN SALTWATER

A. PURPOSE

As mentioned earlier, based on the work of Snyder (1990) and Jacobus (1991) there is reason to believe that much of the underwater noise generated by rainfall during moderate to heavy rainfall conditions is due to bubble and impact sound generated by large raindrops. Therefore, additional measurements have been made of the energy spectral levels of the underwater sound due to individual raindrops, over the size range of drops which produce Type II bubbles (2.2 mm diameter and larger). Once the underwater sound energy generated by individual raindrops is known as a function of drop size, the contribution to the underwater sound from individual drops can be summed to obtain a predicted acoustic signature for a given rainfall rate.

Measurement of the underwater sound energy spectra for various sizes of large raindrops was first accomplished by Jacobus (1991). One of the average spectra obtained by Jacobus for 4.2 mm diameter drops is shown in Figure 29, which shows the impact contribution to the intensity spectrum as well as the total spectrum (bubble and impact). Note that the impact spectrum is virtually insignificant when compared to the spectrum that includes the bubble noise.

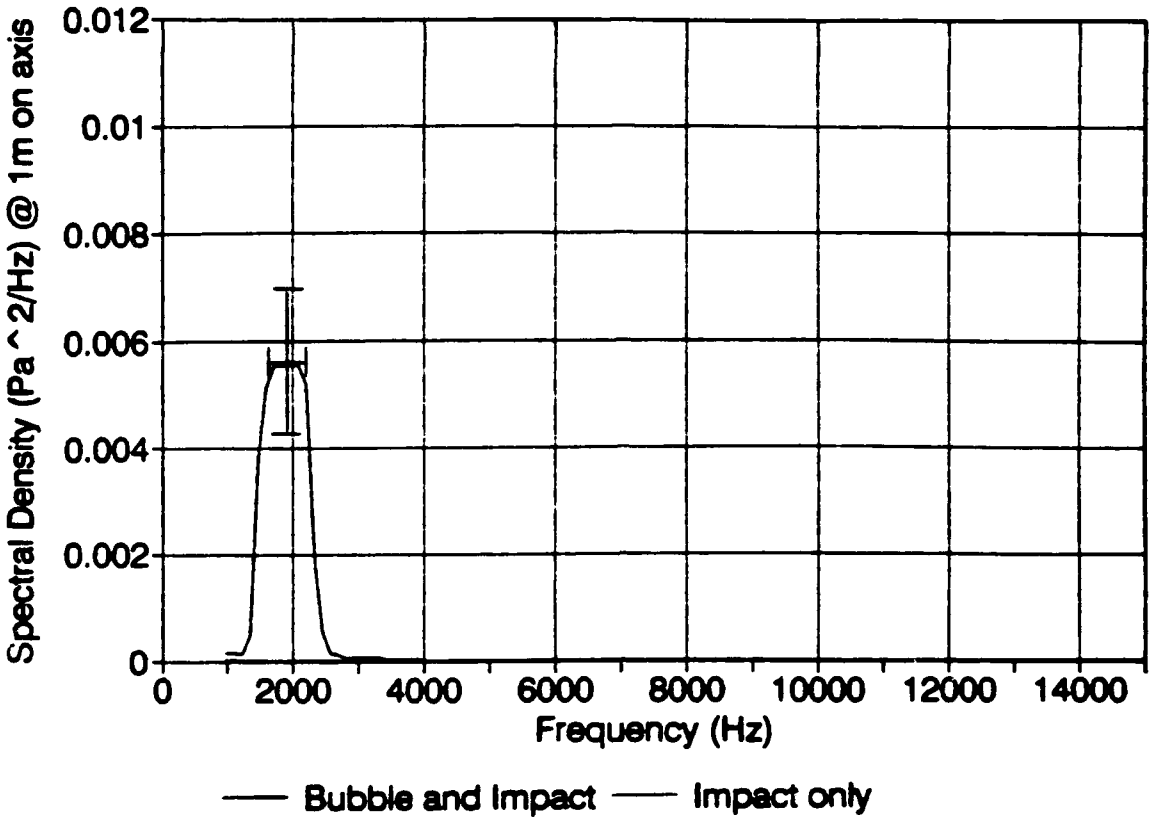

Figure 29. Impact and bubble components of the intensity spectrum for 4.2 mm diameter raindrops, as measured by Jacobus (1991). The impact spectrum is very close to the x axis.

The spectra obtained by Jacobus, however, are insufficient for predicting underwater acoustic levels for rainfall. A careful review of Jacobus' work revealed that he applied a Hamming window to his measurements of the bubble pressure signals prior to computing the intensity spectra of the bubbles. While his purpose for windowing his pressure signals was reasonable (to minimize leakage of the bubble energy to sidelobes in the frequency domain), he failed to account for the effect that

using a Hamming window would have in reducing the total measured intensity of the signal. For stationary random processes, the coherent processing loss (Harris, 1976) due to use of a Hamming window can be compensated for, but the bubble pressure signal is transient in nature, and the usual coherent loss factor cannot be directly applied.

To assess the effect of applying a Hamming window to a Type II bubble pressure signal, an idealized signal was used. The idealized bubble pressure signal is given by:

$$p(t) = e^{-\alpha t} \cdot \cos(2\pi f_o t) \tag{9}$$

where f_o is the bubble resonance frequency, and α is the amplitude decay rate. For the test case, f_o was taken to be 2000 Hz and α was taken to be $(5 \text{ msec})^{-1}$, a value close to the theoretical decay rate for a 2000 Hz bubble in water. The analytic solution for the Fourier Transform of the pressure signal is given by:

$$P(f) = \frac{2\pi jf + \alpha}{(2\pi jf + \alpha)^2 + (2\pi fo)^2} \tag{10}$$

and so it is possible to compute the theoretical intensity spectrum of the ideal infinite duration bubble signal for the sake of comparison. A discrete finite form of the ideal pressure signal was generated using MATLAB (a mathematics program), with a simulated sampling rate of 250 kHz and a total record length of 16.4 ms (4096 points). The simulated pressure signal is shown in Figure 30. Figure 31 shows the same signal

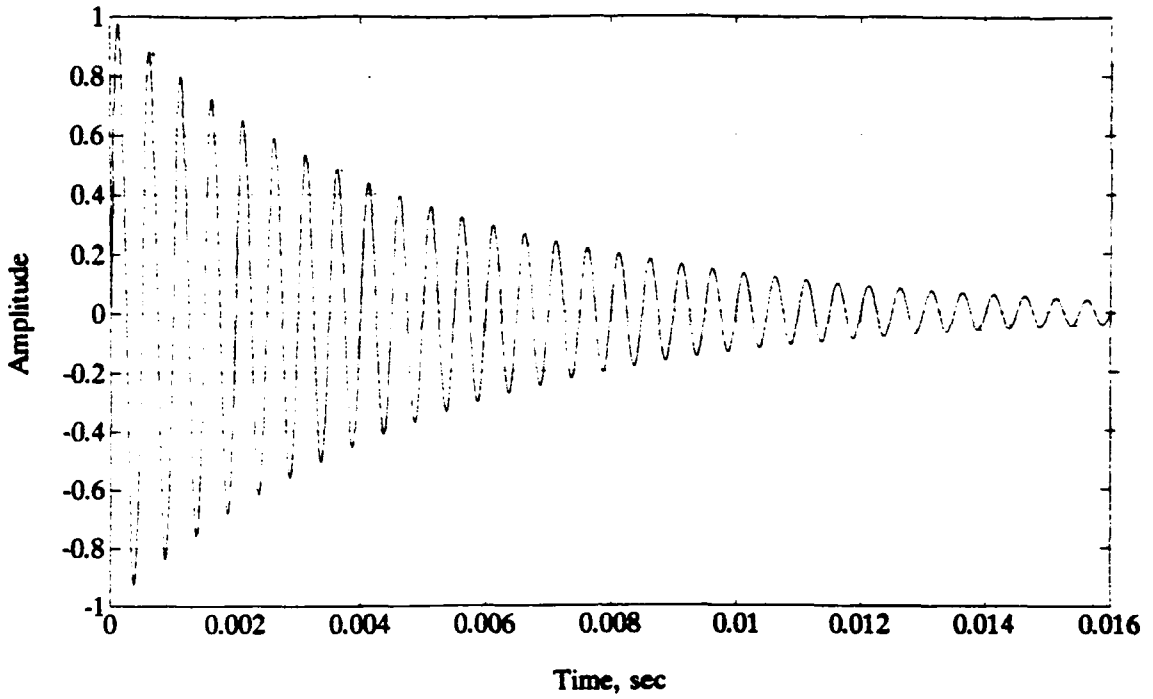

Figure 30. Theoretical bubble signal with a Rectangular window.

after a Hamming window has been applied. The energy spectra of both the unwindowed (or rather, the Rectangular windowed) signal and of the Hamming windowed signal were calculated using the Discrete Fourier Transform, and compared to the theoretical intensity spectrum based on the analytic expression for the Fourier Transform. The result is shown in Figure 32, which shows the spectral peak at 2000 Hz due to the bubble. The spectrum obtained using the rectangular window is very similar, both in shape and magnitude, to the theoretical spectrum. The spectrum obtained using the Hamming window, however, differs markedly both in shape and

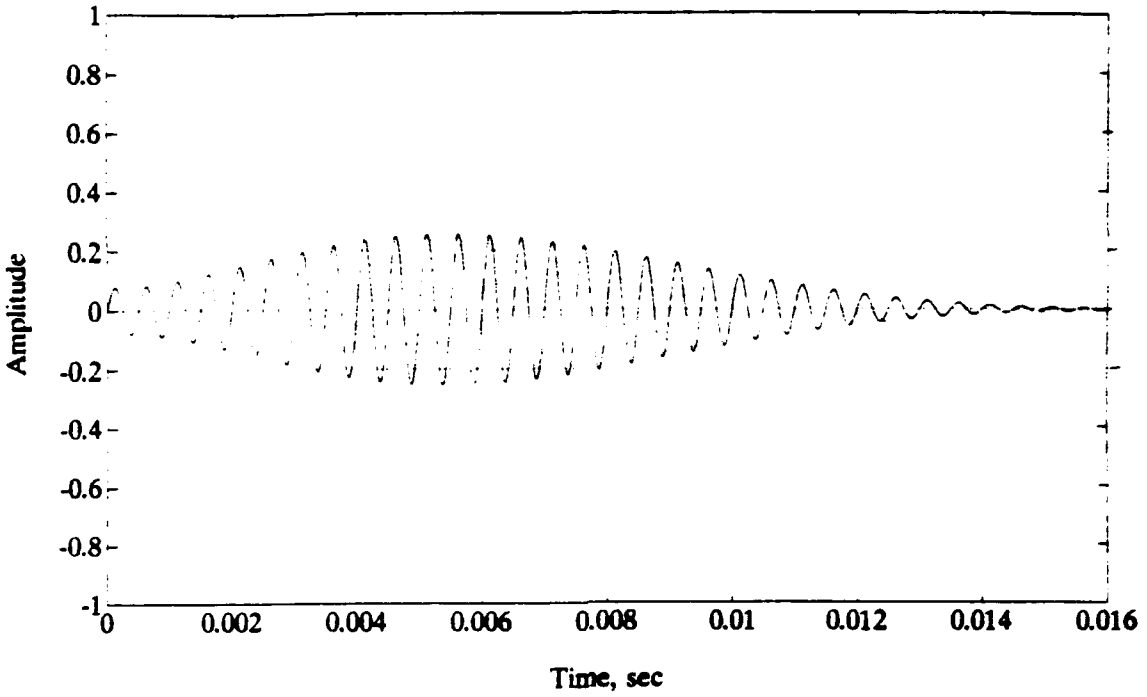

Figure 31. Pressure signal after applying a Hamming window.

magnitude from the theoretical bubble spectrum. In fact, the ratio of the total sound intensity using the Hamming window to the total sound intensity using the Rectangular window is about 0.13. Clearly, the effect of using a Hamming window makes Jacobus's results for the bubble spectra quantitatively unreliable.

Also, the number of bubble signatures collected by Jacobus for each raindrop size was relatively small from a statistical standpoint (he collected about 30 samples for each drop size). To obtain a more reliable estimate of the average spectrum for each raindrop size, the goal here was to obtain 100 bubble signatures for each of six

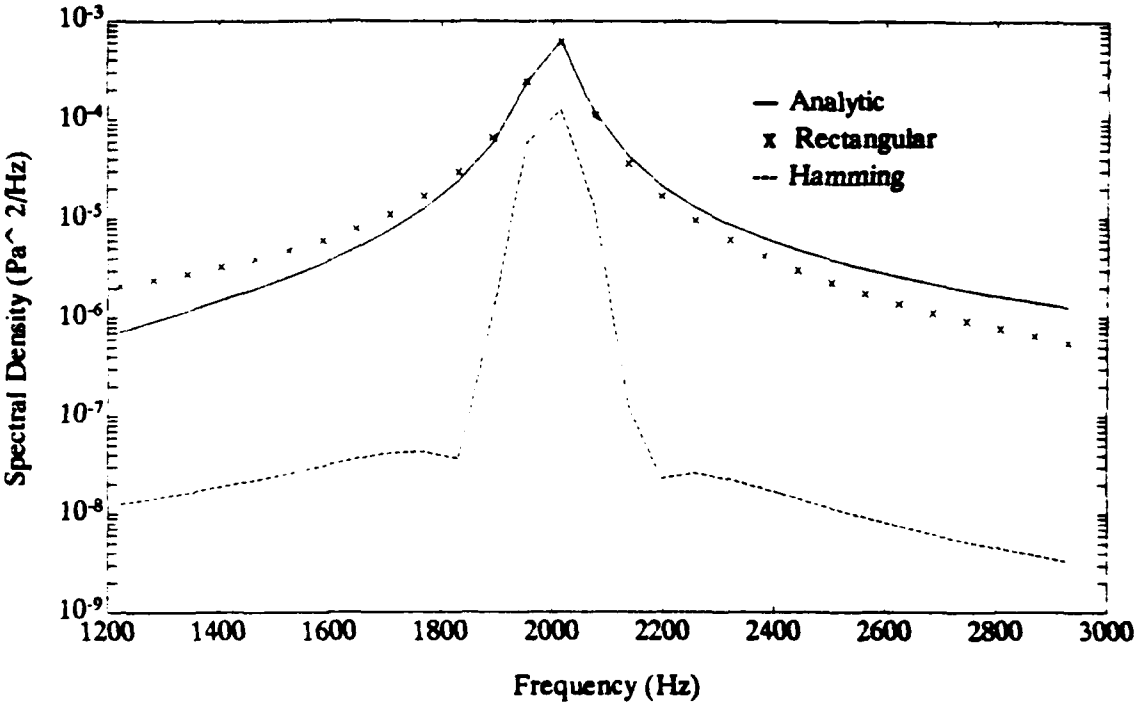

Figure 32. Comparison of the theoretical Fourier spectrum of the pressure signal (solid line) with the Rectangular windowed DFT spectrum (crosses) and the Hamming windowed DFT spectrum (dashed).

large drop sizes. The individual bubble spectra were then averaged and smoothed to obtain representative spectra for various drop size ranges. A summary of the drop diameters, size ranges, and number of bubble samples obtained is presented in Table 3. The drops of each diameter listed in Table 3 are taken to be characteristic of the corresponding range of drop sizes. Over 90 samples were obtained for all but the smallest drop size (the low bubble production rate, and deflection by drafts in the ventilation shaft, made collection of the 2.5 mm drop bubble signals difficult).

Since the impact spectra are much smaller in magnitude than the bubble spectra for each drop size, only 30 impact samples were collected to obtain average impact spectra for three drop diameters (2.5 mm, 3.4 mm, and 4.2 mm). The impact spectra for the remaining drop sizes were obtained by interpolating the measured spectra (the method used will be described later).

TABLE 3. NUMBER OF BUBBLE SAMPLES FOR EACH DROP SIZE

Drop Diameter (mm)	Drop Size Range (mm)	Number of Samples
2.5	2.2 - 2.8	46
3.0	2.8 - 3.2	99
3.4	3.2 - 3.6	98
3.8	3.6 - 4.0	100
4.2	4.0 - 4.4	100
4.6	4.4 - 4.8	99

B. EXPERIMENTAL PROCEDURES

1. Setup for Bubble Sound Measurements

The equipment setup used to measure the Type II bubble signal is shown in Figure 33. All the drops were released from a height of about 26 m using the drop tower and redwood tank arrangement described in the previous chapter. For these

experiments the tank was filled with saline water. Initially, artificial sea salt was added to the tank to simulate ocean water. Later, filtered seawater was obtained from the Monterey Bay Aquarium and added to the water already in the tank.

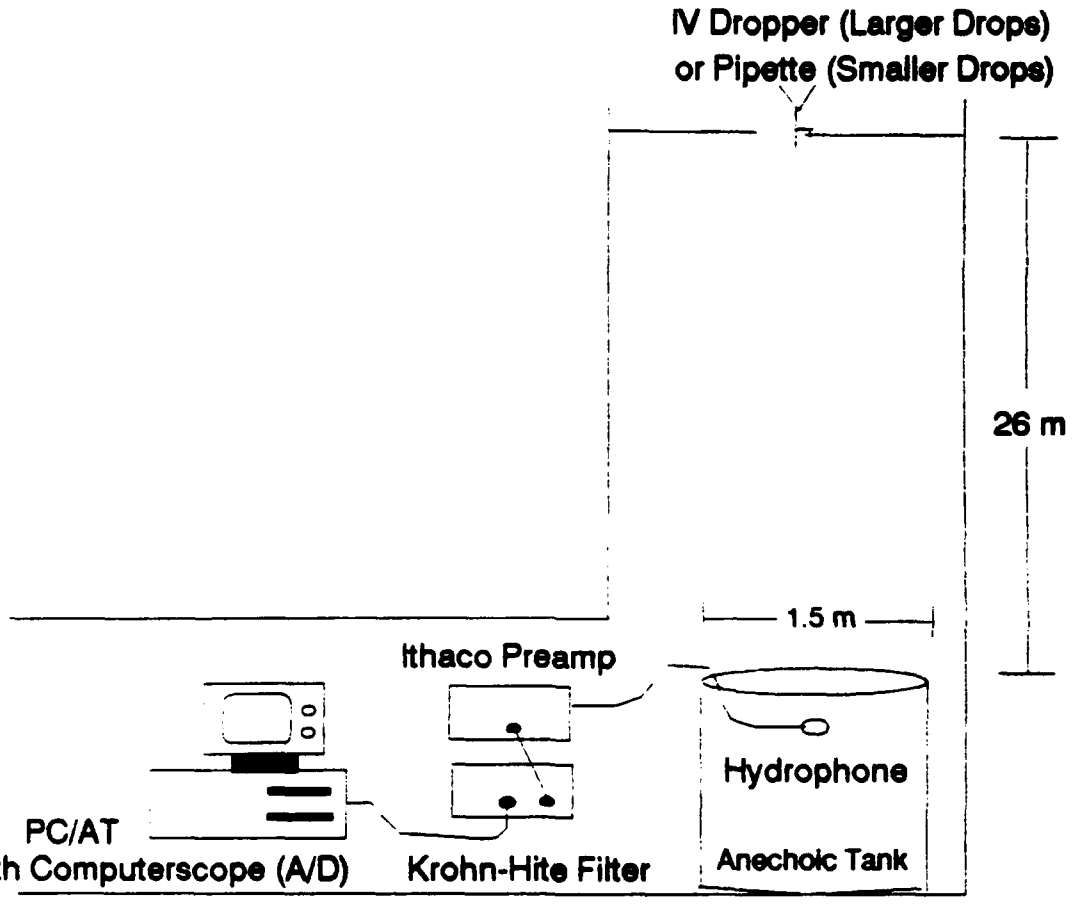

Figure 33. Equipment setup for bubble signal measurements.

For the drops in the 3.4 mm to 4.6 mm size range, calibrated pipette tips attached to an I-V bottle were used to generate the drops, with an accuracy of ± 5% by volume. For the other two drop sizes (2.5 mm and 3.0 mm), the drops were too small

to fall on their own. At first, the smaller drop sizes were generated by attaching a pipette tip to a loudspeaker driven by a function generator operating in "burst" mode. When the function generator triggered, the drop would be forced off the pipette by the vibration of the loudspeaker. The accuracy of this method was determined to be ± 20%, which was unsuitable when compared to the accuracy obtained for the larger drop sizes. The bubble signal measurements for the smallest two drop sizes were therefore repeated using an Eppendorf digital pipette, with an accuracy of ± 1% by volume. The disadvantage of using the pipette is that the drops had to be generated manually, requiring two people for data collection.

A single hydrophone was used to measure the underwater bubble noise. The hydrophone contains two coaxial 1/8 inch cylindrical barium titanate elements , and has a nominal sensitivity of -91.5 dB re V/Pa. The response of the hydrophone is flat (± 3 dB) over a frequency range of 5 to 300 kHz (Snyder, 1990). The hydrophone was located at a depth z of 9 cm for the 4.2 mm and 4.6 mm drops, and at a depth z of 6.0 to 6.5 cm for the smaller drops. The distance h on the surface from the point above the hydrophone to the point of drop impact was measured with a ruler to an estimated accuracy of ± 0.5 cm. A metal grid was placed over the surface to help determine where the drops landed; the grid squares were 5 cm by 5 cm.

An Ithaco preamplifier was used to amplify and filter the bubble signals. A gain of 2000 was used for the larger drop sizes and 5000 for the smaller drop sizes. The Ithaco was set up as a band pass filter with a pass band of 1 to 30 kHz. The filter settings were necessary because of electrical interference in the building at frequencies outside the pass band range. The output of the Ithaco was then passed through a single Krohn-Hite band pass filter with the same filter settings to further attenuate interfering noise. The resonance frequencies of the bubbles were in the pass band range, and the filter settings did not interfere with the bubble signal measurements.

The data was collected using the Computerscope digital analyzer, now mounted in a PC/AT computer. The sampling rate for the bubble signals was 250 kHz. The length of the bubble records extracted for processing and analysis was 16.0 ms (or 4000 data points for each bubble). A 16 ms record length was necessary to recover most of the energy (over 95%) of each bubble signal measured.

Measurements were also made of the drop temperature, surface temperature, salinity, and surface tension. The temperature measurements were made with mercury thermometers, with an accuracy of ± 0.5° C. The salinity was measured using a salinometer accurate to 0.05 ppt. Surface tension was measured with a capillary tube, which was accurate to ± 5 dyne/cm.

As mentioned in the introduction, Jacobus (1991) discovered that the energy radiated by the Type II bubbles seemed to depend on the salinity and on the surface-drop temperature difference. A summary of the present temperature measurements is given in Table 4. While the tank temperature remained fairly constant, the fluid temperature of the drops was difficult to control, since the data collection process could take several hours. Subsequently, the drop - surface temperature difference varied between 2 C° and 5.5 C°. This could result in a ± 0.8 dB variation in spectral energy, based on Jacobus's data for fresh water.

TABLE 4. SUMMARY OF DROP AND SURFACE TEMPERATURES

Drop Diameter (mm)	Drop Temperature (°C)	Surface Temperature (°C)	Temperature Difference (C°)
2.5	28	23	5
3.0	21	23	2
3.4	24	21	3
3.8	24	21	3
4.2	26	23	3
4.6	17	22.5	5.5

A summary of the salinity and surface tension measurements is shown in Table 5. The salinity values ranged from about 32.3 ppt to 37.3 ppt. The work by Jacobus suggests that this could cause a ± 3% (or ± 0.1 dB) variation in the energy levels. The tank salinity increased after the filtered seawater was added, apparently due to salt which had collected on the walls of the tank where the level was lower. Evaporation of some of the tank water may also have contributed to increasing salinity levels. In general, the surface tension in the tank increased with time due to repeated filtering of the tank water and the addition of pure filtered seawater after collection of the 4.2 mm raindrop data. Also, the water in the tank is discolored by the leaching of tannic acid from the redwood. Overall, the surface tension of the tank water was 10 to 20 dynes/cm lower than the surface tension of pure water at 18° C (73 dynes/cm). The effect this had on the bubble sound or the generation of bubbles is unknown.

2. Setup for Impact Sound Measurements

While the setup used to obtain the impact spectra was similar to the setup for the bubble measurements, there were some important differences. First, the impact signals were not band pass filtered. Filtering was minimized to prevent altering the impact signal. The Ithaco preamplifier was used to amplify the impact signals using a gain of 500, and had a high pass filter setting of 0.03 Hz to remove dc bias

TABLE 5. SUMMARY OF SURFACE TENSION AND SALINITY

Drop Diameter (mm)	Salinity (ppt)	Surface Tension (dyne/cm)
2.5	37.3	62
3.0	37.2	62
3.4	34.9	57
3.8	34.9	57
4.2	34.1	57
4.6	32.3	52

from the input signal to Computerscope. The Krohn-Hite band pass filter was not used at all. The hydrophone was placed at a depth of 10 cm for the impact measurements.

The impact signals were collected using Computerscope at the maximum sampling rate of 1 MHz. The largest possible sampling rate was used to prevent undersampling the impulse component of the impact sound. The noise from interference was much more pronounced than for the bubble measurements, and the impact signals were much shorter in duration. Therefore, shorter length records were extracted for the impact signals than for the bubble signals. The extracted record lengths were 500 μsec for the 2.5 mm impacts, 1 msec for the 3.4 mm impacts, and 2 msec for the 4.2 mm impacts.

C. DATA ANALYSIS

1. Analysis of the Bubble Signals

a. Conversion of Hydrophone Voltage to On-axis Pressure

The hydrophone voltage levels recorded by Computerscope were corrected to the on axis pressures at 1 m. To accomplish this, the recorded voltages were first corrected for the amplifier gain and the hydrophone sensitivity using:

$$p_{hyd} = \frac{V}{G \cdot M} \tag{11}$$

where p_{hyd} is the pressure at the hydrophone (Pa), V is the recorded voltage, G is the amplifier gain, and M is the hydrophone sensitivity (V/Pa). The hydrophone response was assumed to be omnidirectional.

Second, a correction must be applied to account for divergence ($1/r$ pressure variation), and a dipole radiation pattern ($\cos\theta$ pressure variation). The pertinent geometry is shown in Figure 34. The dipole radiation pattern for bubble oscillations has been confirmed by Kurgan (1989) for Type I (small raindrop) bubbles. The necessary correction factor is given by:

$$p_{1m\ on\ axis} = p_{hyd} \cdot \frac{h^2 + z^2}{100 \cdot z} \tag{12}$$

where p_{hyd} is the uncorrected pressure, z is the hydrophone depth (in cm), h is the distance from the point of impact to the point above the hydrophone (in cm), and $p_{1m\ on\ axis}$ is the on-axis pressure at one meter.

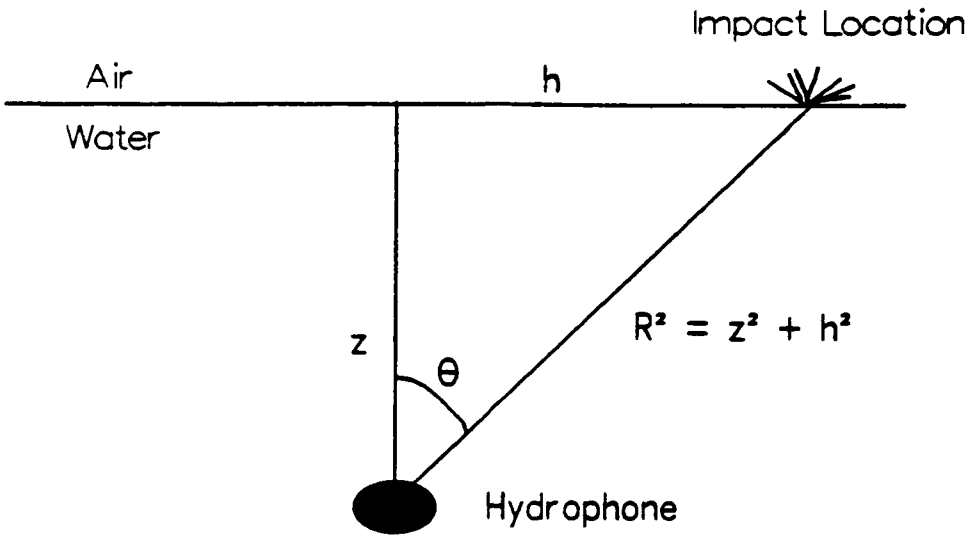

Figure 34. Geometry for range and angle correction.

For some of the bubble signal measurements, the hydrophone was in the near field of the dipole. To correct for this, a third correction factor had to be applied, and is given by (Medwin and Beaky, 1989):

$$p_{farfield} = p_{1m\ on\ axis} \cdot \sqrt{\frac{1}{1+\frac{1}{k^2 r^2}}} \qquad (13)$$

where $p_{farfield}$ is the corrected far field pressure, r is the range (m), and k is the wave number (m^{-1}), which can be computed from the resonance frequency of the bubble ($k = 2\pi f/c$, where c is the sound speed in m/s and f the bubble frequency in Hz).

b. Calculation of the Acoustic Energy Spectra

A 4096 point Fast Fourier Transform of each bubble signal time series was computed using MATLAB to obtain the bubble frequency spectra. The FFT algorithm employed by MATLAB is given by:

$$X(k+1) = \sum_{n=0}^{N-1} x(n+1)\, e^{\frac{-i2\pi nk}{N}} \tag{14}$$

where $x(n)$ represents the time series values, $X(k)$ represents the frequency series values, and N is the number of points in the series. For this case, the $x(n)$ are pressure values in Pa; the units of the spectral values $X(k)$ are Pa per bin.

To compute the energy density spectrum in $Pa^2 \cdot s/Hz$ from the FFT values, the following equation is used:

$$E(f) = \frac{2 \cdot \Delta t \cdot |X(k)|^2}{N \cdot df} \tag{15}$$

where $E(f)$ is the energy spectral level (in units of $Pa^2 \cdot s/Hz$) at the frequency f, X is the Discrete Fourier Transform value with index k, and N is the number of points. The frequency f is given by $k \cdot df$, as k varies from 0 to $N/2$. The frequency

resolution (or bin width) is given by $df = 1/N\Delta t$, where Δt is the sampling interval. For the 250 kHz sampling rate used to collect the bubble data, the sampling interval was 4 μsec, giving a frequency resolution of 61 Hz for a 4096 point FFT. To resolve any confusion between Equation 15 and other equations for the power or energy spectrum of a signal, a derivation of Equation 15 is provided in Appendix A.

c. Averaging of the Bubble Spectra

The individual bubble sound spectra will contain peaks at the resonance frequencies of the bubbles. More than one peak may be present if the event results in secondary bubbles as well as a dominant bubble. Both the magnitude and the frequency of the peak(s) can vary from one spectrum to the next. It is therefore necessary to statistically average the bubble spectra in some fashion to obtain a representative spectrum for a given drop size.

To accomplish this, two different approaches have been employed here. The first approach, following the method of Jacobus (1991), is to ensemble average the individual bubble spectra for each raindrop size. After the spectra are ensemble averaged, a 1 kHz wide moving filter is applied to smooth the ensemble spectrum.

An alternative approach for obtaining a smooth spectrum was to fit a smooth curve to the probability distribution of dominant bubble frequencies for each

drop size. The bubble frequency distribution curve $n(f)$, where $n(f)$ represents the fraction of bubbles with resonance frequencies within a given frequency interval centered on the frequency f, is then multiplied by the total spectral energy (in units of $Pa^2 \cdot s$) to obtain a smooth energy density spectrum for each drop size. The total spectral energy for each drop size was obtained by integrating the average spectra obtained previously.

The smoothing method just described is performed using only the dominant bubble frequencies, since the dominant bubbles seem to account for most of the raindrop bubble energy (Jacobus, 1991). To show this, the average spectra were computed using the dominant bubble contribution only and compared to the spectra containing both dominant and secondary bubble energy. To obtain only the dominant bubble contribution to the average spectra, a simulated bandpass filter centered on the dominant bubble frequency was applied to the individual bubble spectra prior to averaging. The filter frequency width was six times the theoretical 3 dB bandwidth for an oscillating bubble at a given frequency. This bandwidth was selected because it allowed for recovery of approximately 90% of the dominant bubble energy.

d. Bubble Total Energy Calculation

To investigate the variation of dominant bubble energy with bubble frequency, the dominant bubble energies were calculated using the following equation (Kurgan, 1989):

$$E = \frac{2\pi r^2}{3\rho c} \cdot \sum_{t=0}^{t=T} p_{ax}(t)^2 \Delta t \tag{16}$$

where E is the total bubble energy (in Joules), r is the range, ρc is the acoustic impedance, and the summation is over the square of the axial pressure values for the bubble signal time series. This equation accounts for the dipole nature of the bubble sound, and holds for $k \cdot r > 3$, where k is the wavenumber. A derivation of Equation 16 is given in Appendix B. The squared axial pressure summation in the time domain is related to the axial energy density spectrum defined in Equation 15 by:

$$\sum_{f=0}^{f=f_{max}} E(f)\,df = \sum_{t=0}^{t=T} p_{ax}(t)^2 \,\Delta t \tag{17}$$

Equation 16 can therefore be expressed in terms of the axial energy density spectrum as:

$$E = \frac{2\pi r^2}{3\rho c} \cdot \sum_{f=0}^{f=f_{max}} E(f)\,df \tag{18}$$

where the range r is 1 m. The integration is performed over a frequency interval equal to six times the 3 dB bandwidth of the bubble signals. This bandwidth was sufficient for recovering 90% of the dominant bubble energy.

2. Analysis of the Impact Signals

Similar analysis techniques were used to obtain the impact spectra, with some important differences. For converting the measured voltages to pressures, no near field correction factor was applied, since the hydrophone was placed farther from the surface than for the bubble measurements, and the impact noise is broadband. Also, the record lengths used for the spectral analysis were shorter (from 500 μsec to 2 msec). The contribution to the impact spectra from the plateau component of the impact noise, which results in a peak in the spectrum at low frequencies (less than about 1000 Hz), was rejected. As stated earlier, the plateau noise does not appear to contribute to the far field noise signature of the impact.

D. RESULTS

1. Bubble Formation Percentages

A summary of the percentage of large raindrops observed to produce bubbles in salt water is given in Table 6. The percentages are in general agreement with the percentages obtained by Snyder (1990) for fresh water. In general, the

percentage of large raindrops that produce bubbles tends to decrease with decreasing drop size.

TABLE 6. BUBBLE PRODUCTION PERCENTAGE

Drop Diameter (mm)	Bubble Percentage	
	Fresh	Salt
2.5	20	25
3.0	37	37
3.4	50	50
3.8	63	50
4.2	62	50
4.6	55	62

Of the fraction of raindrops which produce bubbles, a still smaller fraction produce both dominant and secondary bubbles. The percentage of secondary bubble formation for the drops observed to produce bubbles is given in Table 7. Overall, the percentage of secondary bubble formation is between 10 and 20%. The relatively high percentage observed for the 4.6 mm drops could be because they are the most energetic. As noted by Jacobus (1991), the secondary bubbles were generally smaller in magnitude and higher in frequency than the dominant bubbles.

TABLE 7. PERCENTAGE OF BUBBLE PRODUCING DROPS THAT INCLUDE SECONDARY BUBBLES IN SALT WATER

Drop Diameter (mm)	Percentage
2.5	8
3.0	9
3.4	19
3.8	16
4.2	12
4.6	35

2. Average Bubble Spectra

The spectra obtained from ensemble averaging and smoothing the individual bubble spectra are shown in Figures 35 through 40. Even after smoothing, the spectra have multiple peaks. Jacobus ascribed the secondary peaks in the spectra to the contribution of secondary bubbles and to a phenomenon he referred to as "wobbles". The wobbles were gated sinusoidal signals that appeared before, during, or after the bubble signal. No wobbles were observed in the bubble signals collected for this work; in fact, the wobbles may have been a tank scattering artifact which was present only prior to installation of the redwood wedges on the walls of the tank. Moreover, the likelihood that the secondary bubbles would produce peaks in the spectra of the same order of magnitude as the dominant peak is inconsistent with the

relatively small percentage of secondary bubble formation, and the lower energy of the secondary bubbles as compared to the dominant bubbles.

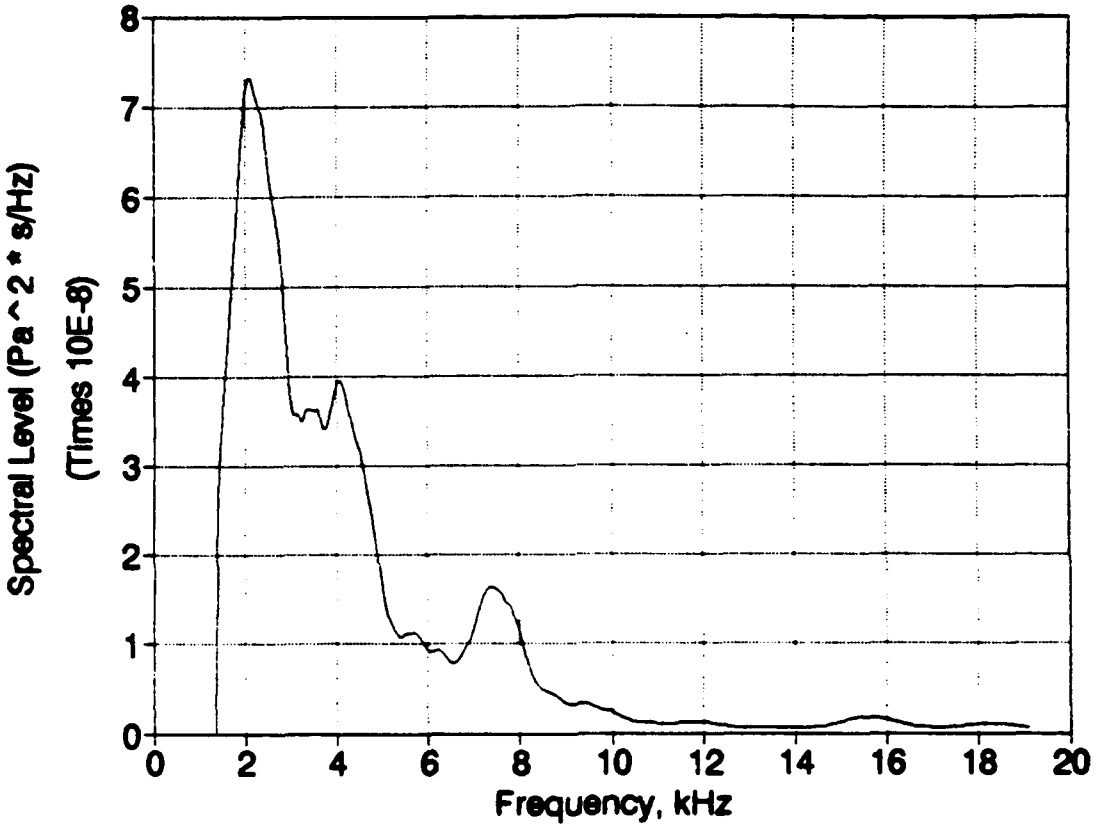

Figure 35. Average bubble spectrum, 4.6 mm diameter raindrops.

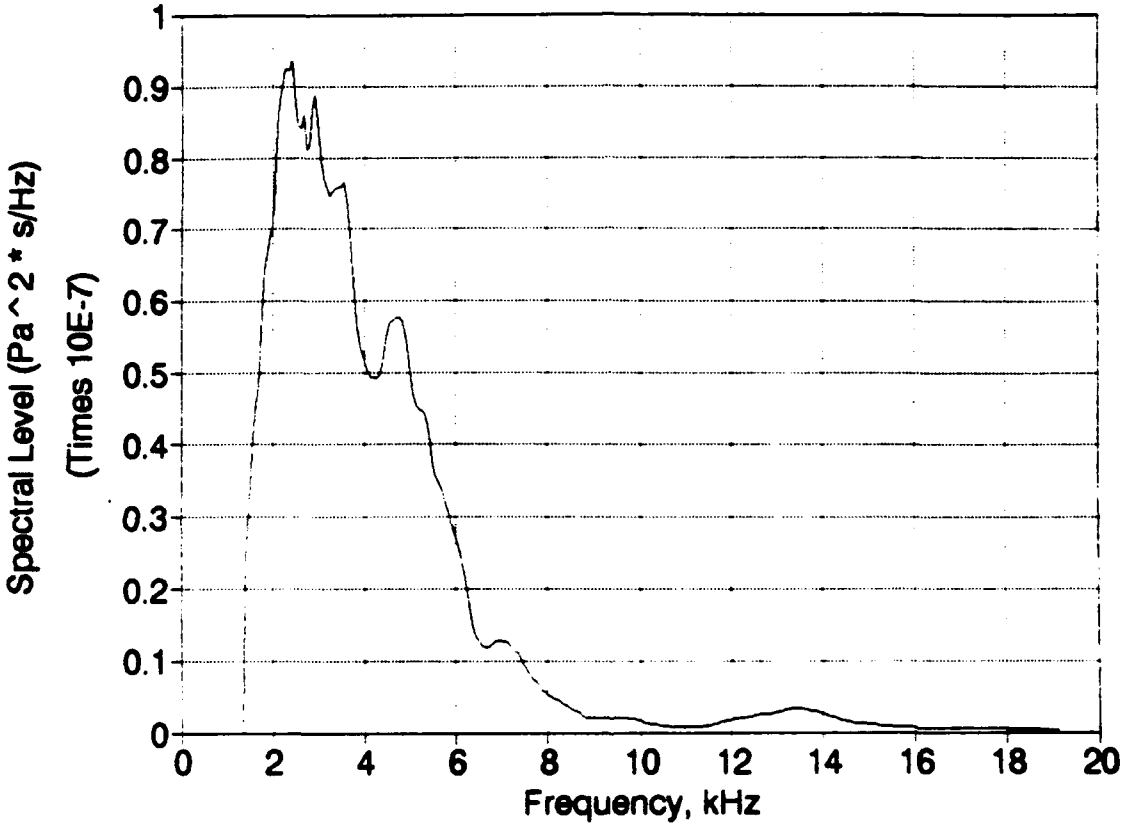

Figure 36. Average bubble spectrum, 4.2 mm diameter raindrops.

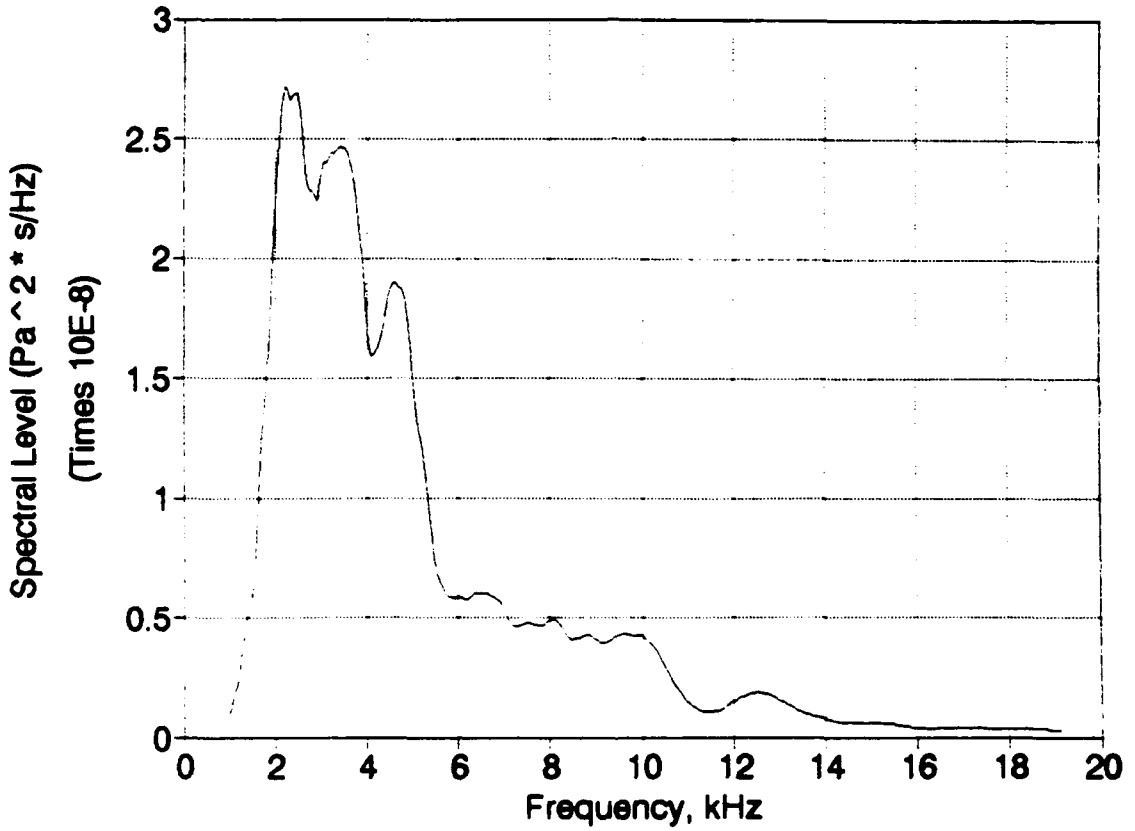

Figure 37. Average bubble spectrum, 3.8 mm diameter raindrops.

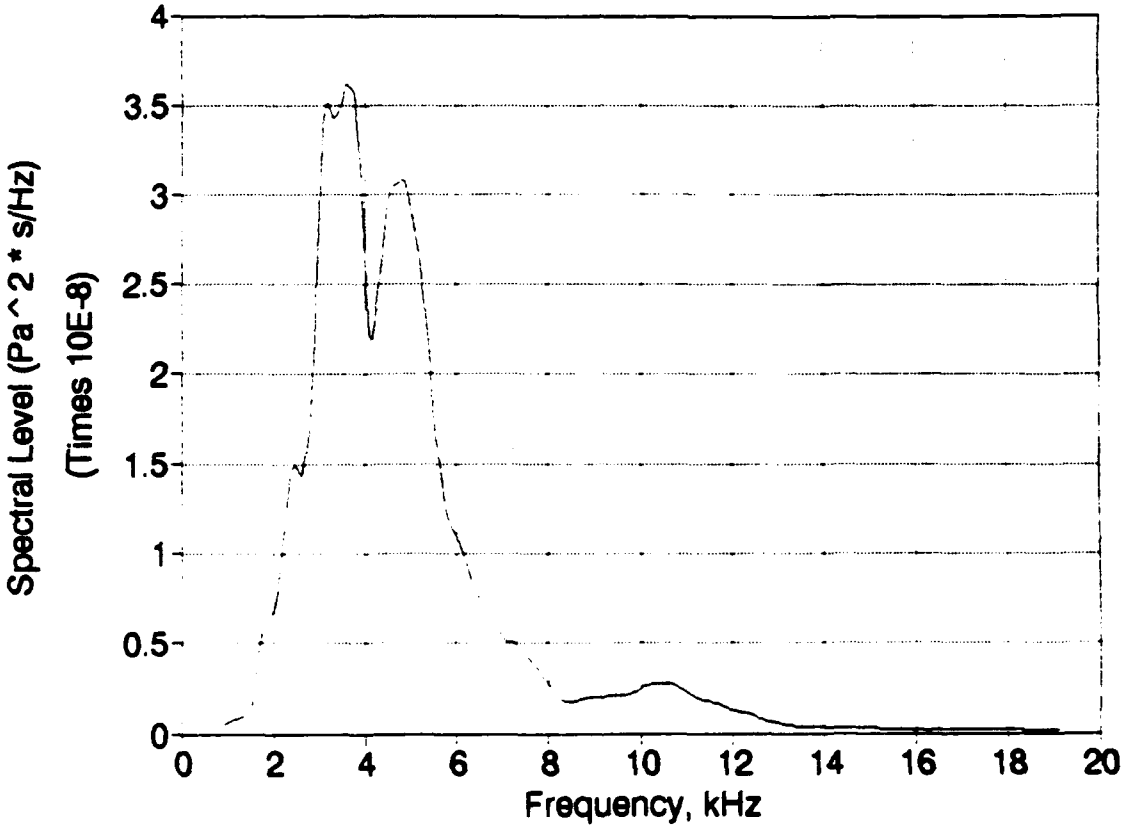

Figure 38. Average bubble spectrum, 3.4 mm diameter raindrops.

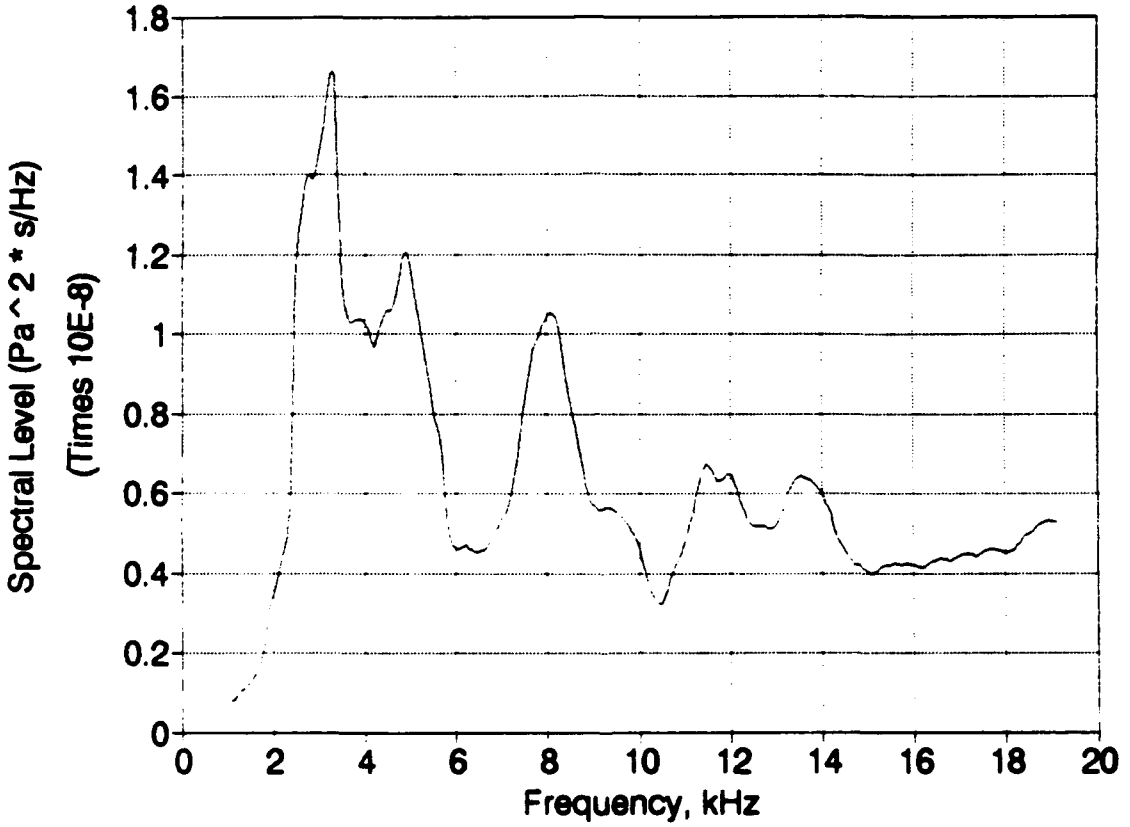

Figure 39. Average bubble spectrum, 3.0 mm diameter raindrops.

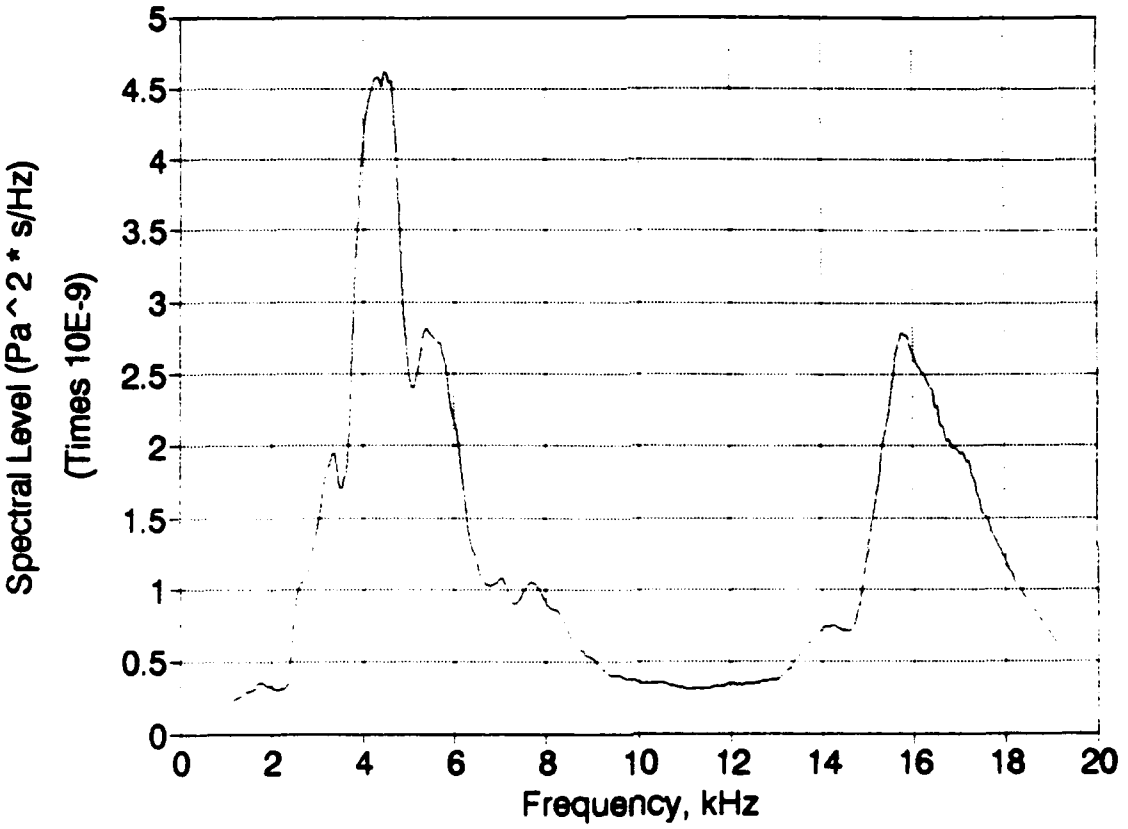

Figure 40. Average bubble spectrum, 2.5 mm diameter raindrops.

To investigate the notion that the spectral peaks are due mainly to the dominant bubble signals, average spectra were obtained which included only the energy of the dominant bubble. The resulting spectra tend to have the same overall shape as before, although the spectral levels are somewhat smaller (about 10 to 20%) over most of the frequency range. An example is shown in Figure 41 for the 4.6 mm diameter drops. Similar results were obtained for the other drop sizes.

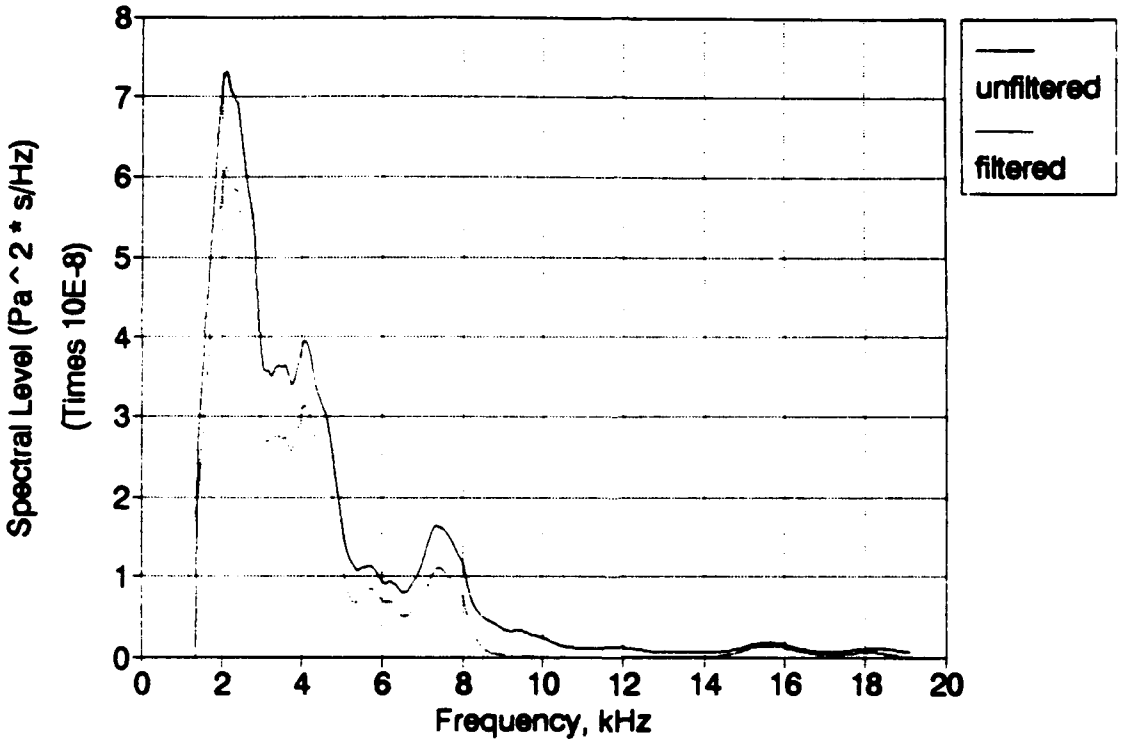

Figure 41. Comparison of the 4.6 mm raindrop bubble spectrum (solid) with the spectrum of the dominant bubble energy alone (dashed).

The broad shape of the spectra can be mostly attributed to the dominant bubbles. However, highly energetic individual bubbles may be responsible for local peaks in the spectra, since the spectral peak for an individual bubble can be relatively narrow (the 3 dB bandwidth for a 2000 Hz bubble is on the order of 100 Hz). An ensemble average of as many as 100 bubble spectra may be insufficient for obtaining a smooth spectrum. All of the average bubble spectra have been plotted in Figure 42 to illustrate their relative shapes and magnitude.

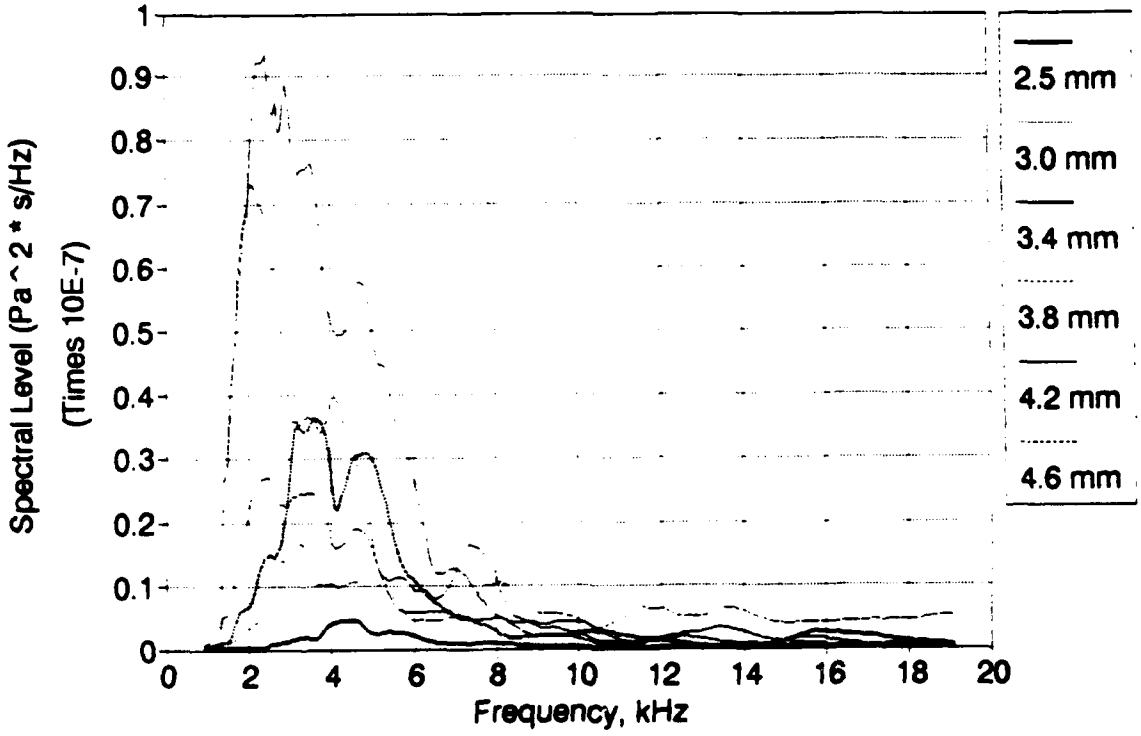

Figure 42. Bubble spectra for the six large raindrop diameters studied.

3. Bubble Frequency Distributions

The dominant bubble frequencies for each drop size were computed. The mean, the median, and the standard deviation of the dominant bubble frequencies are given in Table 8. As can be seen, the dominant bubbles tend to increase in frequency with decreasing drop size. Also, the variation in bubble frequencies becomes quite large for the smallest drop sizes (2.5 mm and 3.0 mm). Both of these observations agree with the trends observed in the average bubble spectra.

TABLE 8. DOMINANT BUBBLE STATISTICS

Drop Diameter (mm)	Mean Frequency (Hz)	Median Frequency (Hz)	Standard Deviation (Hz)
2.5	10,023	9125	5597
3.0	9874	8484	6442
3.4	4905	4242	2305
3.8	4514	3998	2139
4.2	3716	3235	2240
4.6	3327	2808	1999

Histograms showing the percentage of dominant bubbles vs. frequency are shown in Figures 43 through 48. The frequency bins in these figures are 244 Hz wide.

The smooth, fitted curves shown in the figures are gamma probability distributions, given by:

$$g(f) = \frac{1}{\beta^{\alpha}\Gamma(\alpha)} \cdot f^{(\alpha-1)} \cdot e^{-\frac{f}{\beta}}, \qquad f > 0 \tag{19}$$

where f is the frequency, α and β are parameters that define the shape of the distributions, and $\Gamma(\alpha)$ is the gamma function evaluated at α (eg., see Walpole and Meyers, 1989). The gamma distribution was selected to model the dominant bubble frequency distributions because the distributions appear to be skewed right (towards higher frequencies). The skewness could not have been modeled adequately using a normal probability distribution unless higher moments (skewness and kurtosis) had been introduced. Most of the fitted curves are in reasonable agreement with the actual distributions. The fits are poorest for the smallest drop sizes (2.5 and 3.0 mm diameter). For the 2.5 mm drops, this may be in part due to the smaller sample size (46 vice 98 to 100 for the other drop sizes). Since the average energy for the smaller drops is less than for the larger drops, the fit may not be as critical for these sizes.

The characteristics of the bubble frequency distributions as a function of drop size may explain some of the observed spectral characteristics. As drop size decreases, the dominant bubble frequency tends to increase (eg., the smaller drops tend to produce smaller, higher frequency bubbles). The standard deviation of dominant bubble frequencies also tends to increase with decreasing drop size. In fact,

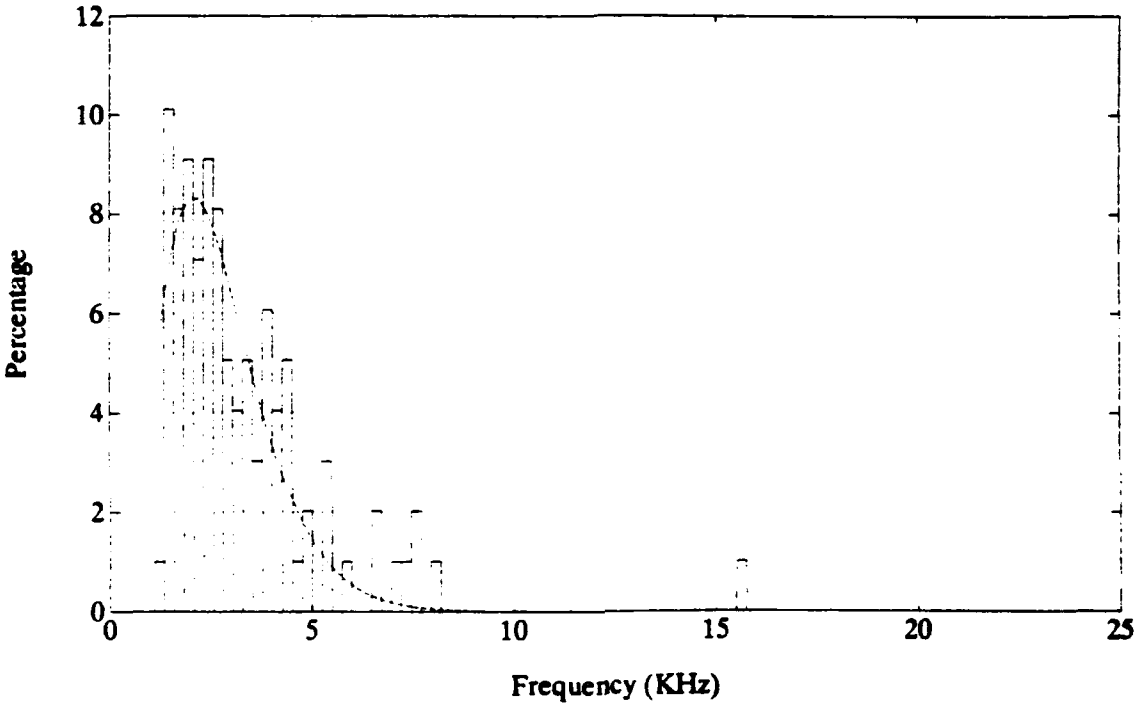

Figure 43. Dominant bubble frequency distribution, 4.6 mm diameter drops. The dashed line is the gamma distribution of Equation 19 with $\alpha = 4.31$, $\beta = 626$.

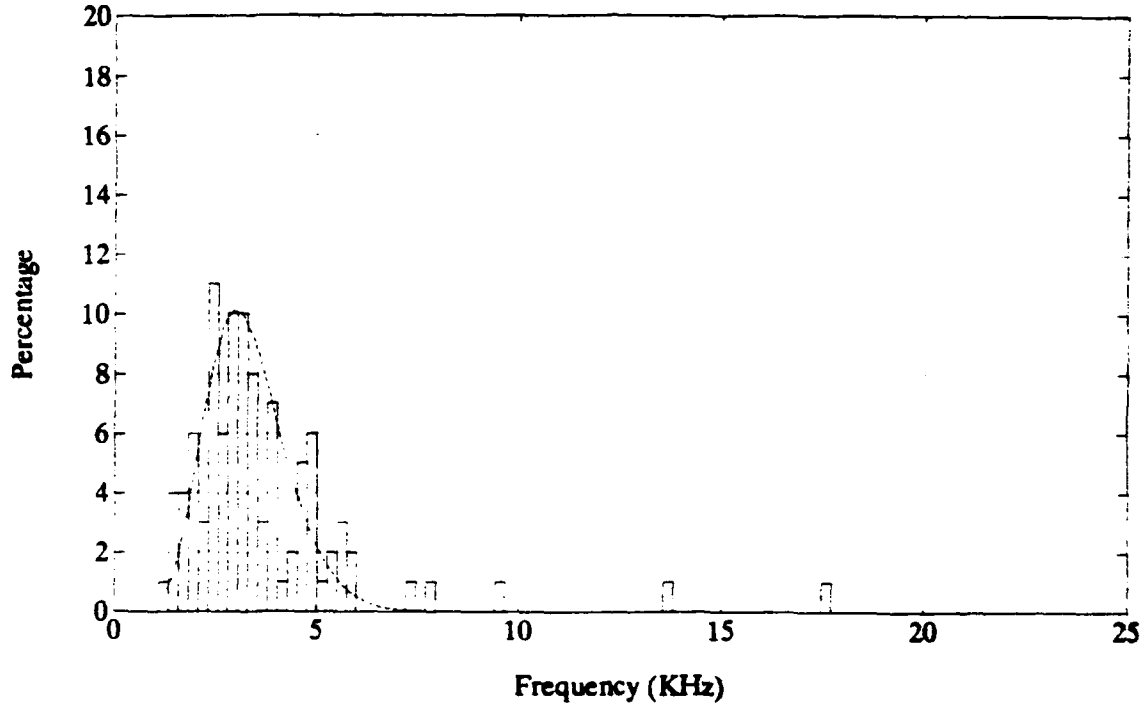

Figure 44. Dominant bubble frequency distribution, 4.2 mm diameter drops. The dashed line is the gamma distribution of Equation 19 with $\alpha = 10.9$, $\beta = 303$.

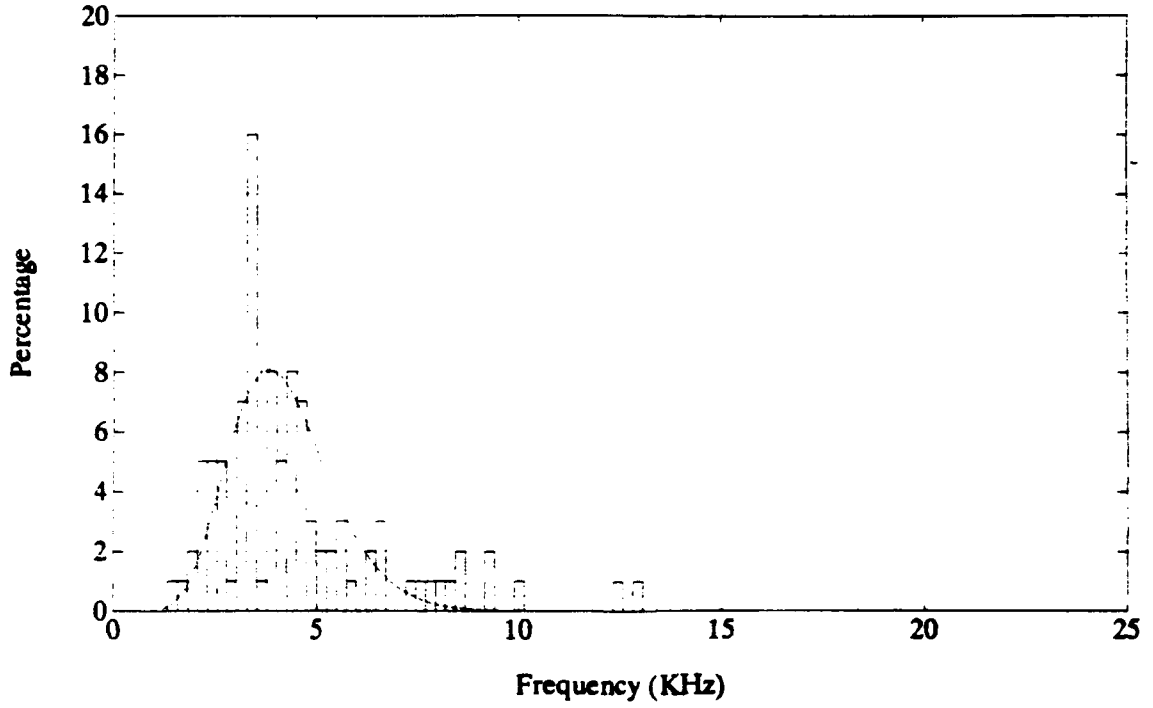

Figure 45. Dominant bubble frequency distribution, 3.8 mm diameter drops. The dashed line is the gamma distribution of Equation 19 with α = 11.3, β = 372.

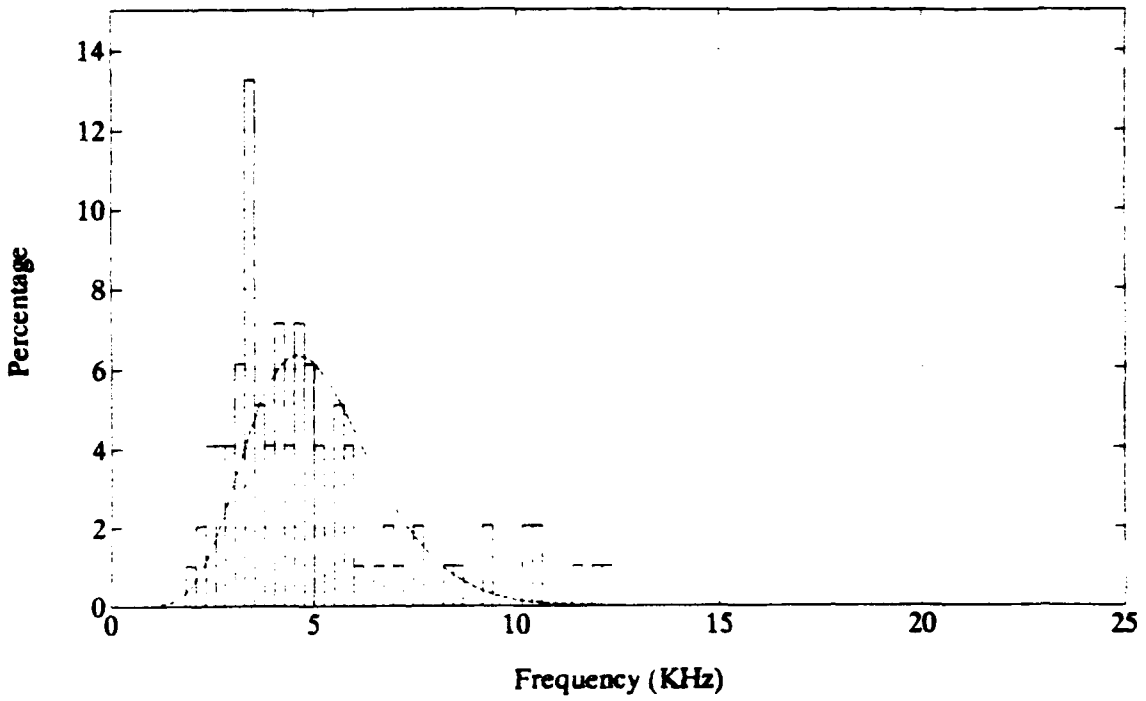

Figure 46. Dominant bubble frequency distribution, 3.4 mm diameter drops. The dashed line is the gamma distribution of Equation 19 with α = 10.2, β = 502.

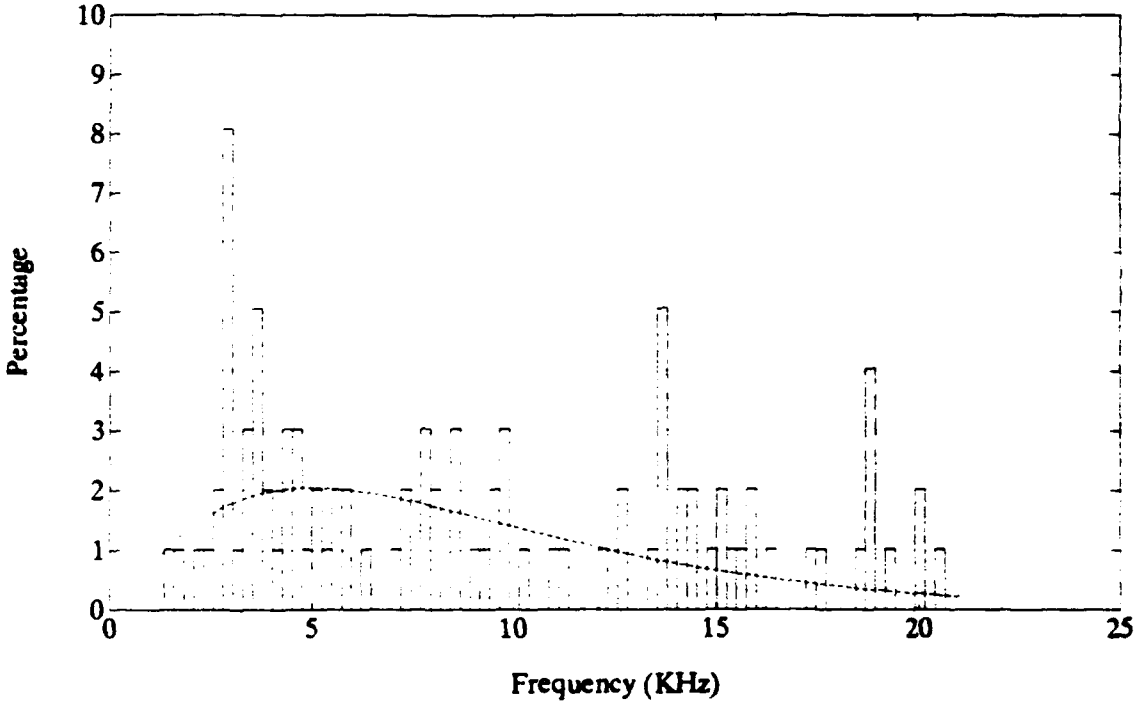

Figure 47. Dominant bubble frequency distribution, 3.0 mm diameter drops. The dashed line is the gamma distribution of Equation 19 with $\alpha = 2.25$, $\beta = 4000$.

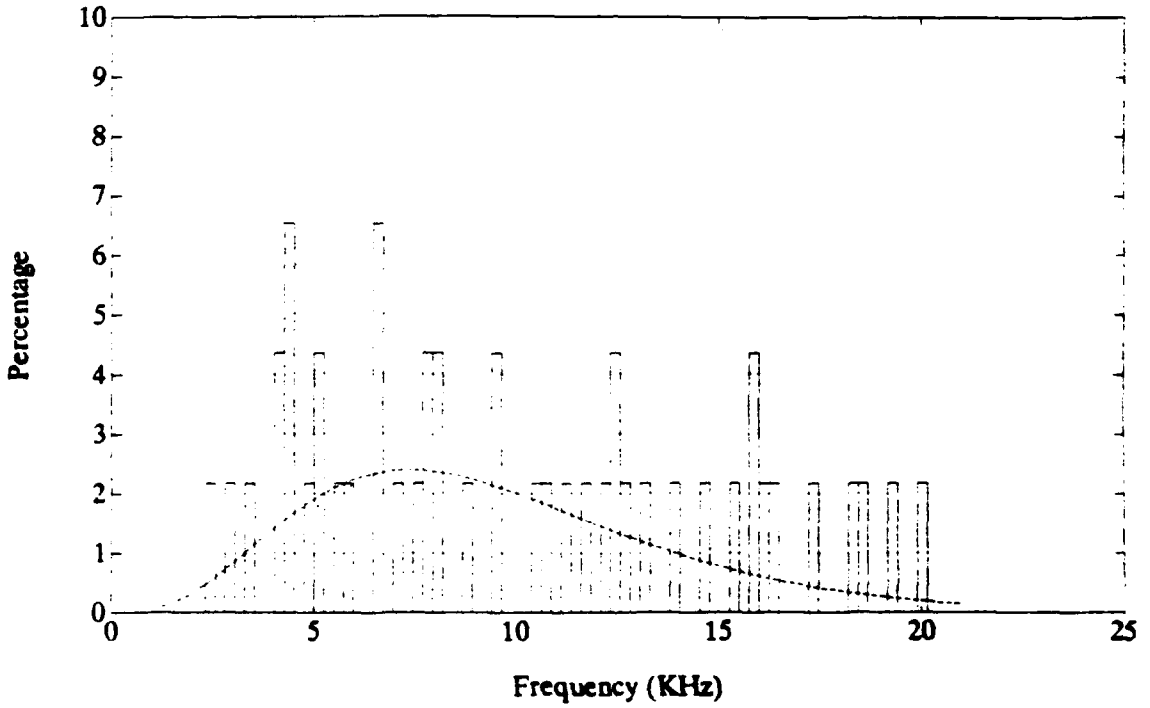

Figure 48. Dominant bubble frequency distribution, 2.5 mm diameter drops. The dashed line is the gamma distribution of Equation 19 with $\alpha = 5.98$, $\beta = 1840$.

the probability distributions for the smallest drop sizes (2.5 and 3.0 mm diameter) are rather uniform, which agrees with the observation that the spectra for the smallest drops are rather broad. In the next section, the fitted distribution curves will be used to obtain smoothed average spectra for the various drop size ranges. The smoothed spectra will then serve as the basis for calculating the predicted underwater acoustic spectra due to rainfall at sea for a given rainfall rate.

4. Fitted Bubble Spectra

The fitted distributions for the dominant bubble frequencies were used as the basis for smoothing the bubble energy spectra. The average bubble spectrum for each drop size was integrated, and the resulting value was multiplied by the fitted bubble frequency distribution to yield a smooth spectrum. The results are shown in Figures 49 through 54, where the smoothed spectrum is compared with the average spectrum for each drop size.

The smoothing technique used here does have some flaws. For instance, theoretically the energy radiated by individual bubbles depends on the bubble frequency. The damping constant for higher frequency bubbles is higher than for lower frequency bubbles, varying from 0.03 for 2 kHz bubbles to 0.06 for 20 kHz bubbles (Clay and Medwin, 1977). Thus, for the same initial amplitude, a high frequency bubble signal will decay more rapidly and radiate less energy than for a low

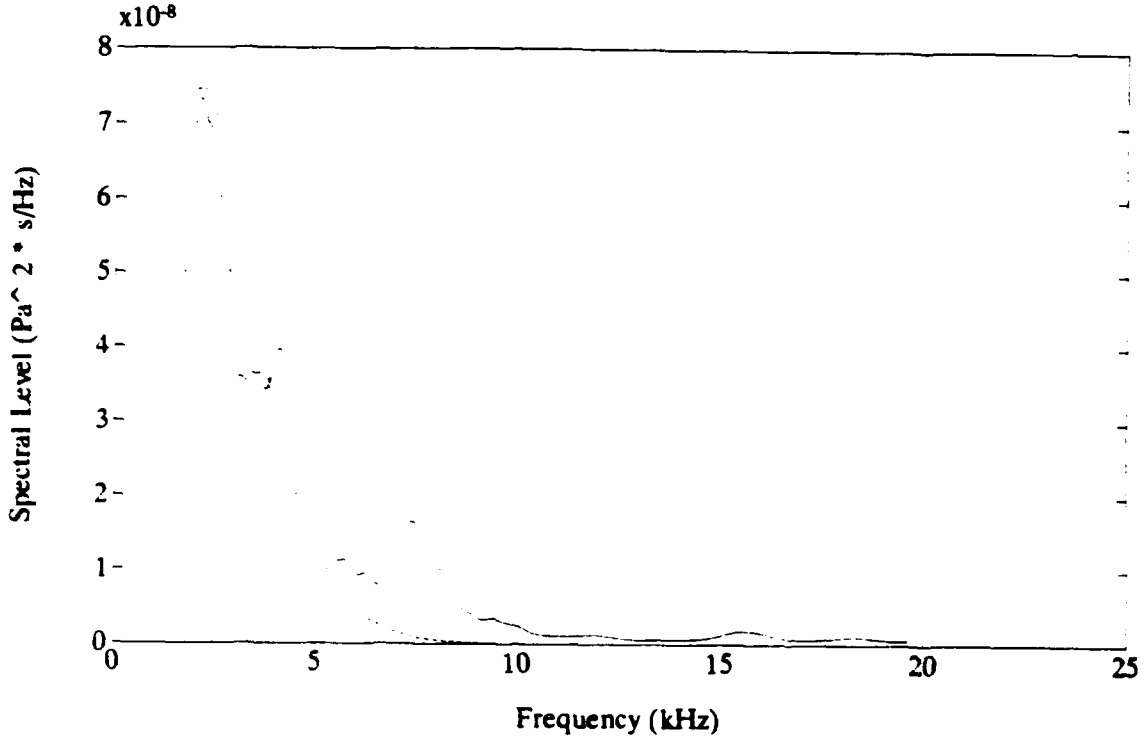

Figure 49. Average spectrum (solid) vs. smoothed spectrum (dashed), 4.6 mm drops. The integrated spectral energy is $2.13 \cdot 10^{-4}$ $Pa^2 \cdot s$.

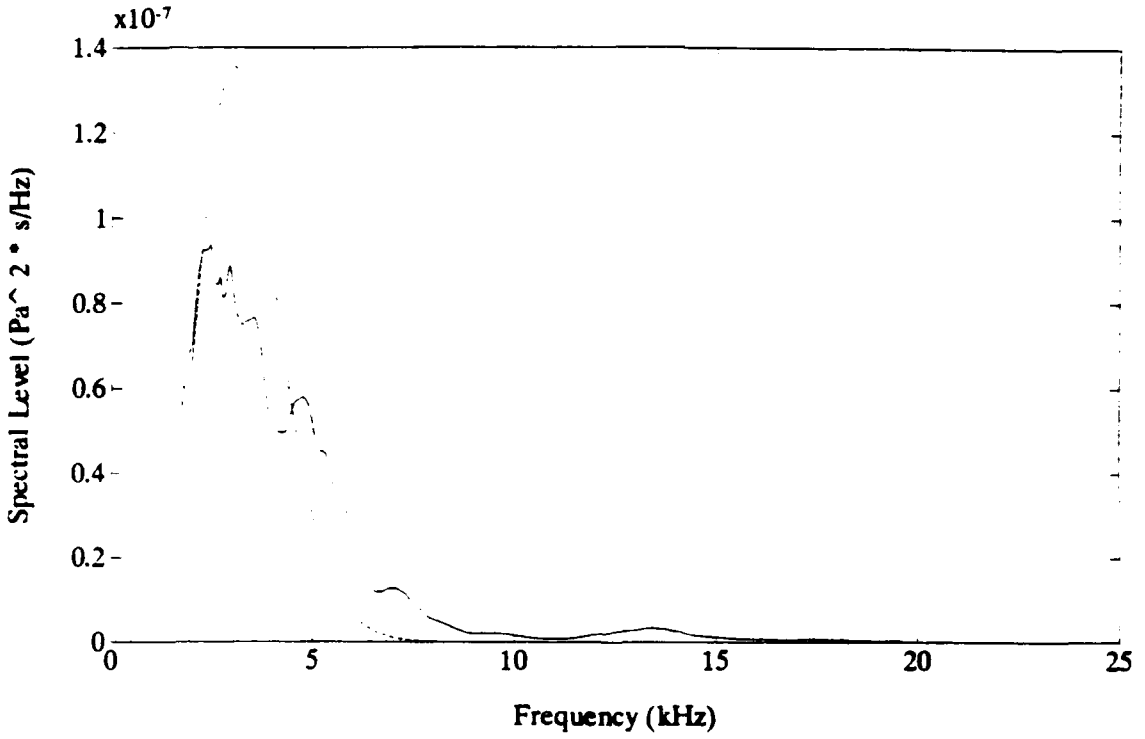

Figure 50. Average spectrum (solid) vs. smoothed spectrum (dashed), 4.2 mm drops. The integrated spectral energy is $3.22 \cdot 10^{-4}$ Pa^2-s.

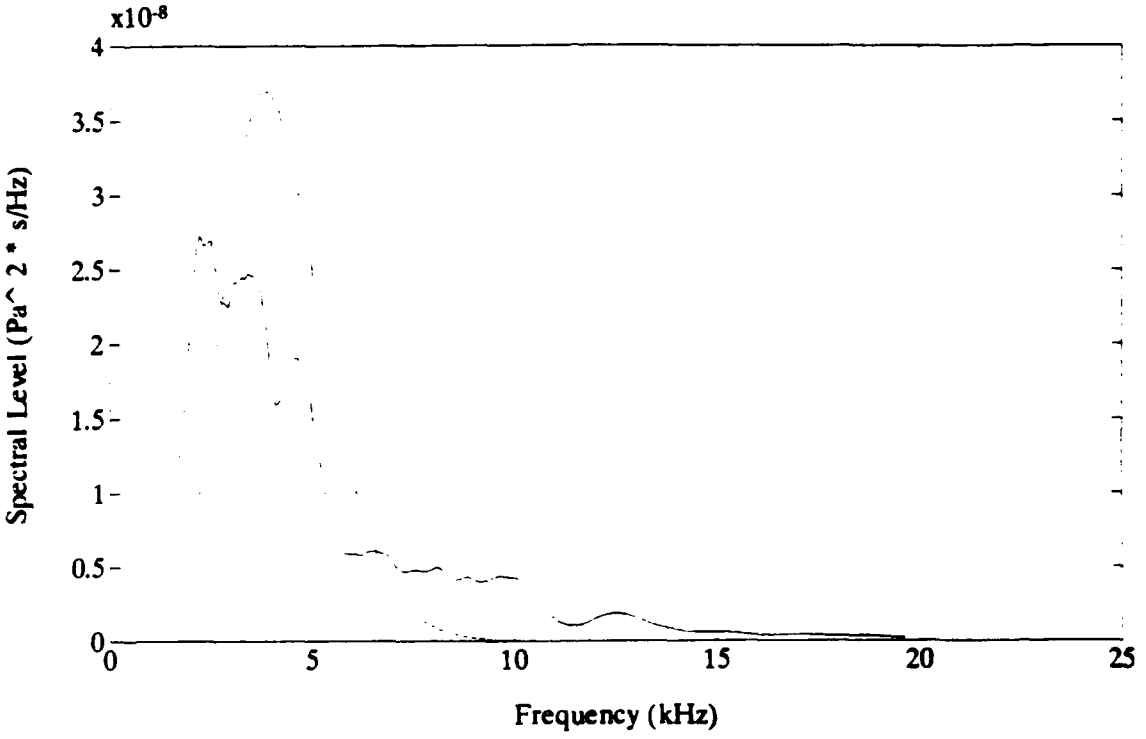

Figure 51. Average spectrum (solid) vs. smoothed spectrum (dashed), 3.8 mm drops. The integrated spectral energy is $1.11 \cdot 10^{-4}$ $Pa^2 \cdot s$.

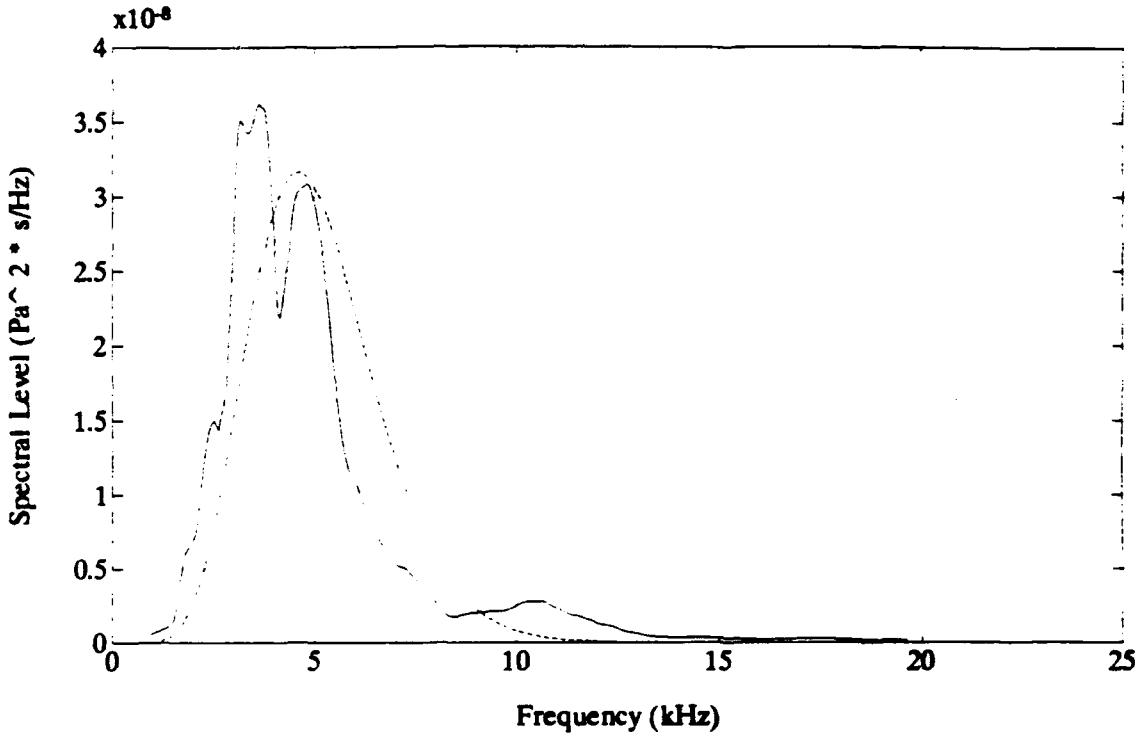

Figure 52. Average spectrum (solid) vs. smoothed spectrum (dashed), 3.4 mm drops. The integrated spectral energy is $1.22 \cdot 10^{-4}$ $Pa^2 \cdot s$.

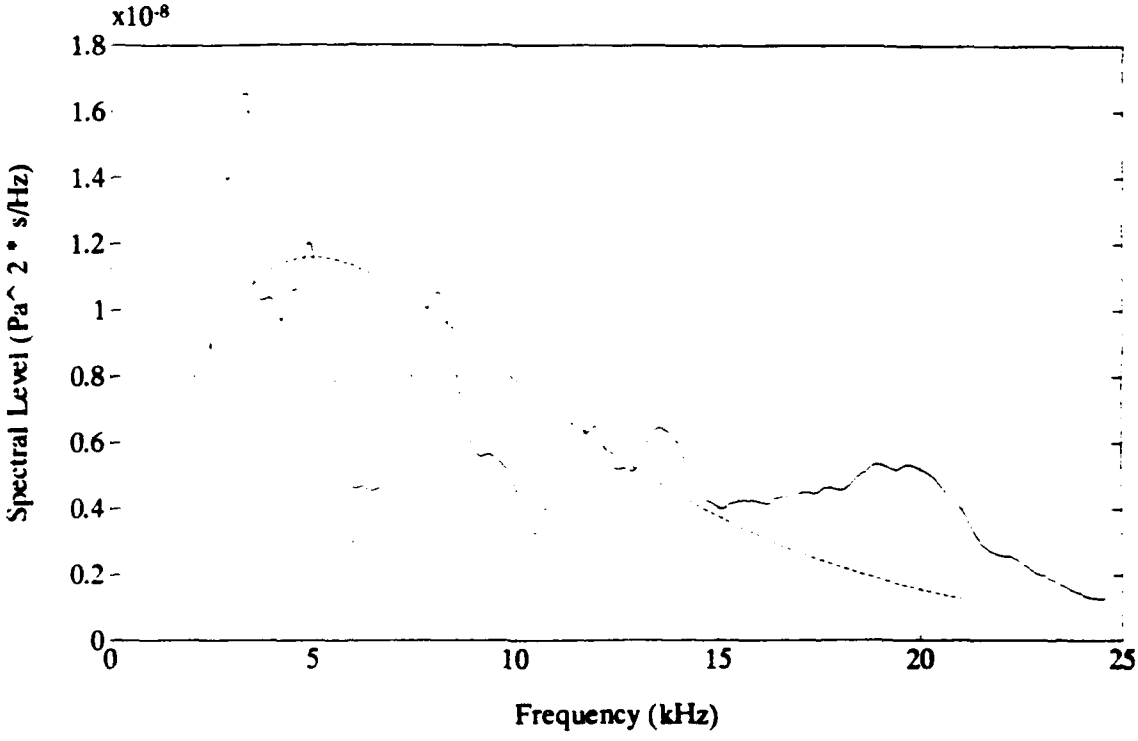

Figure 53. Average spectrum (solid) vs. smoothed spectrum (dashed), 3.0 mm drops. The integrated spectral energy is $1.14 \cdot 10^{-4}$ $Pa^2 \cdot s$.

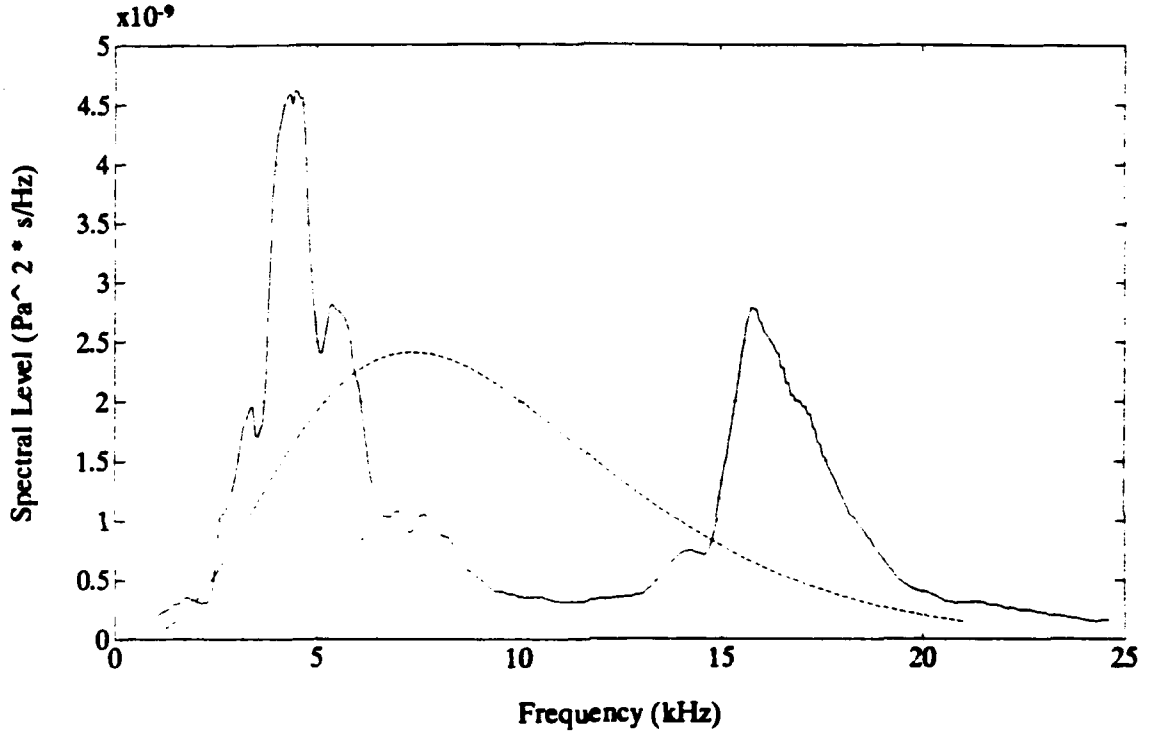

Figure 54. Average spectrum (solid) vs. smoothed spectrum (dashed), 2.5 mm drops. The integrated spectral energy is $2.29 \cdot 10^{-4}$ $Pa^2 \cdot s$.

frequency bubble signal. For instance, a theoretical 2 kHz bubble with the same initial amplitude as a 10 kHz bubble will radiate 8 times as much energy. To investigate this possibility, the dominant bubble energies for each drop size were calculated per Equation 16 and then averaged together in 2 kHz wide frequency intervals. Plots of the average dominant bubble energy vs. frequency are shown in the upper half of Figures 55 through 60 for each drop size. The number of dominant bubbles in each frequency interval is shown in the lower half of these figures. No energy vs. frequency trend can be readily discerned for most of the drop sizes, perhaps because of the relatively small number of drops in some frequency intervals. It may be possible that the higher frequency bubbles tend to have larger initial amplitudes than the lower frequency bubbles. For the 3.4 mm drops, however, the bubble energies do appear to decrease with increasing frequency.

Some of the average bubble energies in the range of 12 to 18 kHz appear to be unusually high for the 4.6 mm, 4.2 mm, and 2.5 mm diameter drops. Some of the bubbles in this frequency range may actually have been secondary raindrop bubbles generated by droplets expelled during the raindrop splash.

Another factor to consider is the variation of the bubble signal bandwidths with frequency. The theoretical bandwidth for a bubble oscillating at a frequency f_R is given by:

$$\Delta f = \delta_R \cdot f_R \tag{20}$$

where Δf is the 3 dB bandwidth and δ_R is the damping constant (Clay and Medwin, 1977). A 2000 Hz bubble, for instance, has a theoretical bandwidth of about 60 Hz in the frequency domain, while the bandwidth for a 20 kHz bubble is about 1200 Hz. Thus, not all the bubble energy for the higher frequency bubbles will be confined to a single frequency bin (for the fitted distributions, the bins were 244 Hz wide).

Despite these flaws, the smoothed spectra are in reasonable agreement with the average spectra, except for the 2.5 mm drops. However, as can be seen from the energy vs. frequency plot for this drop size (Figure 60), it appears that the bubbles in the 16 to 18 kHz range were much more energetic (by a factor of more than 10) than the bubbles in the adjacent frequency bins. The peak in the average spectrum at about 16 kHz for this drop size is probably due to these highly energetic bubbles, and may not have been prominent if a larger number of samples had been used. As mentioned earlier, some of the high frequency bubbles may actually have been secondary bubbles formed by splash droplets.

5. Average Impact Spectra and Total Fitted Spectra

The average impact spectra for the 2.5, 3.4, and 4.2 mm drops are shown in Figure 61. The broadband character of the impact sound is evident. Figure 62 is a

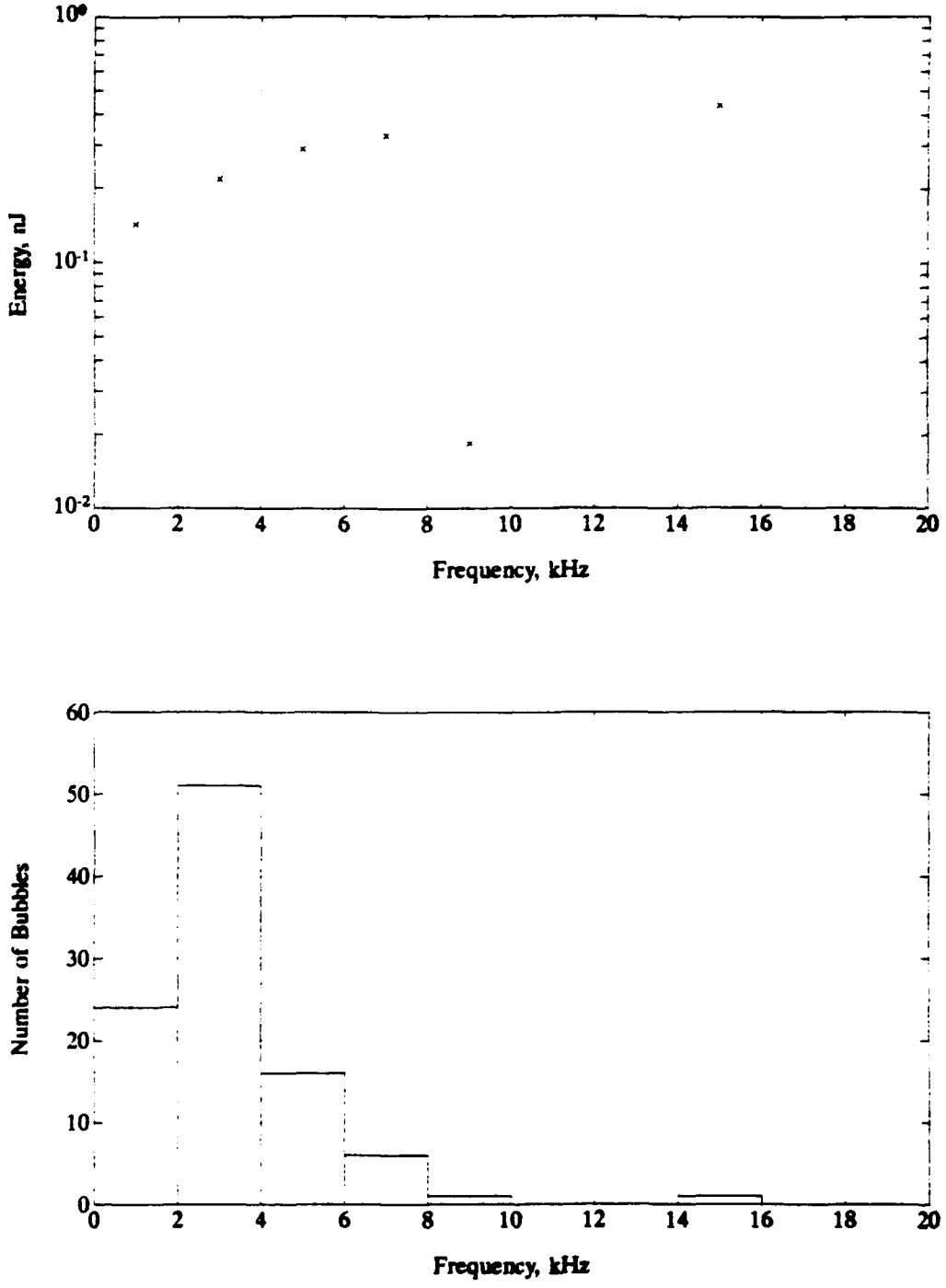

Figure 55. Average dominant bubble energy vs. frequency for the 4.6 mm drops (upper curve). Lower curve is a histogram of the number of bubbles per frequency bin. The energy value at 9 kHz may be anomalous.

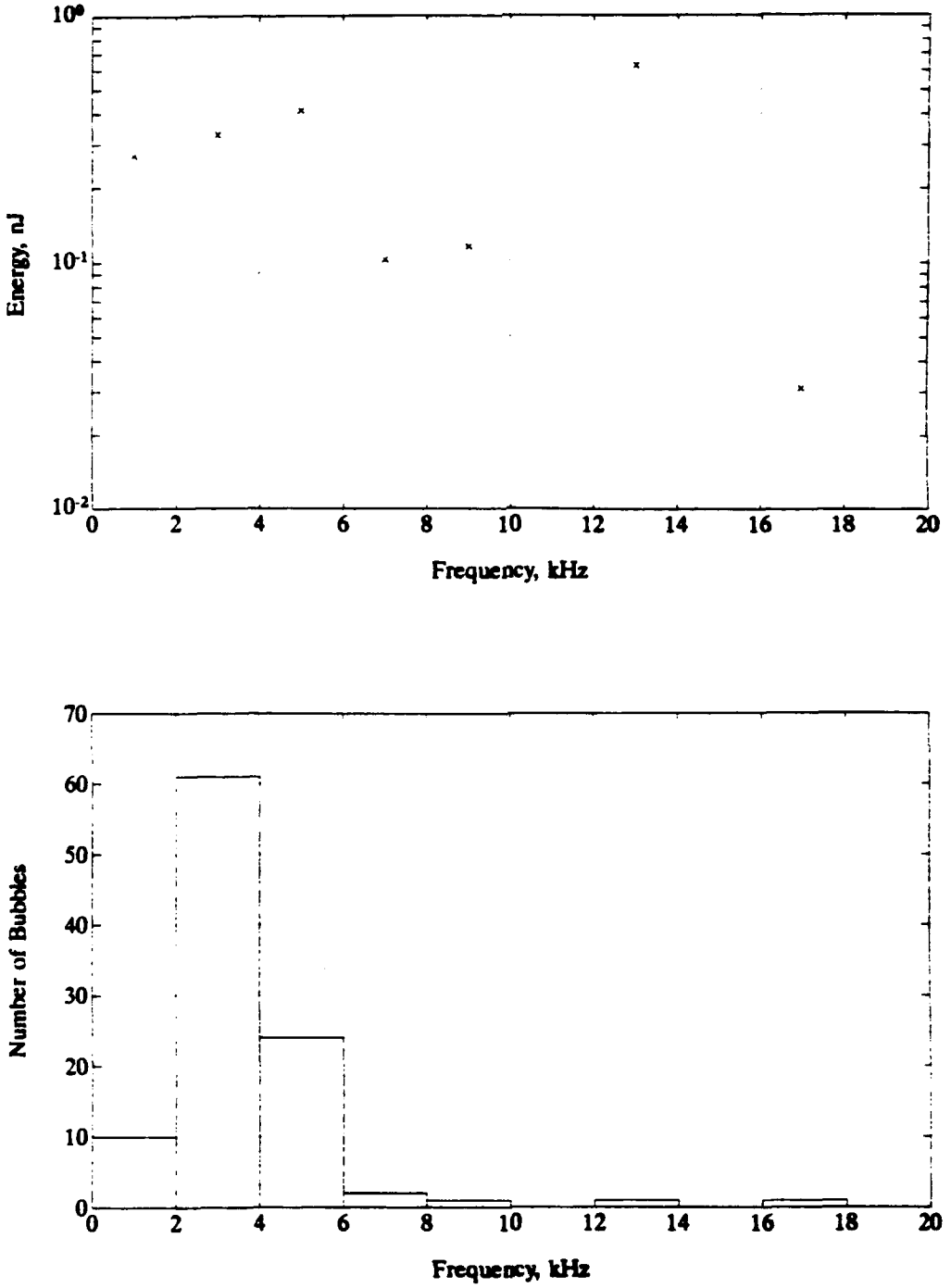

Figure 56. Average dominant bubble energy vs. frequency for the 4.2 mm drops (upper curve). Lower curve is a histogram of the number of bubbles per frequency bin.

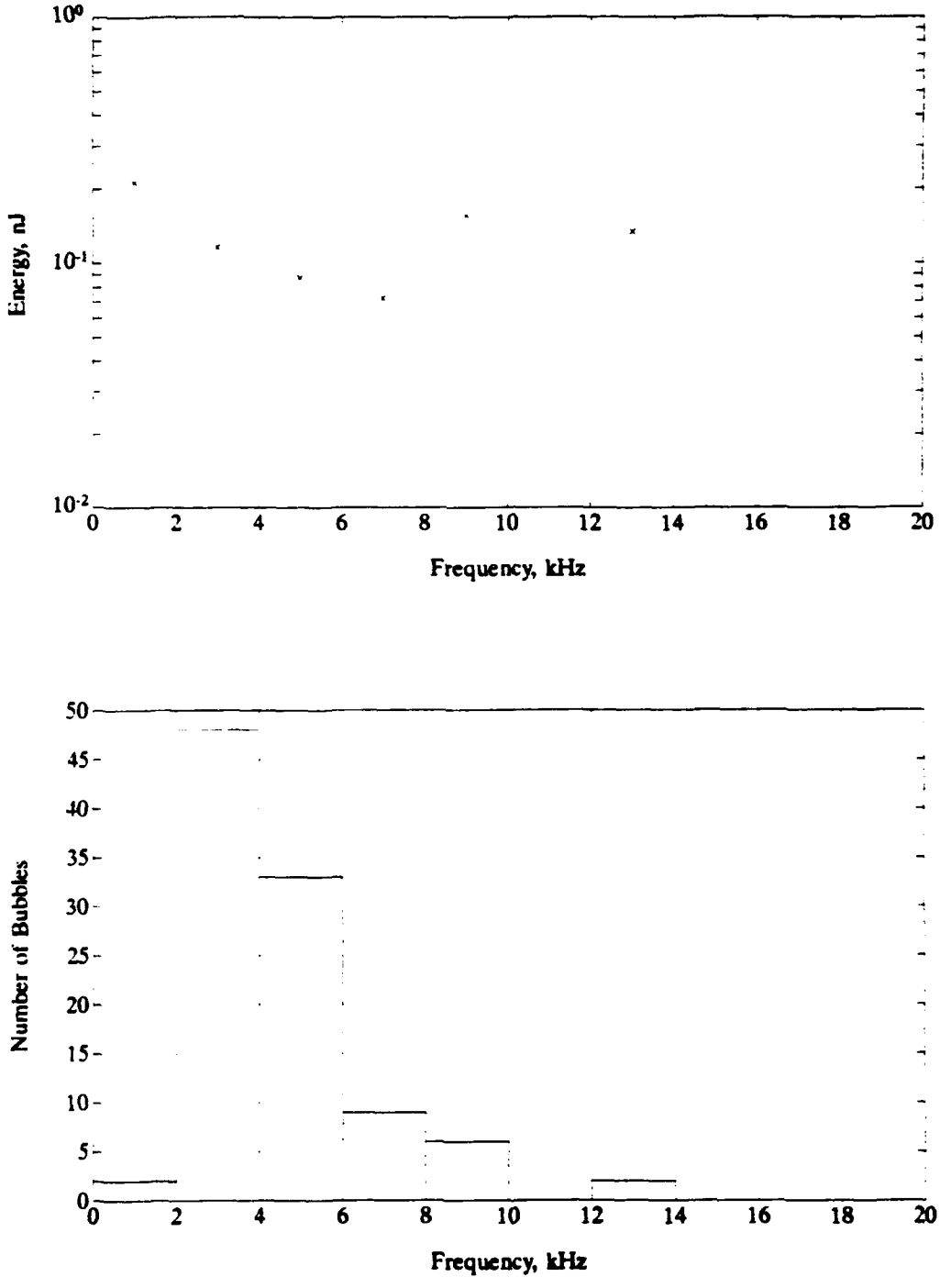

Figure 57. Average dominant bubble energy vs. frequency for the 3.8 mm drops (upper curve). Lower curve is a histogram of the number of bubbles per frequency bin.

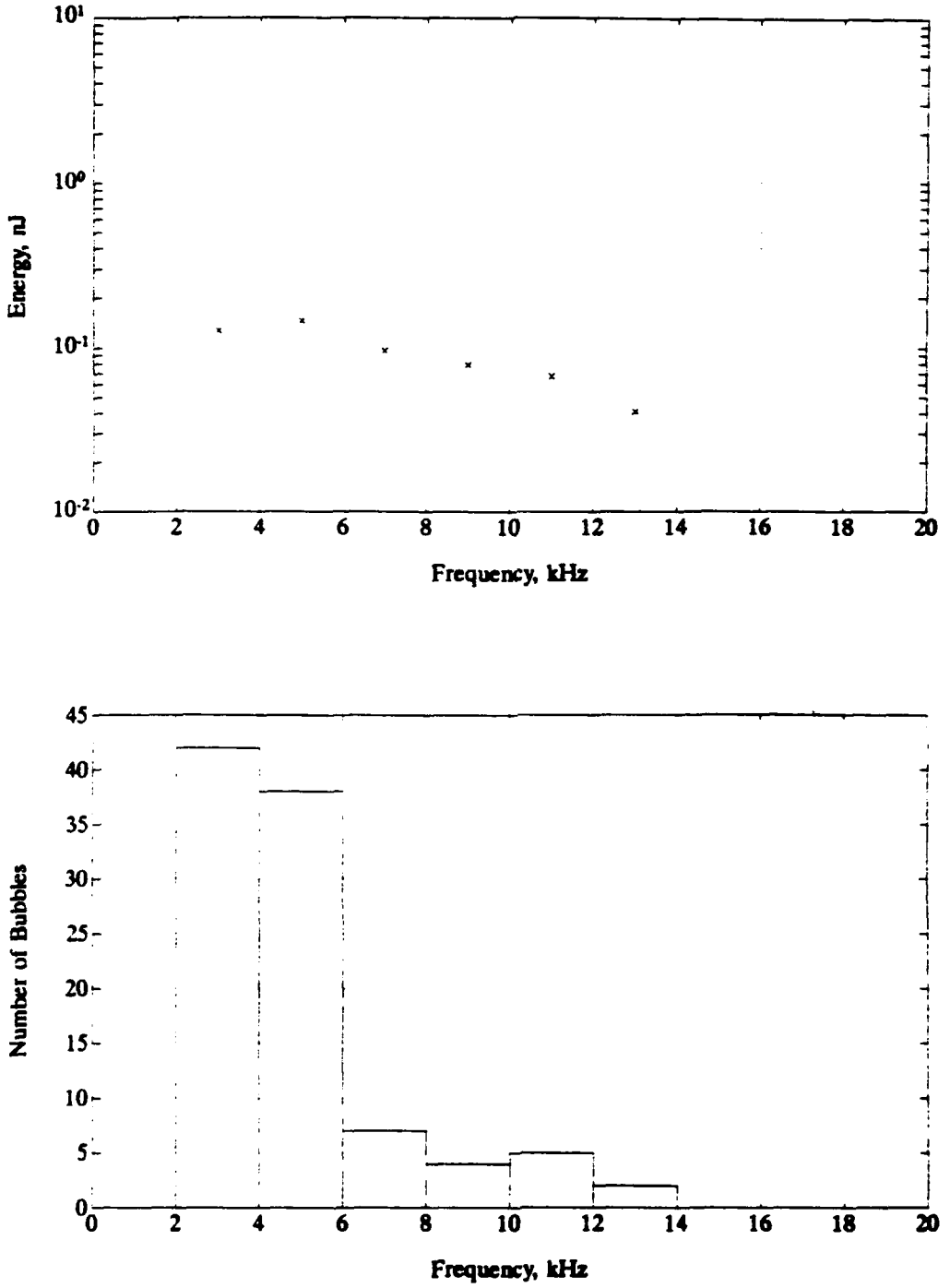

Figure 58. Average dominant bubble energy vs. frequency for the 3.4 mm drops (upper curve). Lower curve is a histogram of the number of bubbles per frequency bin.

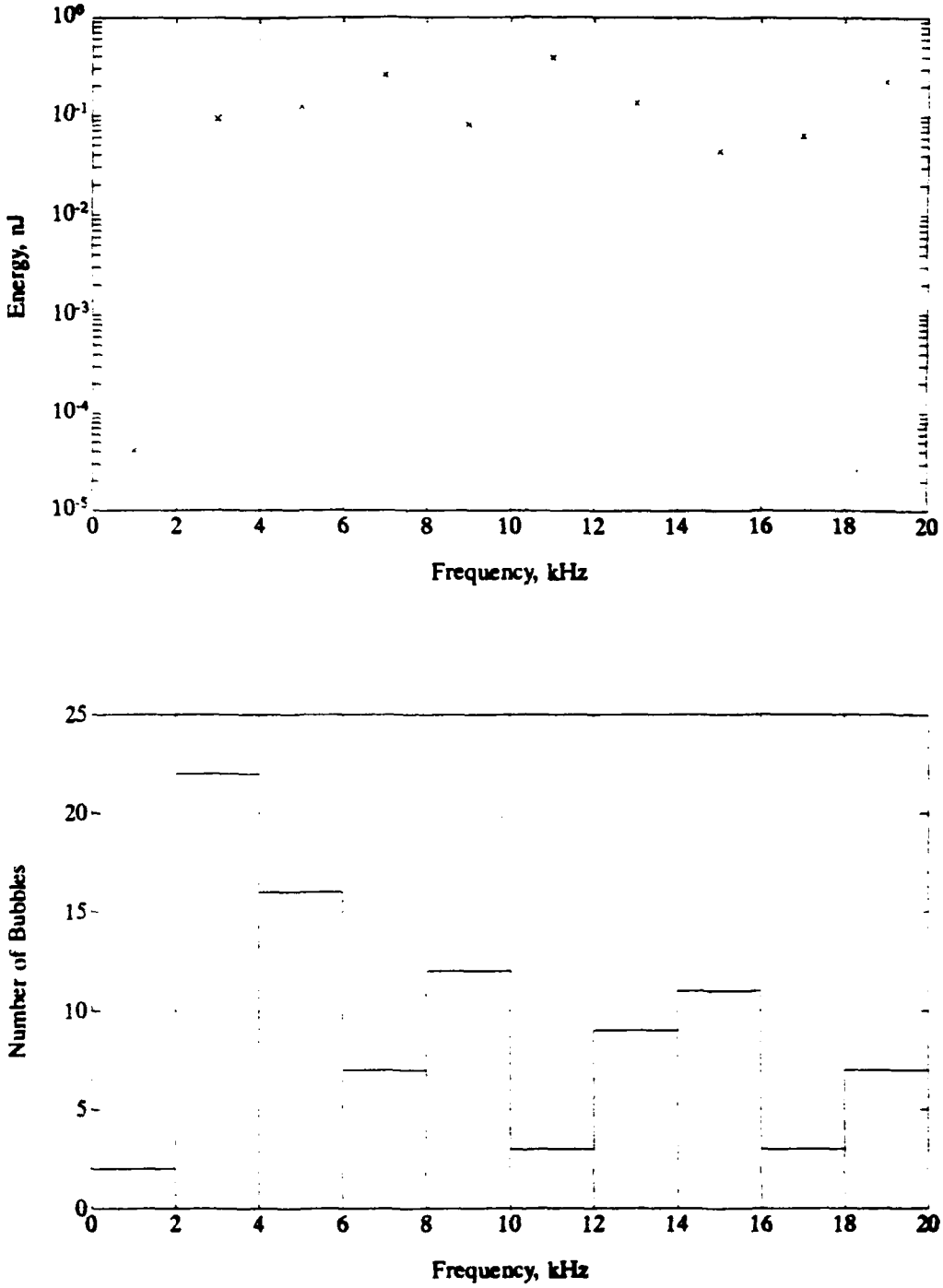

Figure 59. Average dominant bubble energy vs. frequency for the 3.0 mm drops (upper curve). Lower curve is a histogram of the number of bubbles per frequency bin.

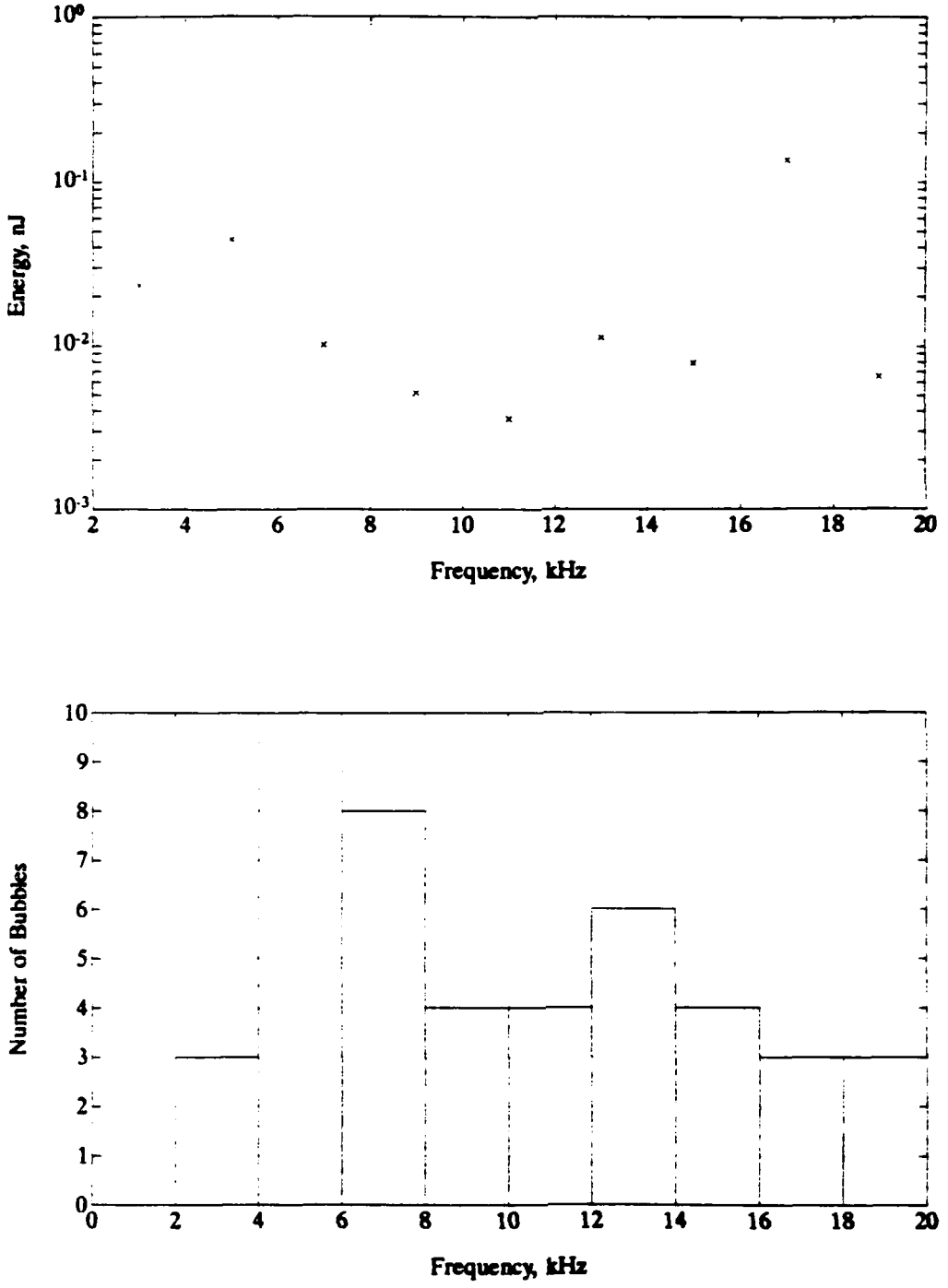

Figure 60. Average dominant bubble energy vs. frequency for the 2.5 mm drops (upper curve). Lower curve is a histogram of the number of bubbles per frequency bin.

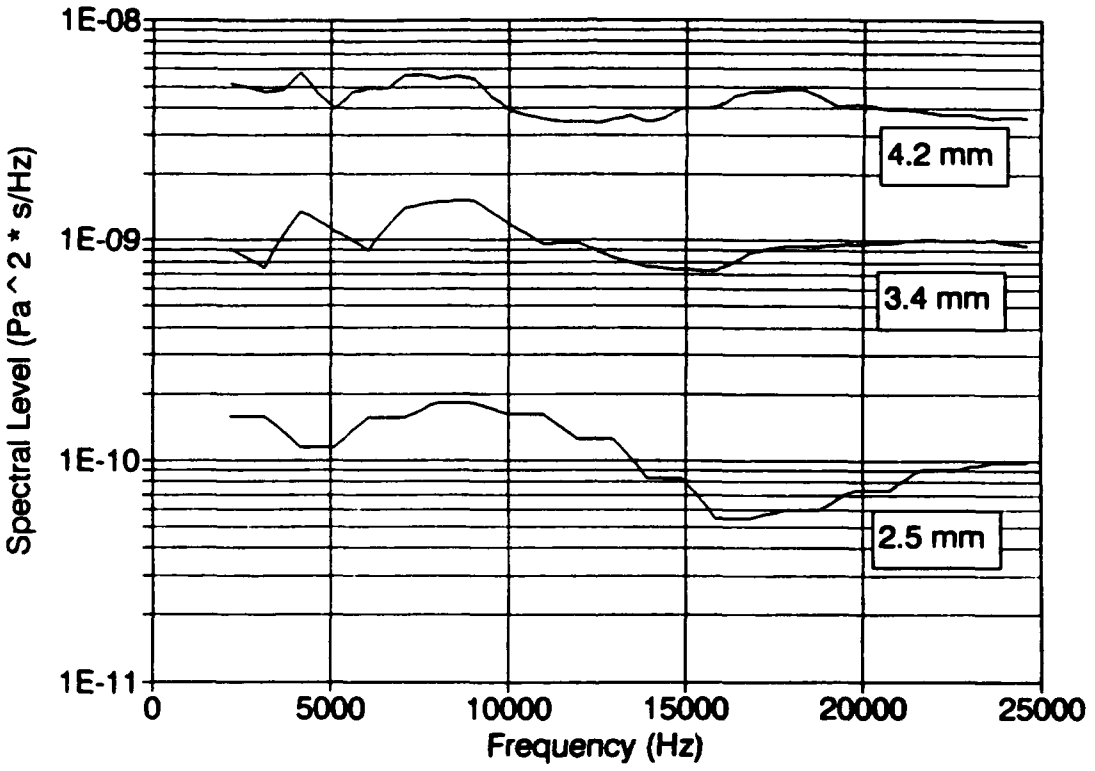

Figure 61. Impact energy spectra for the 2.5 mm, 3.4 mm, and 4.2 mm diameter drops.

plot of the impact signal energy (in pJ) versus drop diameter. The energy of the impact signals varies as the 4th power of the drop diameter (d) over this size range. This agrees with the result obtained by Kurgan (1989) and Jacobus (1991) that the radiated impact acoustic energy is proportional to the kinetic energy of the drops, given by $\frac{1}{2} mv^2$ (the mass m of a raindrop is proportional d^3 while the terminal velocity for large raindrops is proportional to $d^{1/2}$). The curve shown in Figure 62 was interpolated to obtain energy values for the other 3 drop sizes studied. The ratios of the impact energies were then multiplied by the measured spectra to obtain interpolated spectra for the other drop sizes.

All the impact spectra were then smoothed (using a 1 kHz moving average) and added to the smoothed bubble spectra. A summary of the total impact and fitted bubble spectra for each drop size is shown in Figure 63. The impact noise has some effect on the magnitude of the resulting spectra at the higher frequencies.

A summary of the peak spectral levels vs. drop size is presented in Table 9. The peak spectral levels for the smallest drops are at least an order of magnitude less than for the largest drops. The smaller drop sizes have less kinetic energy, and so less energy is available to drive the bubbles into oscillation. In general, the following

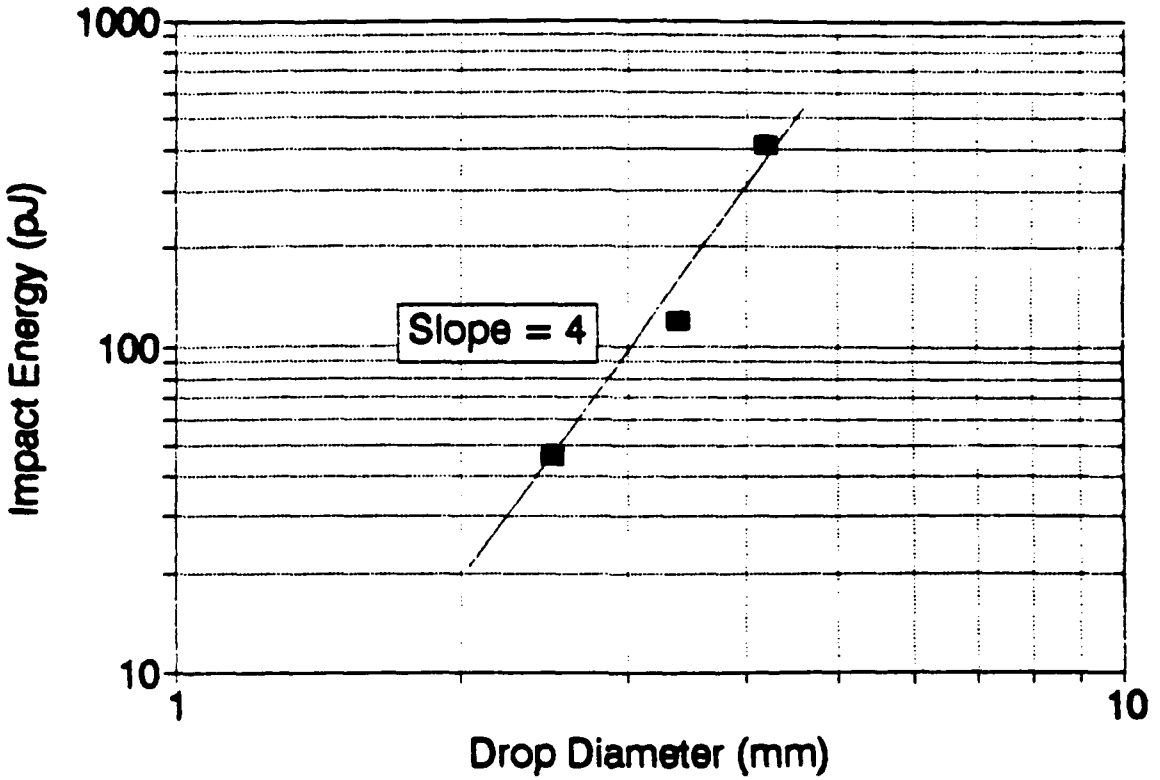

Figure 62. Impact signal acoustic energy (pJ) vs. drop diameter (mm). The curve is a least squares fit.

changes take place in the spectra with decreasing drop size:

- The spectral levels decrease.
- The spectra shift to higher frequencies.
- The spectra become broader.

The spectra shown in Figure 63 will be used in calculating the predicted underwater spectral levels at sea due to rainfall.

TABLE 9. PEAK SPECTRAL LEVELS VS. DROP SIZE

Drop Diameter (mm)	Peak Spectral Level ($Pa^2 \cdot s/Hz$)
2.5	$6.09 \cdot 10^{-10}$
3.0	$4.32 \cdot 10^{-9}$
3.4	$1.59 \cdot 10^{-8}$
3.8	$1.88 \cdot 10^{-8}$
4.2	$6.88 \cdot 10^{-8}$
4.6	$4.80 \cdot 10^{-8}$

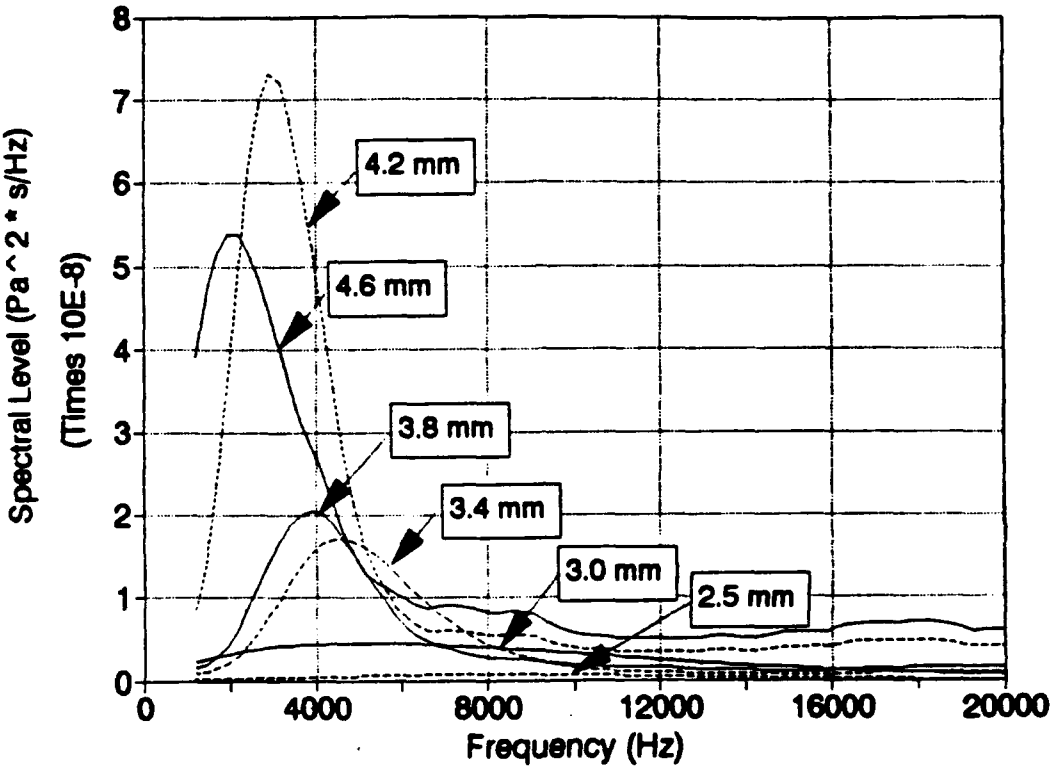

Figure 63. Total fitted energy density spectrum for each large raindrop size.

V. INVERTING THE FITTED RAINDROP SPECTRA

A. INVERSE THEORY

1. Terms and Definitions

Inverse techniques are of tremendous importance in a number of scientific fields, including ocean acoustical tomography and seismology. In simplest terms, the general linear inverse problem consists of finding the desired solution to a set of m equations in n unknowns. The inverse method described here follows the approach used by Wiggins (1972), who outlined an inverse technique for studying surface waves in the Earth.

Let $RS(f)$ represent the rainfall underwater acoustic spectrum measured at sea, and $DRD(d)$ the number of drops of a given drop size d falling per square meter per second. Also, let the function $A(f,d)$ represent the contribution to the underwater acoustic spectrum at the frequency f from raindrops of a given diameter d, such that:

$$RS(f) = \sum_{d} A(f,d) \cdot DRD(d) \tag{21}$$

where the summation is over all drop sizes. An expression for $A(f,d)$ will be derived later in determining the predicted underwater spectrum due to rainfall from the individual raindrop spectra.

Because the raindrop acoustic signatures have been measured only for distinct drop sizes, and because the measured spectral levels are also discrete, the function $A(f,d)$ must be expressed in discrete form. $A(f,d)$ then becomes a matrix, where the matrix entry A_{ij} gives the contribution to the underwater sound spectrum from a drop size range Δd centered on drop diameter d_j, to the frequency bin Δf centered on frequency f_i. In a similar fashion, the functions $RS(f)$ and $DRD(d)$ can be represented as vectors, where RS_i is the spectral value of a frequency bin centered at f_i, and DRD_j represents the drop rate density (number of drops per m^2 per sec) for drops of a given size range centered on diameter d_j. In what follows, matrices will be referred to using a capitalized bold letter, while vectors will be referred to using an uncapitalized bold letter. The frequency index i varies from 1 to m and the drop size index j varies from 1 to n.

Using the matrix notation, the discrete form of Equation 21 is:

$$\sum_{j=1}^{n} A_{ij} \cdot drd_j = rs_i, \qquad i = 1, m \tag{22}$$

which can be characterized as a set of m linear equations in the n unknown variables DRD_j. The coefficients of the variables are given by A_{ij}, and the solution of each

equation is rs_i. The set of equations can be expressed in terms of matrix algebra as:

$$\boldsymbol{A} \cdot \boldsymbol{drd} = \boldsymbol{rs} \tag{23}$$

where $\boldsymbol{A}$ is an m by n matrix, $\boldsymbol{rs}$ is the m by 1 solution vector containing the measured underwater spectral values at discrete frequencies f_i, and $\boldsymbol{drd}$ is the vector containing the unknown drop rate densities for the discrete drop sizes d_j.

The $\boldsymbol{A}$ matrix represents the contributions of each drop size range to the underwater spectral values in each frequency bin, and is therefore related to the physical mechanisms of underwater sound generation by raindrops. Later, a form of the $\boldsymbol{A}$ matrix will be derived using the individual raindrop spectra obtained in the previous chapter. The $\boldsymbol{A}$ matrix values, however, may also be determined statistically. A statistical method that could be used to obtain the $\boldsymbol{A}$ matrix coefficients will be discussed later when making suggestions for future work.

2. The Singular Value Decomposition Method

Singular Value Decomposition (SVD) is the method used by Wiggins (1972) to solve the linear system $\boldsymbol{A} \cdot \boldsymbol{drd} = \boldsymbol{rs}$ for the unknown vector $\boldsymbol{drd}$. However, unlike Wiggins problem, the linear system for our problem is overdetermined; that is, the number of unknowns (given by n) is less than the number of equations (given by m). Put differently, the number of frequency bins in the acoustic spectrum exceeds the

number of drop sizes studied. Unless at least $m - n$ of the equations are linearly dependent, an overdetermined linear system will have no exact solution for the unknown vector ***drd***. In this case, the linear system is said to be inconsistent (Anton and Rorres, 1987). In contrast, for an underdetermined system (where the number of unknowns exceeds the number of equations) an infinite number of solutions exist.

Even though the linear system for our problem is overdetermined, the Singular Value Decomposition method can still be used to obtain a solution. While an exact solution to the system of equations may not be possible, the SVD method will still yield a best fit solution to the system of equations in a least squares sense. That is, if the solution ***drd*** (obtained by Singular Value Decomposition) is multiplied by $\boldsymbol{A}$ to yield the vector rs', then the summation $\Sigma(rs_j - rs'_j)^2$ will be minimized.

The first step in the SVD method is to decompose the $\boldsymbol{A}$ matrix into the product of three different matrices, such that:

$$\boldsymbol{A} = \boldsymbol{U} \cdot \boldsymbol{\Lambda} \cdot \boldsymbol{V}^T \tag{24}$$

The matrix $\boldsymbol{U}$ is an m by k matrix that contains the eigenvectors of length m associated with the columns of the matrix $\boldsymbol{A}$. The matrix $\boldsymbol{\Lambda}$ is a diagonal matrix, where the diagonal elements are the eigenvalues of the matrix $\boldsymbol{A}$. The number of eigenvalues is k, where $k \leq n$, and n is the number of unknowns in the set of linear equations. The matrix $\boldsymbol{V}^T$ is the transpose of the n by k matrix that contains the

eigenvectors of length n associated with the rows of $\boldsymbol{A}$. Techniques for obtaining the eigenvectors and eigenvalues of a matrix $\boldsymbol{A}$ are presented in Anton and Rorres (1987). Singular Value Decomposition can be accomplished with the MATLAB program by using the function $SVD(\boldsymbol{A})$.

Once the matrix $\boldsymbol{A}$ has been decomposed, it can be substituted into Equation 23. Letting $\boldsymbol{V}^T \cdot \boldsymbol{drd} = \boldsymbol{drd}^*$, Equation 23 becomes:

$$\boldsymbol{U} \cdot \boldsymbol{\Lambda} \cdot \boldsymbol{drd}^* = \boldsymbol{rs} \tag{25}$$

Following Wiggins, the vector $\boldsymbol{drd}^*$ will be referred to as the parameter correction vector. Since the columns of the matrix $\boldsymbol{U}$ consist of eigenvectors that are orthonormal, the product $\boldsymbol{U}^T \cdot \boldsymbol{U}$ yields the identity matrix $\boldsymbol{I}$. The product of $\boldsymbol{\Lambda}^{-1} \cdot \boldsymbol{\Lambda}$ (where $\boldsymbol{\Lambda}$ is the eigenvalue matrix and $\boldsymbol{\Lambda}^{-1}$ is its inverse) is also the identity matrix $\boldsymbol{I}$ by definition. The inverse of the matrix $\boldsymbol{\Lambda}$ is obtained by simply inverting the diagonal elements of $\boldsymbol{\Lambda}$. Multiplying both sides of Equation 25 by $\boldsymbol{\Lambda}^{-1} \cdot \boldsymbol{U}^T$ and applying the rules of matrix algebra leads to:

$$\boldsymbol{drd}^* = \boldsymbol{\Lambda}^{-1} \cdot \boldsymbol{U}^T \cdot \boldsymbol{rs} \tag{26}$$

An estimate for the unknown vector $\mathbf{drd}$ can then be obtained from the solution for $\mathbf{drd}^*$ from:

$$\mathbf{drd} \approx \mathbf{V} \cdot \mathbf{drd}^* \tag{27}$$

The above expression is only approximately true, because the product $\mathbf{V} \cdot \mathbf{V}^T$ does not necessarily yield an identity matrix (the eigenvectors are in the columns of $\mathbf{V}$ and in the rows of $\mathbf{V}^T$, and matrix multiplication involves multiplying the rows of the first matrix by the columns of the second matrix). The product $\mathbf{V} \cdot \mathbf{V}^T$ is referred to as the resolution matrix $\mathbf{R}$. The more the $\mathbf{R}$ matrix resembles an actual identity matrix (with diagonal elements equal to 1 and off diagonal elements equal to zero), the better the solution $\mathbf{drd}$ is resolved.

3. Effect of Noise on the Inverse Technique

A solution for $\mathbf{drd}^*$ can also be obtained using fewer than the maximum number of eigenvalues. To truncate the number of eigenvectors and eigenvalues to a value k, all the columns of $\mathbf{U}$ and $\mathbf{V}$ with indices greater than k are eliminated, as well as all columns and rows of $\mathbf{A}$ with indices greater than k. The effect of truncating the decomposition matrices is to reduce the goodness of fit of the calculated under-water spectrum $\mathbf{rs'} = \mathbf{A} \cdot \mathbf{drd}$ as compared to the measured spectrum $\mathbf{rs}$.

If the linear system described by Equation 23 were a perfect system, that is, if there were no errors in either the vector $\vec{rs}$ or in the matrix $\mathbf{A}$, then the best solution for $\vec{drd}$ would be the solution obtained using the maximum number of eigenvalues, since this solution would yield the closest fit between the predicted and measured spectral levels. However, errors in the linear system (regardless of their source) will affect the results of inversion. The cumulative errors in the linear system relating the underwater acoustic levels to the drop rate density of drops striking the surface will be referred to as the system noise, and will be represented as a vector $\vec{e}$. The noise can be due to either random or biased errors. Possible sources of noise include:

- Measurement errors.
- Modelling errors.
- Effects not accounted for (wind noise, for example).

The equation for the linear system (Equation 23) can be rewritten so as to include the cumulative noise effects:

$$\mathbf{A} \cdot \vec{drd} + \vec{e} = \vec{rs} \tag{28}$$

Solving for $\mathbf{A} \cdot \vec{drd}$, Equation 28 becomes:

$$\mathbf{A} \cdot \vec{drd} = \vec{rs} - \vec{e} \tag{29}$$

Thus, the solution $\mathbf{drd}$ obtained using the SVD method in fact yields a best fit to $\mathbf{rs} - \mathbf{e}$ rather than the best fit to $\mathbf{rs}$ alone. Significant differences between $\mathbf{rs}$ and $\mathbf{rs} - \mathbf{e}$ will lead to errors in the inverse solution $\mathbf{drd}$. It may be true that a less perfect fit to the spectrum, obtained using fewer than the maximum number of eigenvalues and eigenvectors, will actually yield a better solution for the vector $\mathbf{drd}$. This possibility must be considered when applying the inversion method.

In the following section, a form for the $\mathbf{A}$ matrix will be presented. Then, using a drop rate density vector computed from the Marshall-Palmer raindrop distribution, the underwater spectral levels for a given rainfall rate will be calculated, and compared to spectra measured at sea for similar rainfall rate conditions. If the predicted and the measured underwater acoustic spectra are in reasonable agreement, then an inversion technique based on the derived matrix $\mathbf{A}$ should be possible.

B. SOLUTION OF THE FORWARD PROBLEM

1. Calculations

Jacobus (1991) derived an expression for the underwater acoustic spectrum due to rainfall measured at an upward looking hydrophone at some depth below the

surface. The expression is duplicated here in modified form:

$$RS(f) = \sum_d \pi \times DRD(d) \times E(f,d) \times \sin^2 \psi(f) \times 1 \text{ m}^2 \qquad (30)$$

where $DRD(d)$ is the drop rate density (in units of drops/m^2 s) for each drop size, $E(f,d)$ is the energy density spectrum (in units of Pa^2· s/Hz) for each drop size, and $\psi(f)$ is the beamwidth of the receiving hydrophone. The summation is over all drop sizes d. A derivation of Equation 30 is presented in Appendix C. The rainfall spectrum can then be expressed in units of dB re μPa^2/Hz using the equation:

$$RSL(f) = 10 \cdot \log[RS(f)] + 120 \qquad (31)$$

Comparing Equation 30 with Equation 21 from the previous section, the function $A(f,d)$ that relates drop sizes to spectral levels is determined to be:

$$A(f,d) = \pi \cdot \sin^2 \psi(f) \cdot E(f,d) \cdot 1 \text{ m}^2 \qquad (32)$$

The matrix (discrete) form of A is given by:

$$\boldsymbol{A} = \pi \cdot 1 \text{ m}^2 \cdot \sin^2 \psi(f) \cdot \boldsymbol{E} \qquad (33)$$

Each column of the matrix $\boldsymbol{E}$ contains the average energy spectrum (in Pa^2· s/Hz) for a given raindrop size.

Energy spectra have been measured for six large raindrop sizes, where the fitted spectra contain 82 frequency bins between 1.2 kHz and 21 kHz. A trial $\boldsymbol{E}$

matrix was constructed with dimensions i = 1 to 82 and j = 1 to 6. The $\boldsymbol{E}$ matrix was then substituted into Equation 33 to obtain a trial $\boldsymbol{A}$ matrix. The $\boldsymbol{A}$ matrix was then multiplied by an estimate of the drop rate density vector (***drd***) for a given rainfall rate to yield a prediction for the underwater acoustic spectrum due to rainfall.

The computed spectrum was then compared to actual rainfall noise spectra measured at sea for the same rainfall rate. The at-sea spectra were determined by Tan (1990) and McGlothin (1991) from data obtained at the Ocean Test Platform (OTP) facility in the Gulf of Mexico. The location of the OTP is shown in Figure 64.

The OTP hydrophone is an ITC-3001 (circular piston) transducer with a beamwidth of 28 degrees at 17.5 kHz, and is mounted in a concrete foundation in 15 m of water. The directivity function for a circular piston transducer is given by $D_{\Lambda} = 2 \cdot |J_1(v)| / v$, where $v = ka \cdot \sin\theta$ and J_1 is the 0th Order Bessel Function (eg., see Ziomek, 1985). In the expression for v, ka is the product of the wavenumber and the piston radius, and θ is the angle between the field point and the acoustic axis of the piston. The 3 dB beamwidth is given by a value of $v = 2.2$, and so the beamwidth of the OTP hydrophone can be estimated as a function of frequency. The result is shown in Figure 65. The estimated OTP beamwidth was used in computing the $\boldsymbol{A}$ matrix values. For frequencies below 8 kHz, the beam pattern of the OTP hydrophone is omnidirectional.

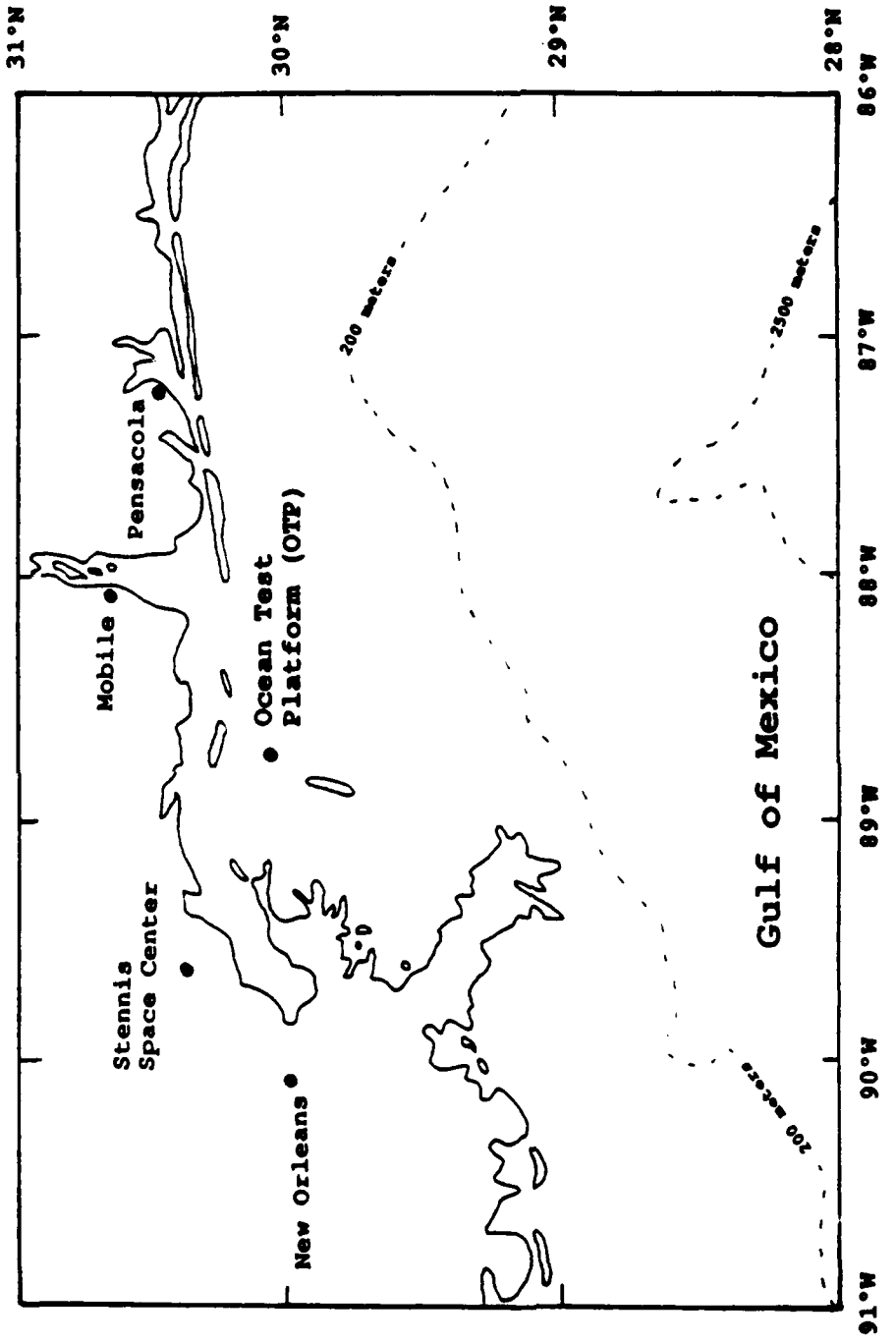

Figure 64. Location of the Ocean Test Platform.

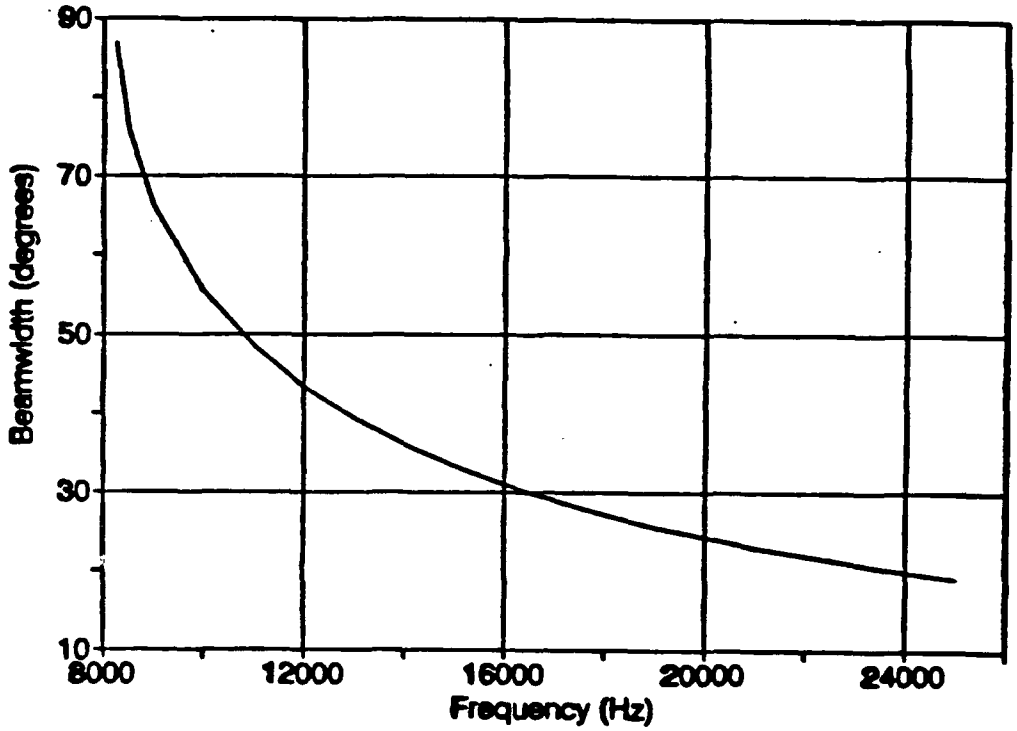

Figure 65. OTP hydrophone beamwidth vs. frequency.

Estimates of the drop rate density vector were obtained for two rainfall rates, 15 mm/hr and 100 mm/hr. The estimates were computed using the Marshall-Palmer drop size distribution described in Chapter II. The values $N(d)$ (number of drops per m^3 per 0.1 mm diameter increment) from the Marshall-Palmer distribution were converted to drop rate density values using the equation:

$$DRD(d) = N(d) \cdot v_t(d) \cdot \Delta d \qquad (34)$$

where d is the drop diameter (mm), v_t is the drop terminal velocity (m/s), and Δd is the drop size range (in tenths of mm) centered on diameter d. The results are shown in Table 10 for the two rainfall rates.

2. Results

The rainfall spectra obtained by multiplying the A matrix by the estimated drop rate density vectors are shown in Figure 66. It should be noted that the effects of small and midsize raindrops were not included in obtaining the predicted levels. The peak spectral level for the 100 mm/hr rainfall is predicted to be 74.5 dB (re $\mu Pa^2/Hz$). The peak level for the 15 mm/hr rainfall is predicted to be 62 dB. Both of the predicted spectra have a negative slope of 10 to 11 dB per octave for frequencies greater than 8 kHz. All estimates assume that measurements are made in the free field (eg., away from surfaces).

The predicted underwater acoustic spectra are only in approximate agreement with the rainfall spectra measured at sea. Figure 67 shows the predicted 15 mm/hr rainfall spectrum, along with rainfall sound spectra measured at the Ocean Test Platform for the same rainfall rate. The ocean measurements have been referenced to free field values by correcting for reflection from the rigid concrete pad surrounding the OTP hydrophone. This is done by subtracting 6 dB from the measured spectral levels for frequencies greater than 1 kHz. The basis for this

Table 10. DROP RATE DENSITIES VS. RAINDROP SIZE

		Drop Rate Density (drops/m^2s)	
Mean Drop Size	Size Range	15 mm/hr Rainfall Rate	100 mm/hr Rainfall Rate
2.5	2.2-2.8	109	729
3.0	2.8-3.2	24.9	241
3.4	3.2-3.6	10.2	135
3.8	3.6-4.0	4.13	74.2
4.2	4.0-4.4	1.67	40.6
4.6	4.4-4.8	0.67	22.7

correction will be described later. The wind speeds during the various rainfall events are shown in the upper right corner of the figure. Wind speeds were moderate for all three cases. The spectral levels for two of the rainfall events are above the predicted spectral levels by 5 to 10 dB for frequencies greater than 8 kHz and by 0 to 5 dB for frequencies between 5 kHz and 8 kHz. As discussed later, the measured levels below about 5 kHz are judged to be unreliable due to probable errors in the OTP hydrophone calibration.

The spectral levels for the third rainfall event shown in Figure 67 are much lower than for the other two rainfall events, and are less than the predicted spectral levels by as much as 15 dB for frequencies between 4 and 12 kHz. It is speculated that

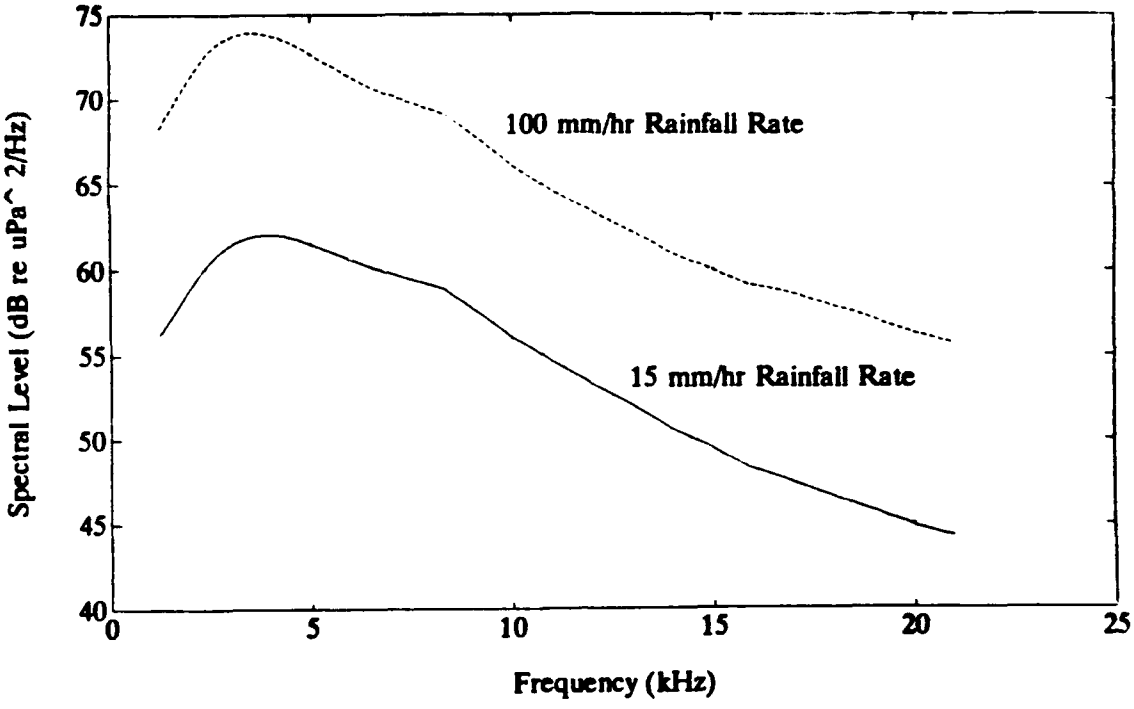

Figure 66. Predicted rainfall spectra for rainfall rates of 15 mm/hr and 100 mm/hr.

the third spectrum was measured during a period when the number of large raindrops present was significantly less than for the other two cases.

A smaller difference between the predicted and the measured spectral levels at the higher frequencies was observed for the 100 mm/hr rainfall rate. Measured rainfall spectra for three events are compared with the predicted 100 mm/hr rainfall spectrum in Figure 68. For the two events with moderate wind speeds (6 to 7 m/s), the measured spectra are 3 to 9 dB greater than the predicted spectrum for frequencies greater than 10 kHz, and are within 6 dB of the predicted spectrum for frequencies

between 5 kHz and 10 kHz. Once again, the measured spectral levels below about 5 kHz are judged to be unreliable.

The third measured spectrum in Figure 68 was for a rainfall event where the wind speed was high. The spectral levels for frequencies greater than about 10 kHz are significantly less for this third event than for the other two events. As mentioned in Chapter II, the attenuation of the rainfall sound for frequencies greater than about 10 kHz in the presence of high winds is probably due to subsurface bubble plumes generated by breaking waves.

As mentioned earlier, the small and midsize drops were not included in the computation of the predicted rainfall spectrum. The characteristic 15 kHz peak associated with the small (Type I) drops has not been observed at the OTP during moderate to heavy rainfall conditions, indicating diminished production of Type I bubbles. Also the small drop bubble noise is dependent on wind speed. For these reasons, small drops were excluded from the rainfall spectrum computations.

To estimate the contribution to the spectrum from the midsize drops (which only generate impact noise), the relationship between drop diameter and impact energy was extrapolated to four of the midsize drop diameters. The drop diameters used were 1.15 mm, 1.45 mm, 1.75 mm, and 2.05 mm. The extrapolated midsize impact energies were then divided by the impact energy for the 2.5 mm drops,

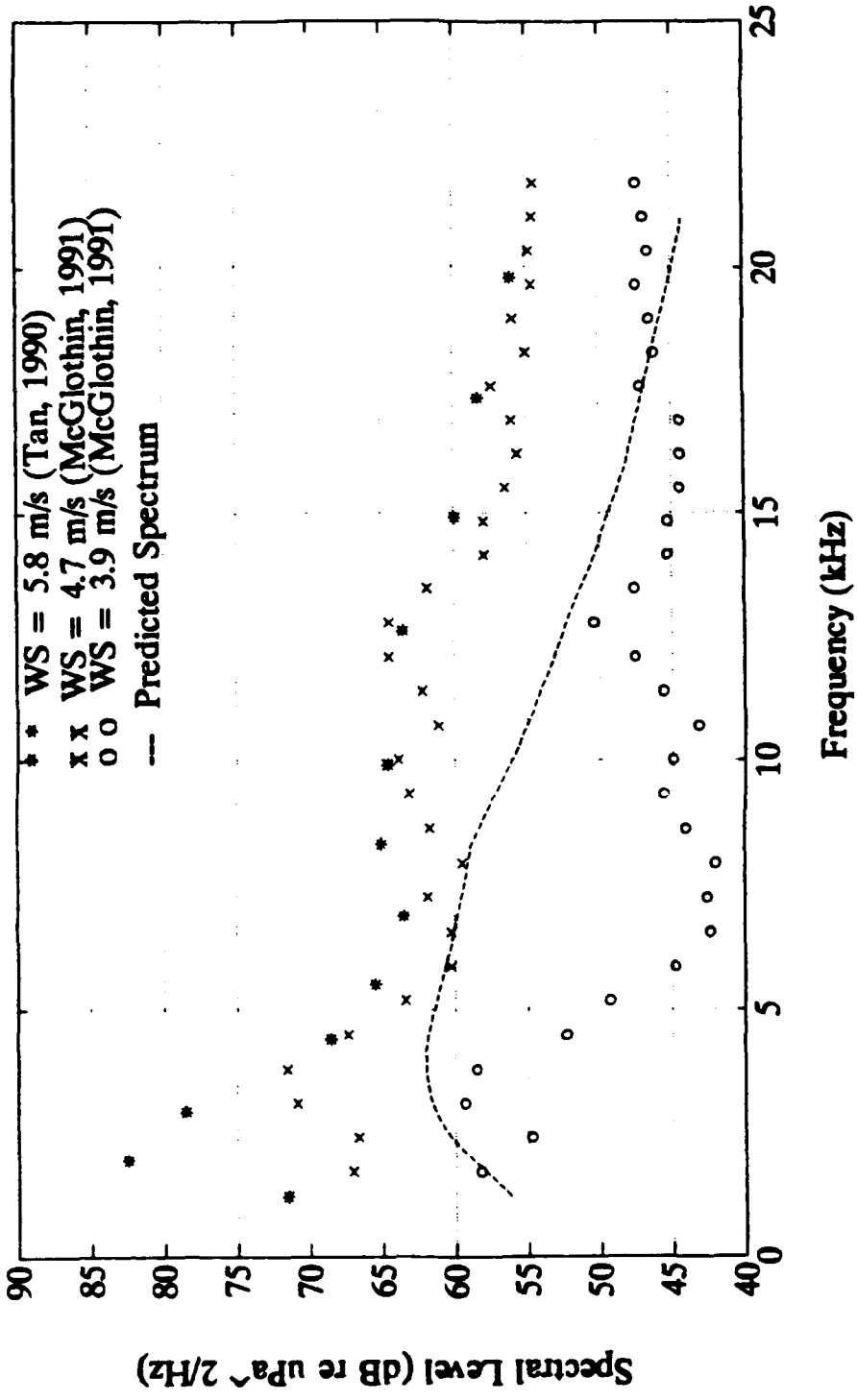

Figure 67. Predicted vs. measured rainfall spectra, 15 mm/hr rainfall rate. WS is the wind speed.

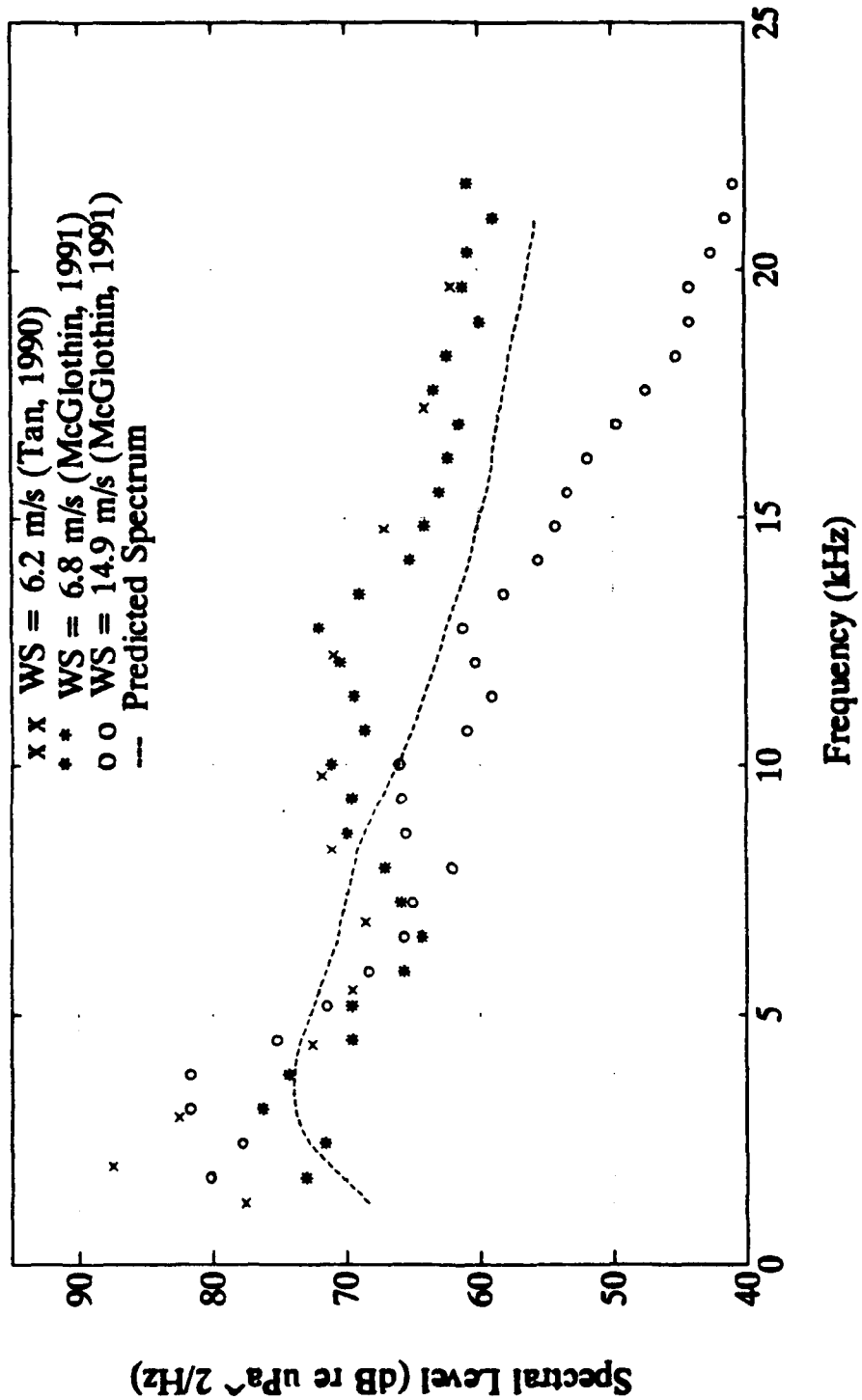

Figure 68. Predicted vs. measured rainfall spectra, 100 mm/hr rainfall rate. WS is the wind speed.

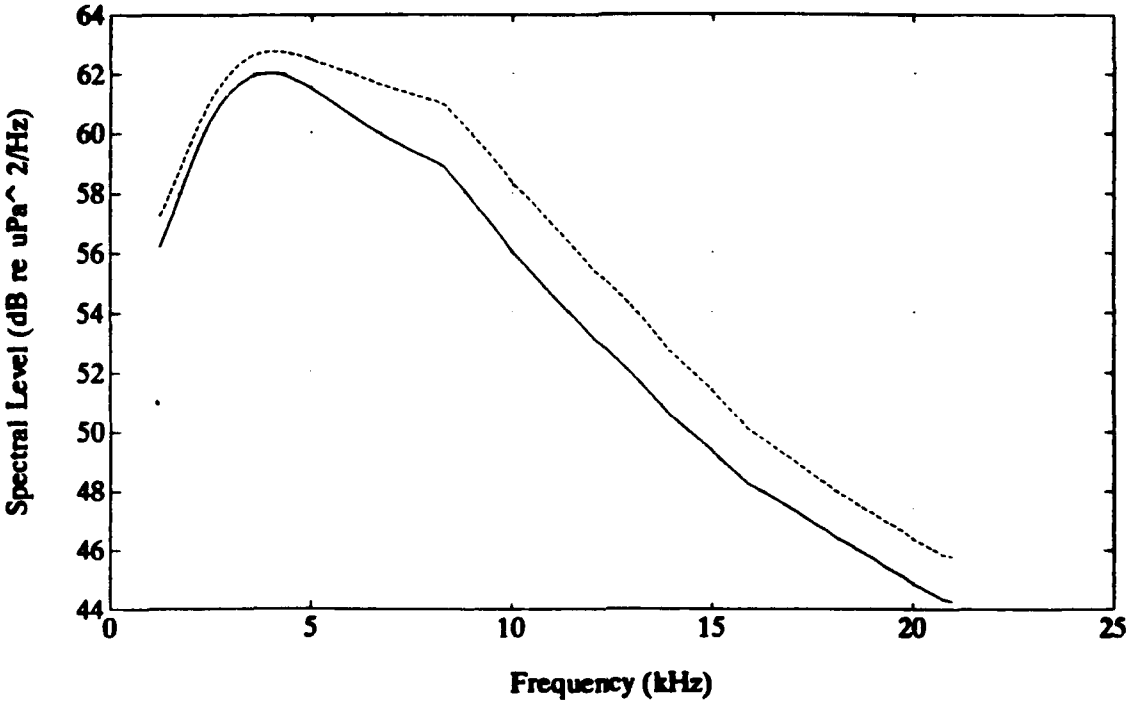

Figure 69. Effect of midsize raindrops on the predicted 15 mm/hr rainfall spectrum. The dashed curve includes the contribution of midsize drops.

and the ratio multiplied by the 2.5 mm raindrop impact spectrum. The midsize impact spectra were used to augment the ***A*** matrix, which was then multiplied by the drop rate density vector which included the midsize drops. The result is shown in Figure 69 for the 15 mm/hr rainfall rate and Figure 70 for the 100 mm/hr rainfall rate. Including the estimated effect of the midsize impacts raised the spectral levels by as much as 2 dB for the 15 mm/hr rainfall rate and 1 dB for the 100 mm/hr rainfall rate. Apparently, the effect of the midsize raindrop impacts on the underwater spectral levels cannot be ignored.

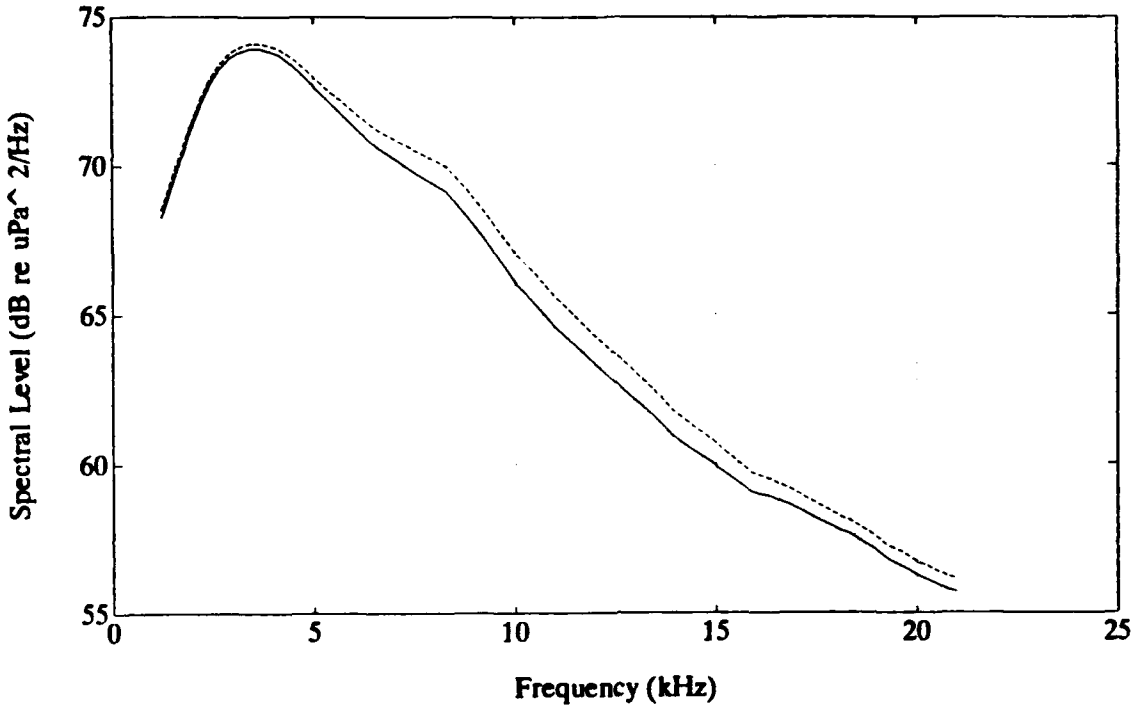

Figure 70. Effect of midsize raindrops on the predicted 100 mm/hr rainfall spectrum. The dashed curve includes the contribution of midsize drops.

3. Discussion

Recall that the measured spectral levels for most of the rainfall events were larger than the predicted spectral levels for frequencies greater than about 10 kHz. The reason(s) for these differences must be determined. The factors that may be responsible for this can be divided into two categories: those that cause the measured spectral levels to be too high and those that cause the predicted spectral levels to be too low.

One of the factors which could result in measured spectral levels that are too large is the scattering effect of the OTP hydrophone mounting. The OTP hydrophone is mounted flush in a concrete block. The radius of the hydrophone's receiving surface is about 10 cm, while the block's maximum dimension on its upper surface is about 2 feet or 60 cm. The presence of the block has a tremendous effect on the pressure measured at the hydrophone. When the wavelength of incident sound is significantly less than the dimensions of the block, the block will behave as a rigid baffle with respect to the hydrophone. For a simple receiver in the vicinity of an infinite baffle, the measured intensities are increased by a factor of 6 dB. The frequency corresponding to a half-wavelength of 0.6 m (the maximum dimension of the block) is about 1 kHz. However, the beam pattern of the hydrophone becomes directional above about 8 kHz. The overall effect that the hydrophone mounting has on the pressure measured at the hydrophone is therefore a complicated function of the frequency. The correction of 6 dB to the measured spectral levels for frequencies greater than 1 kHz is an approximation to this. An attempt must be made to more accurately quantify the effect of the hydrophone mounting on the measured levels.

Another factor which could result in higher than actual measured levels are hydrophone calibration errors. These errors will be most pronounced below 5 kHz, the frequency below which no hydrophone sensitivity values were provided by the

hydrophone manufacturer. An in-situ calibration of the ITC-3001 hydrophone has been conducted, and the calibration data is currently being analyzed with the intent of obtaining reliable hydrophone sensitivity values for the frequency range of interest.

A number of factors may be responsible for making the predicted sound levels too low. The first is the effect of ocean surface roughness. The effect of surface roughness on the sound generated by individual large raindrops has not yet been studied. It may be possible, for instance, that the bubble formation percentages increase in the presence of surface roughness, and may even result in Type II bubble formation extending to drop sizes less than 2.2 mm diameter. Work is currently in progress here at NPS to measure the influence that surface roughness has on large raindrop underwater sound.

Another factor that would make the predicted levels too low is the presence of a greater number of large raindrops in the raindrop size distributions than given by by the Marshall-Palmer distribution. Many of the rainfall events studied by Tan (1990) and McGlothin (1991) occurred during periods of convective rainfall. As discussed in Chapter II, the characteristics of raindrop size distributions can differ markedly from the Marshall-Palmer distribution and in fact depend on the type of precipitation. A drop size measuring device needs to be acquired in order to measure drop size distributions and underwater spectral levels concurrently.

A third factor that may be responsible for making the predicted spectral levels too low is the failure to account for the acoustic propagation conditions at the Ocean Test Platform. The OTP hydrophone is in a shallow water environment in which reverberation (eg., multipath arrival) must be considered. The expression for the $\boldsymbol{A}$ matrix was derived assuming free field conditions. It is recommended that open ocean measurements of the rainfall underwater sound spectrum be obtained, since the spectra measured in the open ocean should be in closer agreement with the spectral levels that are predicted using the free field derivation. For now, an attempt must be made to take into account the propagation conditions at the OTP.

Another factor which may make the predicted levels too low are the effects of water property variations on the energy radiated by individual raindrops. Since the laboratory measurements were performed using seawater, the effect of differences between ocean salinity and laboratory tank salinity should be small. Jacobus (1991) empirically determined that the large raindrop acoustic energy is proportional to the expression $(1 - sal / 77)$, where sal is the salinity in ppt. Based on this result, differences between the open ocean salinity and the laboratory tank salinity should not cause the predicted spectral levels to be underestimated by more than about 0.1 dB.

Temperature effects, however, have a significant impact on the sound energy radiated by large raindrops. Jacobus (1991) determined that the energy

radiated by large raindrops was linearly correlated with the absolute temperature difference between the raindrop and the water surface. For example, for 4.2 mm drops in fresh water Jacobus obtained the expression $E = 540 + 38 \cdot \Delta T$, where E is the raindrop acoustic energy in picojoules, and ΔT the drop-surface temperature difference in °C. Because Jacobus's spectral analysis technique was flawed, this expression is not strictly correct. However, the expression can be used to estimate the effect of drop-surface temperature differences if it is assumed his spectral analysis error affected all of his results uniformly. Using Jacobus's expression, raindrops of 4.2 mm diameter whose temperature difference with the surface is 20° C will radiate approximately 3.8 dB more energy than raindrops that are at the same temperature as the surface. No measurements of raindrop temperatures have been made at the OTP, but it is possible that drop-surface temperature differences at sea were significantly larger than for the laboratory measurements.

The effect of surface tension variations on the sound radiated by large drops has not yet been studied. The surface tension of the tank water was lower than for clean seawater by as much as 20 dynes/cm for some of the measurements, suggesting that surface contamination may have been present. A study of the surface tension effects on the sound generation by large raindrops should be performed.

Another factor that would tend to make the predicted spectral levels too low is that Type I raindrop bubbles were excluded from the prediction. As mentioned previously, the spectral peak at 15 kHz that is associated with the Type I raindrop bubbles is absent in the presence of moderate and heavy rainfall, indicating that Type I bubble formation is diminished. Some unknown fraction of small raindrop bubbles may still be present during moderate and heavy rainfall.

A study currently in progress of the damping constants of raindrop bubbles in fresh and salt water has revealed that the lower frequency bubble signals collected in the redwood tank are contaminated to some extent by scattering of sound from the tank walls. It was suspected that tank scattering would increase the energy measured for individual raindrops, which in turn would result in higher than actual spectral level predictions. To estimate the magnitude of the error due to tank reverberation, dominant bubble signals of various frequencies were compared with the energies of simulated bubble signals with the same amplitude and frequency, but with damping constants equal to the theoretical values. The energy difference between the measured and theoretical signals was on the order of $\pm$ 1 dB, with no observed dependence on frequency.

C. SUGGESTIONS FOR FUTURE WORK

As mentioned earlier, a statistical approach could be used to obtain an inversion matrix $\boldsymbol{A}$. This would be accomplished by making simultaneous measurements of raindrop size distributions and rainfall spectral levels. For each frequency bin of the rainfall spectrum, a multiple linear regression could then be performed between the rainfall spectral level and the drop rate densities for the various drop sizes. The regression coefficients obtained for a single frequency bin would correspond to one row of the $\boldsymbol{A}$ matrix described earlier.

Comparing the $\boldsymbol{A}$ matrix coefficients obtained using the statistical approach with the similar coefficients obtained from the laboratory measurements would shed some light on the physical processes of raindrop underwater sound generation. Variations in the coefficients due to wind speed and surface roughness could also be studied. The procurement of a raindrop size measuring device for data collection at the Ocean Test Platform site is anticipated.

VI. CONCLUSIONS

The original goal of this study was to develop an inversion technique for measuring rainfall using laboratory measurements of the underwater sound generated by large raindrops. The laboratory measurements conducted here provide the basis for the forward problem required as part of the inversion. Differences between the measured and predicted rainfall spectra need to be accounted for before inversion of the rainfall spectra to obtain rainfall rate is attempted. The work accomplished here provided additional insights into the physical mechanisms for underwater sound generation by individual raindrops. For instance, the study revealed that:

- The far field impact sound of rainfall consists primarily of impulsive broadband noise.
- The energy of the large raindrop bubble sound tends to become smaller and more broadband in nature for decreasing drop size.
- The dominant bubbles produced by the drop splash are responsible for most of the underwater sound energy of individual large raindrops.

A statistical approach for relating underwater spectral levels to raindrop size distributions would be fruitful, and may reveal more about the physical processes of underwater sound generation by rainfall.

APPENDIX A

DERIVATION OF THE EQUATION FOR THE ENERGY SPECTRUM

The continuous Fourier Transform for aperiodic signals is given by:

$$X(f) = \int_{-\infty}^{\infty} x(t) e^{-j2\pi ft} dt \tag{35}$$

Assume the signal is discretized using $t = n\Delta t$, where n ranges from $-N/2$ to $N/2$ (in the limit as N goes to infinity). The discrete form of the above equation is then:

$$X(f_k) = \sum_{-N/2}^{N/2} x(n) e^{\frac{-jk2\pi n\Delta t}{N\Delta t}} \Delta t = \Delta t \sum_{-N/2}^{N/2} x(n) e^{\frac{-j2\pi kn}{N}} = \Delta t \cdot X(k) \tag{36}$$

where $X(f_k)$ becomes $\Delta t \cdot X(k)$, and $X(k)$ is the Discrete Fourier Transform of the signal x.

By Rayleigh's Theorem for an aperiodic signal, the energy is conserved per the following equation:

$$E = \int_{-\infty}^{\infty} |x(t)|^2 dt = \int_{-\infty}^{\infty} |X(f)|^2 df \tag{37}$$

which, after substituting the discrete forms of $x(t)$, $X(f)$, and $df = 1/N\Delta t$, becomes:

$$E = \sum_{-N/2}^{N/2} |x(n)|^2 \Delta t = \sum_{-N/2}^{N/2} |X(f_k)|^2 df = \sum_{-N/2}^{N/2} |X(k)\Delta t|^2 \left(\frac{1}{N\Delta t}\right) \tag{38}$$

or, after canceling like terms:

$$E = \sum_{-N/2}^{N/2} |x(n)|^2 \Delta t = \frac{\Delta t}{N} \sum_{-N/2}^{N/2} |X(k)|^2 \tag{39}$$

The units of $x(n)$ are Pa (the 1 m on-axis pressure), while the units of $X(k)$ are Pa per bin. Equation 39 can be rewritten so that the Fourier Spectrum is summed over all frequencies, where the frequency resolution is given by $df = 1/(N\Delta t)$:

$$E = \frac{\Delta t}{N \cdot df} \sum_{-N/2}^{N/2} |X(k)|^2 \cdot df \tag{40}$$

The individual terms on the right hand side of Equation 40 represent the energy spectrum of the finite duration pressure signal, in units of $Pa^2 \cdot s/Hz$. Since the frequency spectrum is symmetric, the negative frequencies can be mapped into the positive frequencies by multiplying the spectral levels by two, yielding:

$$E(f) = \frac{2 \cdot \Delta t}{N \cdot df} \cdot |X(k)|^2, \quad f \geq 0 \tag{41}$$

where $E(f)$ represents the energy density spectral level in $Pa^2 \cdot s/Hz$ for the frequency $f = k \cdot df$ as the index k varies from 0 to $N/2$.

To verify Equation 41, a damped sinusoid given by $p(t) = e^{-\alpha t} \cdot \cos(2\pi f_o t)$ was used to simulate an actual bubble signal. The value of α was taken to be $1/(5 \cdot 10^{-4})$ s^{-1}, and f_o was assumed to be 5000 Hz. The signal was sampled at an interval of 1 μsec, with a total record length of 2048 points. A plot of the signal is shown in Figure 71. The energy density spectrum of the signal was then calculated using Equation 41. The resulting spectrum is shown in Figure 72. The total signal energy was then calculated in both the time domain and the frequency domain to yield the following results:

$$\sum_{n=0}^{n=N-1} p(n)^2 dt = 1.2446 \cdot 10^{-4} \quad Pa^2 \cdot s$$
$$\sum_{f=0}^{f=f_{max}} E(f)\, df = 1.2495 \cdot 10^{-4} \quad Pa^2 \cdot s \qquad (42)$$

The resulting values are in good agreement.

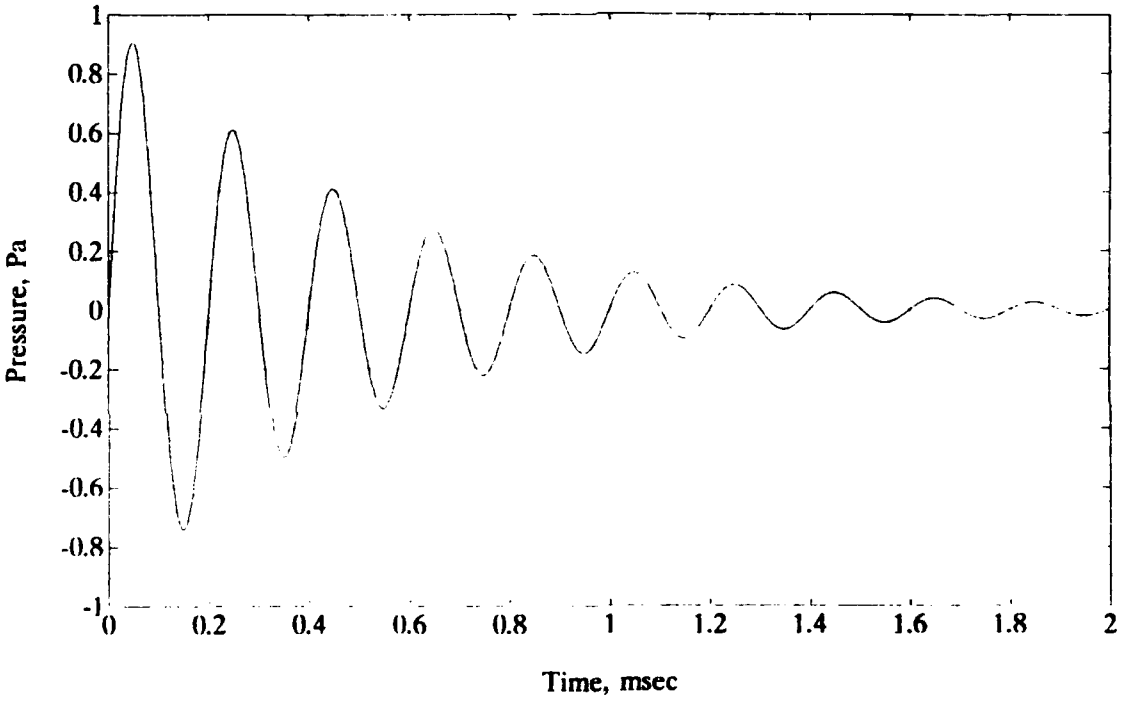

Figure 71. Simulated bubble signal for spectrum verification.

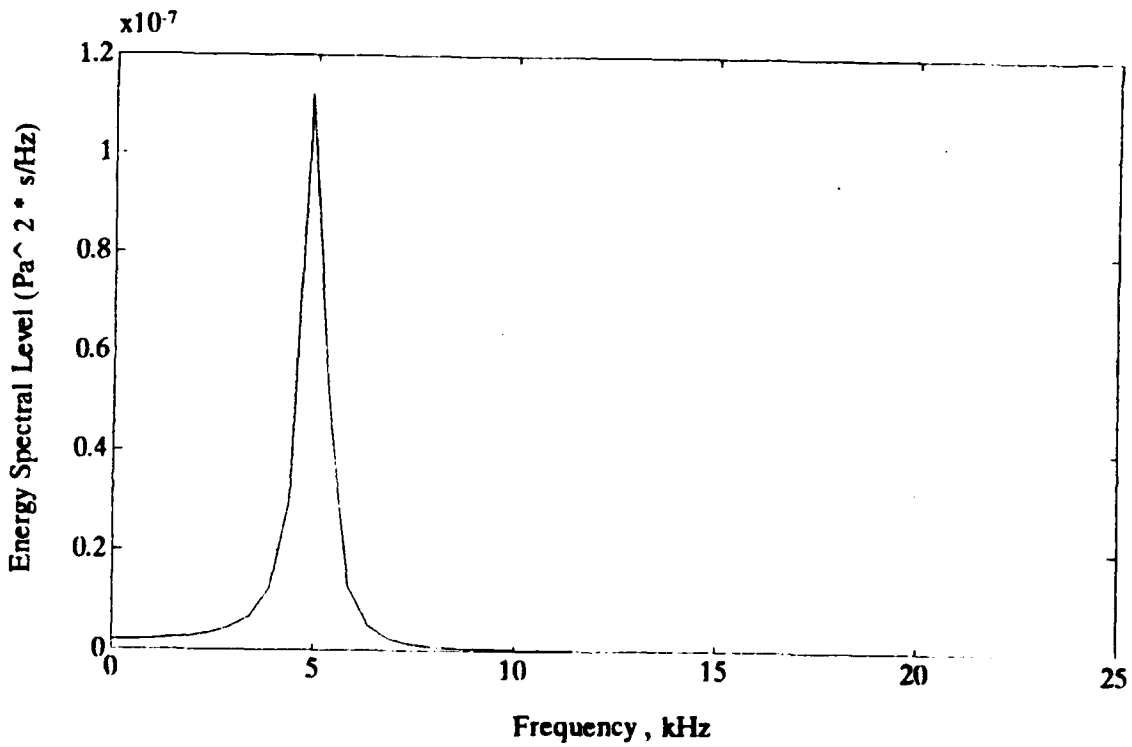

Figure 72. Energy density spectrum of simulated bubble signal.

APPENDIX B

DERIVATION OF THE BUBBLE ENERGY EQUATION

Let $p_{ax}(t, r)$ be the instantaneous on-axis acoustic pressure of a dipole source at a range r, and $p(t, r, \theta)$ be the pressure at the range r and angle θ. For a dipole source, $p(t, r, \theta) = p_{ax}(t, r) \cos \theta$, where θ is the angle with the dipole axis. The radiated acoustical energy E can be written as:

$$E = \int_t \int_A (INTENSITY)\, dA\, dt = \int_t \int_A (p \cdot u)\, dA\, dt \qquad (43)$$

where u is the particle velocity and A is the surface area. The integration in area is performed over the hemisphere from the dipole axis to the surface.

When $k \cdot R > 3$, the relationship $u = p / (\rho c)$ can be used with less than 10% error in magnitude, where ρc is the acoustic impedance and k is the wavenumber. Performing a surface integration with a ring element given by $(2\pi \cdot r \cdot \sin \theta)\, r d\theta$ and substituting the expression for p in terms of p_{ax}, we have:

$$E = \left(\frac{2\pi r^2}{\rho c}\right) \int_t \int_0^{\frac{\pi}{2}} p_{ar}^2 \cos^2\theta \sin\theta \, d\theta \, dt - \left(\frac{2\pi r^2}{3\rho c}\right) \int_t p_{ar}^2 \, dt \tag{44}$$

which can be expressed in digitized form as:

$$E = \left(\frac{2\pi r^2}{3\rho c}\right) \sum_{t=0}^{t=T} p_{ar}^2 \, \Delta t \tag{45}$$

where T is the time duration of the signal (eg., the record length).

APPENDIX C

DERIVATION OF THE RAINFALL SPECTRUM EQUATION

Given $DRD(d)$ (the drop rate density for a given raindrop size in units of drops/m^{2}s), and $E(f,d)$ (the 1 meter on-axis energy density spectral values for a given drop size in units of Pa^2·s/Hz), the spectral values at a depth z_o due to raindrops of a given size can be determined by summing the individual contributions from the bubble and impact dipole sources distributed over the surface.

The spectral values at the depth z_o must be obtained by integrating the contributions to the underwater sound from each drop size over the surface area, while accounting for the dipole nature of the bubble and impact sound. The spectral values for each drop size can then be summed to yield the overall rainfall spectrum. The geometry of the problem is illustrated in Figure 73.

The pressure p at a range r and angle θ from a surface dipole is equal to the on-axis pressure p_{ax} times the ratio $\cos(\theta)\cdot r_1/r$, where r_1 is 1 meter. If the range r is such that the plane wave approximation is valid, then the intensity is approximately equal to $p^2/(\rho c)$, where ρc is the acoustic impedance. If the intensity is proportional to the square of the pressure, then the intensity at the depth z_o due to an arbitrary dipole will be equal to the on-axis intensity of the dipole at one meter times the square of the ratio

$\cos(\theta)\cdot r_1/r$. The effect of attenuation has been neglected here. Accounting for the dipole variation of intensity, the total rainfall spectrum at a depth z_o can be expressed as:

$$RS(f) = \sum_d [\int_A E(f,d)\cdot DRD(d)\cdot \frac{r_1^2\cos^2\theta}{r^2}\cdot dA] \qquad (46)$$

where the area integration is carried out over the ocean surface. Referring to Figure 73, the surface area element dA for a ring integration is given by $dA = 2\pi\cdot h\cdot dh$, where h varies from zero to $r\cdot\sin\psi(f)$. The angle $\psi(f)$ corresponds to the beamwidth at a frequency f for an upward looking receiver at the depth z_o. Equation 46 can be transformed to an integral in θ using the substitutions $z_o = r\cos\theta$, $h = r\sin\theta$, and $dh = z_o\sec^2\theta\ d\theta$, which leads to:

$$RS(f) = \sum_d [\ 2\pi\cdot r_1^2\int_0^{\psi(f)} E(f,d)\cdot DRD(d)\cdot\cos\theta\cdot\sin\theta\, d\theta] \qquad (47)$$

Finally, evaluation of the integral leads to:

$$RS(f) = \sum_d \pi\cdot E(f,d)\cdot DRD(d)\cdot\sin^2\psi(f)\cdot 1\mathrm{m}^2 \qquad (48)$$

where r_1^2 has been replaced by 1 m^2.

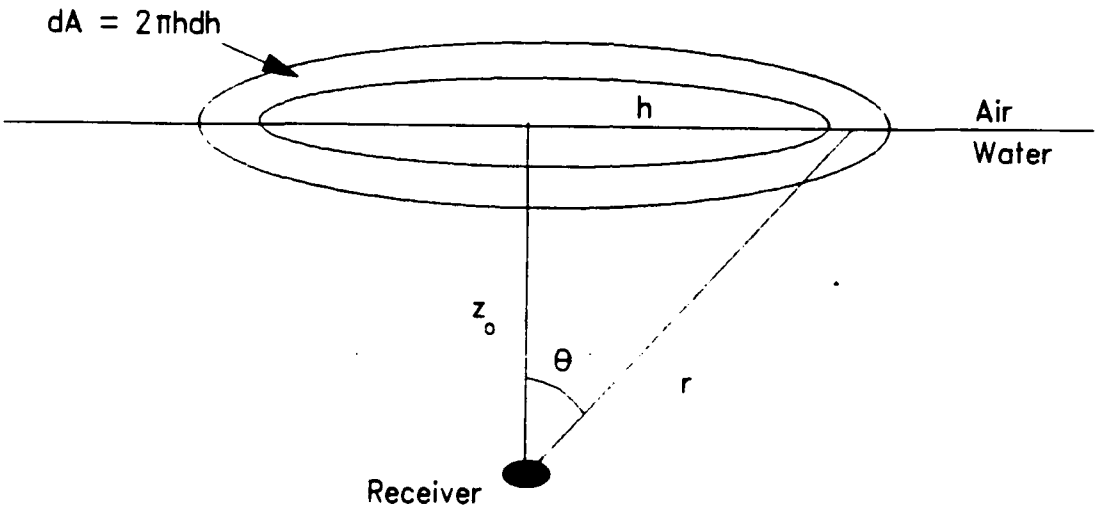

Figure 73. Geometry for the ring integration of the surface sound field.

LIST OF REFERENCES

Anton, H., and Rorres, C., *Elementary Linear Algebra with Applications*, pp. 301-323, John Wiley and Sons Inc., 1987.

Atlas, D., and Ulbrich, C. E. W., "The Physical Basis for Attenuation - Rainfall Relationships and the Measurement of Rainfall Parameters by Combined Attenuation and Radar Methods," *J. Rech. Atmos.*, **8**, pp. 275-298, 1974.

Clay, C. S. and Medwin, H., *Acoustical Oceanography: Principles and Applications*, pp. 194-203, John Wiley and Sons Inc., 1977.

Franz, G. J., "Splashes as Sources of Sound in Liquids," *J. Acoust. Soc. Am.*, **31**, pp. 1080-1096, 1959.

Hodson, M. C., "Raindrop Size Distribution," *J. Climate Appl. Meteor.*, **25**, pp. 1070-1074, 1986.

Jacobus, P. W., *Underwater Sound Radiation from Large Raindrops*, Master's Thesis, Naval Postgraduate School, Monterey, California, 1991.

Kurgan, A., *Underwater Sound Radiated by Impacts and Bubbles Created by Raindrops*, Master's Thesis, Naval Postgraduate School, Monterey, California, 1989.

Lemon, D. D., Farmer, D. M., and Watts, D. R., "Acoustic Measurements of Wind Speed and Precipitation Over a Continental Shelf," *J. Geophys. Res.*, **89**, pp. 3462-3472, 1984.

Longuet-Higgins, M. S., "An Analytic Model of Sound Production by Raindrops," *J. Fluid Mechanics*, **214**, pp. 395-410, 1990.

Marshall, J. S., and Palmer, W. McK., "The Distribution of Raindrops with Size," *J. Meteor.*, **5**, 165-166, 1948.

McGlothin, C., *Ambient Sound in the Ocean Induced by Heavy Precipitation and the Subsequent Predictability of Rainfall Rate*, Master's Thesis, Naval Postgraduate School, Monterey, California, 1990.

Medwin, H., and Beaky, M. M., "Bubble Sources of the Knudsen Sea Noise Spectra," *J. Acoust. Soc. Am.*, **86**, pp. 1124-1130, 1989

Medwin, H., and Daniel, A. C., "Acoustical Measurements of Bubble Production by Spilling Breakers," *J. Acoust. Soc. Am.*, **88**, pp. 408-412, 1990.

Medwin, H., Jacobus, P. W., Snyder, D. E., and Nystuen, J. A., "The Anatomy of Underwater Rain Noise," paper presented at the Acoust. Soc. Am. Conf., New Orleans, Louisiana, 1992.

Medwin, H., Kurgan, A., and Nystuen, J. A., "Impact and Bubble Sound from Raindrops at Normal and Oblique Incidence," *J. Acoust. Soc. Am.*, **88**, pp. 413-418, 1990.

National Center for Physical Acoustics Technical Report, *Sources of Ambient Noise in the Ocean: an Experimental Investigation*, by H. C. Pumphrey and L. A. Crum, pp. 16-27, 1989.

Nystuen, J. A., "Rainfall Measurements using Underwater Ambient Noise," *J. Acoust. Soc. Am.*, **79**, pp. 972-982, 1986.

Nystuen, J. A., "An Explanation of the Sound Generated by Light Rain in the Presence of Wind", to appear in *Natural Sources of Underwater Sound*, ed. B. R. Kerman, Kluwer Academic Press, 1992.

Nystuen, J. A., and Farmer, D. M., "Precipitation in the Canadian Atlantic Storms Program: Measurements of the Acoustic Signature," *Atmosphere-Ocean*, **27**, pp. 237-257, 1989.

Nystuen, J. A., and Farmer, D. M., "The Influence of Wind on the Underwater Sound Generated by Light Rain in the Presence of Wind," *J. Acoust. Soc. Am.*, **82**, pp. 270-274, 1987.

Oguz, H. N., and Prosperetti, A., "Bubble Entrainment by the Impact of Drops on Liquid Surfaces," *J. Fluid Mechanics*, **218**, pp. 143-162, 1990.

Pruppacher, H. H., and Klett, J. D., *Microphysics of Clouds and Precipitation*, D. Reidel Publishing Company, Dordrecht, Holland, 1978.

Pruppacher, H. R., and Pitter, R. L., "A Semi-Empirical Determination of the Shape of Cloud and Raindrops," *J. Atmos. Sci.*, **28**, pp. 86-94, 1971.

Pumphrey, H. C., Crum, L. A., Bjorno, L., "Underwater Sound Produced by Individual Drop Impacts and Rainfall," *J. Acoust. Soc. Am.*, **85**, pp. 1518-1526, 1989.

Pumphrey, H. C., "Underwater Rain Noise - the Initial Impact Component," paper presented at the United Kingdom Institute of Acoustics Meeting, 1991.

Snyder, D. E., *Characteristics of Sound Radiation from Large Raindrops*, Master's Thesis, Naval Postgraduate School, Monterey, California, 1990.

Tan, C., *A Characterization of Underwater Sound Produced by Heavy Precipitation*, Master's Thesis, Naval Postgraduate School, Monterey, California, 1990.

Ulbrich, C. E. W., "Natural Variations in the Analytical Form of the Raindrop Size Distribution," *J. Climate Appl. Meteor.*, **22**, pp. 1764-1775, 1986.

Undersea Surveillance Department, Naval Undersea Center, San Diego, TP 532, *Windows, Harmonic Analysis, and the Discrete Fourier Transform*, by F. J. Harris, pp. 14-16, 1976.

Waldvogel, A., "The N_0 Jump of Raindrop Spectra," *J. Atmos. Sci.*, **31**, pp. 1067-1078, 1974.

Walpole, R. E., and Myers, R. H., *Probability and Statistics for Engineers and Scientists*, 4th Ed., pp. 164-165, Macmillan Publishing Co., 1989.

Wiggins, R. A , "The General Linear Inverse Problem: Implication of Surface Waves and Free Oscillations for Earth Structure," *Reviews of Geophysics and Space Physics*, **10**, pp. 251-285, 1972.

Ziomek, L. J., *Underwater Acoustics: A Linear Systems Theory Approach*, pp. 79-80, Academic Press Inc., 1985.

INITIAL DISTRIBUTION LIST

	No. Copies
1. Defense Technical Information Center Cameron Station Alexandria, VA 22304-6145	2
2. Library, Code 52 Naval Postgraduate School Monterey, CA 93943-5000	2
3. Chairman (Code OC/Co) Department of Oceanography Naval Postgraduate School Monterey, CA 93943-5000	1
4. Dr. A. A. Atchley Code (PH/Ay) Naval Postgraduate School Monterey, CA 93943-5000	1
5. Dr. J. A. Nystuen Code (OC/Ny) Naval Postgraduate School Monterey, CA 93943-5000	2
6. Dr. H. Medwin Code (PH/Md) Naval Postgraduate School Monterey, CA 93943-5000	1

7. Commander 1
Naval Oceanography Command
Stennis Space Center
MS 39529-5004

8. Commanding Officer 1
Naval Research Laboratory Detachment
Stennis Space Center
MS 39529-5004

9. Office of Naval Research (Code 420) 1
800 N. Quincy Street
Arlington, VA 22217

10. Office of Naval Research (Code 1125 OA)
800 N. Quincy Street
Arlington, VA 22217

11. Mr. Harry Selsor 1
Code 311, Naval Research Laboratory Detachment
Stennis Space Center
MS 39529-5004

12. Dr. John R. Proni 1
NOAA/AOML/OAD
4301 Rickenbacker Causeway
Miami, FL 33149

13. Lt. Leo H. Ostwald Jr., USN 1
Naval Submarine School
Code 80 SC AC Class 92050, Box 700
Groton, CT 06349-5700